1990-12

A comparison of ice drift motion from modeled and buoy data

Lundeen, Gregory N.

Monterey, California: Naval Postgraduate School

http://hdl.handle.net/10945/27628

AD-A246 062

NAVAL POSTGRADUATE SCHOOL
Monterey, California

DTIC
S ELECTE
FEB 2 0 1992
D D

THESIS

A COMPARISON OF ICE DRIFT MOTION
FROM MODELED AND BUOY DATA

by

Gregory N. Lundeen

December 1990

Thesis Advisor   Robert II. Bourke
Co-Advisor   James Morison

92-03999

92 2 14 173

REPORT DOCUMENTATION PAGE

1a Report Security Classification Unclassified		1b Restrictive Markings			
2a Security Classification Authority		3 Distribution Availability of Report			
2b Declassification Downgrading Schedule		Approved for public release; distribution is unlimited.			
4 Performing Organization Report Number(s)		5 Monitoring Organization Report Number(s)			
6a Name of Performing Organization Naval Postgraduate School	6b Office Symbol (if applicable) 68	7a Name of Monitoring Organization Naval Postgraduate School			
6c Address (city, state, and ZIP code) Monterey, CA 93943-5000		7b Address (city, state, and ZIP code) Monterey, CA 93943-5000			
8a Name of Funding Sponsoring Organization	8b Office Symbol (if applicable) ,	9 Procurement Instrument Identification Number			
8c Address (city, state, and ZIP code)		10 Source of Funding Numbers			
		Program Element No	Project No	Task No	Work Unit Accession No

11 Title (Include security classification) A COMPARISON OF ICE DRIFT MOTION FROM MODELED AND BUOY DATA

12 Personal Author(s) Gregory N. Lundeen

13a Type of Report Master's Thesis	13b Time Covered From To	14 Date of Report (year, month, day) December 1990	15 Page Count 124

16 Supplementary Notation The views expressed in this thesis are those of the author and do not reflect the official policy or position of the Department of Defense or the U.S. Government.

17 Cosati Codes			18 Subject Terms (continue on reverse if necessary and identify by block number)
Field	Group	Subgroup	PIPS, sea ice, Arctic buoys, ice forecast, Arctic

19 Abstract (continue on reverse if necessary and identify by block number)

U. S. Naval operations in the Arctic require an effective way to predict the movement and behavior of sea ice. This is currently provided by the Navy's PIPS model which is based on Hibler's (1979) sea ice model which combines the thermodynamic ice heat budget with a dynamic ice model sensitive to the effects of ice thickness and ice strength. The PIPS model simultaneously solves a system of four equations of ice momentum balance, ice rheology, ice thickness, and ice strength. In order to test the performance of Hibler's formulation, another version of it, developed by Lemke et al., (1990), was adapted to the Arctic Ocean. The model was initialized and run using 1986 forcing data and its performance evaluated using Arctic buoy drift data. Results indicate that the model ice drift is principally driven by wind forcing, that its response to changes in weather is rapid and essentially correct, and that it performs better at high wind speeds than at low wind speeds. Limitations to its accuracy were chiefly the result of limits to the precision and resolution of the input data provided to run the model, especially near the ice margins. Overall, the model performs well in depicting the ice flow pattern in all conditions in the Arctic.

20 Distribution Availability of Abstract ☒ unclassified unlimited ☐ same as report ☐ DTIC users	21 Abstract Security Classification Unclassified	
22a Name of Responsible Individual Robert H. Bourke	22b Telephone (include Area code) (408) 646-3270	22c Office Symbol OC/bf

DD FORM 1473,84 MAR   83 APR edition may be used until exhausted   security classification of this page
All other editions are obsolete

A Comparison of Ice Drift Motion
From Modeled and Buoy Data

by

Gregory N. Lundeen
Lieutenant, United States Navy
B.S., University of Miami, 1982

Submitted in partial fulfillment of the
requirements for the degree of

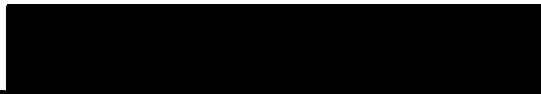MASTER OF SCIENCE IN METEOROLOGY AND PHYSICAL
OCEANOGRAPHY

from the

NAVAL POSTGRADUATE SCHOOL
December 1990

Author: _____
Gregory N. Lundeen

Approved by: _____
Robert H. Bourke, Thesis Advisor

_____
James Morison, Co-Advisor

_____
Curtis A. Collins, Chairman,
Department of Oceanography

ii

ABSTRACT

U. S. Naval operations in the Arctic require an effective way to predict the movement and behavior of sea ice. This is currently provided by the Navy's PIPS model which is based on Hibler's (1979) sea ice model which combines the thermodynamic ice heat budget with a dynamic ice model sensitive to the effects of ice thickness and ice strength. The PIPS model simultaneously solves a system of four equations of ice momentum balance, ice rheology, ice thickness, and ice strength. In order to test the performance of Hibler's formulation, another version of it, developed by Lemke et al., (1990), was adapted to the Arctic Ocean. The model was initialized and run using 1986 forcing data and its performance evaluated using Arctic buoy drift data. Results indicate that the model ice drift is principally driven by wind forcing, that its response to changes in weather is rapid and essentially correct, and that it performs better at high wind speeds than at low wind speeds. Limitations to its accuracy were chiefly the result of limits to the precision and resolution of the input data provided to run the model, especially near the ice margins. Overall, the model performs well in depicting the ice flow pattern in all conditions in the Arctic.

TABLE OF CONTENTS

LIST OF TABLES

LIST OF FIGURES

I. INTRODUCTION

Ever since man has sailed the cold waters of the North Atlantic and the Arctic he has had a desire and a need to determine the extent of the ice cover, ice motion, and ice thickness. Modern day operations in the Arctic, especially by the U. S. Navy, have made it important to be able forecast the behavior of the ice cover, namely its concentration, thickness, and motion. Real time knowledge of the sea ice extent and ice movement are provided on a limited basis today by satellite imagery and sparse buoy data. No technique is yet available to routinely provide real time ice thickness measurements. Thus polar scientists must rely on ice forecast models to provide knowledge of the temporal and spatial variability of these parameters. The development of effective models which can predict the ice concentration, thickness, and velocity is important for the long term study and safe use of the Arctic as well as the Antarctic. This has led to the development of a standard Navy model, the Polar Ice Prediction System (PIPS), which was designed to accomplish these goals.

In the Arctic considerable interaction between the atmosphere, oceans, and the ice layer takes place requiring the dynamic and thermodynamic relationships to be quite complex. Naturally expressions for these relationships have evolved over time, becoming more sophisticated as more measurements of various ice parameters has shed more light on their physical behavior and interaction. Early models used empirical relationships to determine ice motion or drift. The first model used by the Navy was developed by Skiles (1968). It related ice drift to the geostrophic wind and mean upper ocean currents. This model was subsequently replaced by the free drift ice model developed by Thorndike and Colony (1982). This model was based on a relationship between the geostrophic wind, ice, and ocean currents determined from a statistical analysis of five

1

years of drifting buoy data. These two models had serious deficiencies in that they did not take into account the effects of ice thickness, ice concentration, ice growth, and internal ice stress on ice drift.

At the same time these emperical ice drift models were in use, sophisticated sea ice models were developed that concentrated on the thermodynamic treatment of ice and its interaction with the atmosphere and the ocean (Maykut and Untersteiner, 1971; Semtner, 1976; Parkinson and Washington, 1979; Manabe et al., 1979). Early work relating ice dynamics and thermodynamics was conducted by Thorndike et al. (1975), Rothrock (1975), and Coon (1974). The concepts of an ice thickness distribution function and the coupling of ice thickness to ice rheology in the studies of ridging arose from these early studies. In 1979 these concepts of ice dynamics were combined with a working thermodynamic ice model to produce the Arctic Ice Dynamic Joint Experiment ice model (Pritchard, 1980). Hibler (1979) developed a model employing these concepts along with an Eulerian coordinate system and a viscous-plastic ice rheology which made long term simulation feasible. In time, a version of this dynamic-thermodyamic sea ice model was evaluated and modified to run at the Fleet Numerical Oceanography Center (FNOC) and was designated the Navy's standard model, known as the Polar Ice Prediction System (PIPS), for predicting ice motion, ice concentration, and ice thickness (Preller, 1985).

Hibler's model, the basis of PIPS, has been in wide use since 1979. Various studies have sought to define the model's accuracy by comparing different aspects of the model results to real world ice conditions. These include studies by Hibler and Walsh (1982) on seasonal variations, and a study by Tucker (1983) which compared the model ice drift results to buoy data in the Greenland Sea. Later a study was conducted by Tucker and Hibler (1986) which compared the PIPS forecast accuracy with a free ice drift model and buoy data that resulted in several improvements to the operational model (Preller and

Posey, 1989). Owens and Lemke (1990) developed a version of Hibler's ice model coupled to Lemke's one dimensional mixed layer ocean model for studies of the Antarctic.

The purpose of this study was to adapt the Owens-Lemke version of the Hibler sea ice model and run it on the NPS mainframe computer using historical input forcing data and to examine its ability to describe ice motion and ice concentration as compared to buoy trajectories and ice edge reports in the Arctic. The forcing data came from the FNOC Naval Operational Global Atmospheric Prediction System (NOGAPS), a model that provides analysis and prediction fields of atmospheric forcing variables from the year 1986. Buoy trajectories and satellite derived ice edge reports from 1986 were used for comparison of model results. The study concentrates on the ice drift velocities in the central Arctic basin and ice edge position in the eastern Arctic region of the Greenland and Barents Seas. The results are studied to see how the model handles the effects of seasonal variation, periods of maximum and minimum ice extent and thickness, periods of ice growth and decay, significant changes in the input forcing data from day to day such as large storms, and the effects of a snow layer. This study will also look at an instance of the Beaufort Gyre reversal.

As noted earlier, studies on the PIPS model's prediction ability were previously done by Tucker and Hibler (1986). During their study the model was updated on a weekly basis. Updating is not employed in this study. Instead the ice model's ability to portray conditions as accurately as possible, i.e., the real ice conditions over the course of a year, will be studied with historical analysis fields. This in effect removes one source of error (forecasting atmospheric forcing fields) from the study. It is expected that this will reveal some strengths and weaknesses in the ice model.

The following chapters contain an overview of the theories behind the dynamic thermodynamic sea ice model, followed by some specifics on the model version used in this study. This is followed by a chapter which discusses the input data and parameters

3

used in the ice model. The fourth chapter provides and discusses the results of the study. It is followed by a summary and conclusions chapter.

II. MODEL DESCRIPTION

A. GENERAL DESCRIPTION

The ice model used in this study is essentially the dynamic-thermodynamic sea ice model developed by Hibler (1979). As previously mentioned in Chapter I, this model offers improved dynamics over previous sea ice drift empirical models (Skiles, 1968; Thorndike and Colony, 1982) and added an ice thermodynamics component. Succinctly stated, the dynamic-thermodynamic ice model is an interaction between ice momentum balance and the continuity equations of ice thickness and compactness (Stossel et al., 1990). A detailed discussion of the model is provided by Hibler (1979) and in subsequent articles (Hibler, 1984; Preller, 1985; Lemke et al., 1990). An overview of the model, primarily derived from Hibler's 1979 article, is provided here. The main components of the model include equations to determine the momentum balance, the ice rheology, the ice thickness distribution, and the ice strength of an ice field in a specified domain.

Ice momentum balance describes the ice drift through wind and water stresses, Coriolis force, internal ice stress, inertial forces, and ocean tilt. This momentum balance can be discribed by the following equation

$$m \frac{Du}{Dt} = - mf k \times u + \tau_a + \tau_w - mg\nabla H + F \tag{1}$$

$$(1) \quad (2) \quad (3) \quad (4) \quad (5)$$

where the left hand side of the equation is the ice acceleration due to temporal and spatial changes in ice velocity (u). The right hand side of the equation represents the sum of the forces acting on the ice field; (1) is the Coriolis acceleration, (2) is the forcing due to wind stress, (3) is the forcing due to water stress, (4) is the forcing due to the tilt

5

of the sea surface, and (5) is the forcing from internal ice stress. In equation (1) m is the ice mass per unit area, f is the Coriolis parameter, g is the acceleration due to gravity, and H is the sea surface dynamic height. Figure 2.1 schematically shows how the forces act on an ice floe and their relative magnitude.

Observations have shown that the force balance is dominated by the air and water stresses, the Coriolis term, and, under compact ice conditions, the ice interaction or internal stress term (Hibler, 1984). Measurements of water and air stresses show them to be of the order of 0.1 Nm^{-2}. Wind stress is the larger of the two stresses in the central polar pack and plays the largest role in the movement of the ice. The Coriolis force is approximately 0.05 Nm^{-2}; the internal ice stress is variable but can reach similar magnitudes (Hibler, 1984).

The air and water stresses are defined by the following equations

$$\tau_a = \rho_a C_a \mid U_g \mid (U_g \cos \phi + k \times U_g \sin \phi) \tag{2}$$

$$\tau_w = \rho_w C_w \mid U_w - u \mid [(U_w - u) \cos \theta + k \times (U_w - u) \sin \theta] \tag{3}$$

where U_g is the geostrophic wind, U_w is the geostrophic ocean current, C_a and C_w are the air and water drag coefficients, ρ_a and ρ_w the air and water densities, and ϕ and θ are boundary layer turning angles for air and water, respectively. A turning angle is the angular difference between the ice motion and the direction of the force acting upon it (in this case geostrophic winds and oceanic currents), the difference arising from friction. The geostrophic winds act above the thin boundary layer that overlies the ice surface. Water stress acts in a manner opposite to the direction of ice movement (McPhee, 1979). Figure 2.2 illustrates the turning angle principle.

Ice is not completely solid; it can deform and flow like a fluid under stress. Ice rheology is the science of ice deformation, crushing, and flow through elastic, viscous,

and plastic means. Plastic behavior defines a permanant change in shape or deformation as a result of stress but without breaking. Viscosity determines a fluid's resistence to flow, while elasticity is an object's ability to return to its original shape after undergoing a stress. Ice breaks apart easily under tension resulting from diverging forces. During periods of convergence it may fracture or crush, rather easily when large amounts of thin ice are present. Thick ice, on the other hand, exhibits considerable resistence to compression and shearing. Hibler defined the deformation stresses involved through a viscous-plastic constitutive law which relates the ice stress to the strain rate and ice thickness (or equivilantly, ice strength). The force resulting from the internal ice stress is defined as follows:

$$F = \nabla \sigma \tag{4}$$

where σ, the two dimensional stress tensor, is calculated by the following equation

$$\sigma_{ij} = 2\eta(\varepsilon_{ij}, P)\varepsilon_{ij} + [(\zeta(\varepsilon_{ij}, P) - \eta(\varepsilon_{ij}, P))\varepsilon_{kk} - \frac{P}{2}]\delta_{ij} \tag{5}$$

where ε_{ij} is the strain rate tensor, P is a pressure term related to ice thickness, ε_{kk} is the ice divergence and ζ and η are the non-linear bulk and shear viscosities, respectively. In this model sea ice is considered to be a non-linear viscous compressible fluid that interacts in a rigid-plastic manner. This allows the ice to resist compression and shear deformation at high stresses while allowing dilation to occur when little or no stress is applied. In a manner proportional to the ice thickness or strength, ice is considered to flow plastically for high negative strain rates (compaction) and to deform in a linear viscous manner for sr all negative strain rates. This allows for ridging under compression and thinning under divergence. Figure 2.3 depicts how the ice behaves under stress.

7

The thickness of ice affects how the ice drifts and how it will deform under a stress. Thin ice with its relatively low mass will tend to be moved more by surface winds and other forces and will fracture and crush easily when compacted. Thick ice, with more mass per unit area, is more resistant to movement from forcing. Thick ice is also able to withstand higher amounts of convergence than thin ice. In the model an ice thickness distribution function accounts for the change of ice thickness and concentration due to growth, ablation, advection and deformation of sea ice. The original Hibler (1979) ice model considered the ice within a given grid cell to have only two thicknesses: thick ice of thickness h and having a concentration or compactness A ($0 \leq A \leq 1$) and thin ice of thickness essentially zero (includes open water) and a concentration of (1 - A). Later models, including the version used in this study, updated this two level thickness parameterization to a multilevel thickness parameterization (Hibler, 1984) with several levels of thickness h equally spaced from zero to twice the average ice thickness. The model used in this study uses a seven level parameterization.

Growth rates for thick ice (> 0.5 m) are considerably slower than for thin ice (< 0.5 m) (Owens and Lemke, 1990). This is a result of the slow transfer of heat through ice over a non-linear temperature gradient from the warmer ocean below to the cooler atmosphere above the ice layer. Thin ice has an almost linear transfer of heat across its layer allowing for faster growth in the presence of freezing conditions. Since the mass for thin ice is small, the average thickness for both thick and thin ice in a model cell is considered to be h/A. The seven level ice thickness, h, and its concentration, A, are derived from the continuity equations of thickness and compactness and include the effects of advection, convergence, divergence, thermodynamic growth and decay, and diffusion.

$$\partial \frac{h}{\partial t} = -\partial \frac{(uh)}{\partial x} - \partial \frac{(vh)}{\partial y} + S_h + diffusion \tag{6}$$

8

$$\partial \frac{A}{\partial t} = -\partial \frac{(uA)}{\partial x} - \partial \frac{(vA)}{\partial y} + S_A + \textit{diffusion} \qquad (7)$$

where the left hand side of equations (6) and (7) are the temporal changes of ice thickness and concentration, respectively. The first two terms of the right side of the equations describe the effects of advection, and convergence/divergence with u representing motion in the x direction and v represeting motion in the y direction. With advection ice can be moved into and out of a grid cell resulting in convergence and divergence, respectively. Divergence will decrease the ice thickness in a cell, opening leads and polynyas in which thin ice forms. Convergence will close leads and polynyas, crushing thinner and weaker ice thereby increasing the ice thickness in a grid cell. The third terms, S_h and S_A, are the thermodynamic terms of growth and decay. They are described in the following equations

$$S_h = f(\frac{h}{A})A + (1-A)\,f(0) \qquad (8)$$

$$S_A = \begin{cases} f\frac{(0)}{h_o}(1-A) & \text{if } f(0) > 0 \\ 0 & \text{if } f(0) < 0 \end{cases} + \begin{cases} 0 & \text{if } S_h > 0 \\ (\frac{A}{2h})S_h & \text{if } S_h < 0 \end{cases} \qquad (9)$$

where f(h) is the ice growth rate for each level of ice thickness h and f(0) is the growth rate of thin ice, h_o is a fixed demarcation between thick and thin ice of 0.5 m, and (1-A) is the fraction of open water. The S_h term is the sum of the ice grown in both open water and the additional growth of thick ice.

The growth rate of ice, f(h), is computed from a complex heat budget which determines the oceanic and atmospheric heat fluxes through the ice which arise from the conservation of energy at the upper and lower surfaces of the ice. Most ice models (including the one in this study) include provisions for calculating a snow layer for use in

9

the heat budget. The snow layer has the conflicting effects of providing an insulating cover to the ice surfaces which reduces ice growth rates and also having a high albedo which reflects incoming solar radiation reducing the rate of ice melt. The heat fluxes involved include incoming solar (short wave) radiation, net long wave radiation, sensible heat, latent heat, and conduction of heat from the ocean to the underside of the ice, from the upper ice surface to the snow, and from the snow layer to the atmosphere. Figure 2.4 provides a profile of the heat budget across the ice and snow layers. Following Semtner's (1976) formulation, heat is transferred through the ice sheet by assuming a linear temperature profile within the ice and a constant ice conductivity. When heat is lost from open water to the atmosphere, the ice growth rates resulting from the heat loss are taken be vertical in direction. When open water absorbs heat from the atmosphere, the heat is allowed to mix under the flows to reduce growth rates. Any remaining heat can be used to raise the mixed layer temperature, which causes lateral melting, or be used to raise the temperature of ice. In the presence of an ice cover the mixed layer is held at the freezing temperature until all the ice in a grid cell is melted first. (Preller and Posey,1989).

The strength of a substance is a measure of its ability to resist deformation as a result of stress. In this model ice strength (P) in equation (5) is treated as a function of the ice thickness distribution and concentration and is given by the equation

$$P = P^* h \exp \left[- C(1 - A) \right] \qquad (10)$$

where P* is a constant that is a measure of the maximum ice strength, the point where compressive stresses increase to a level sufficient to cause ice to deform as a plastic vice a linear viscous fluid (Figure 2.3.a). The constant C is the rate at which compactness (A) affects the ice strength. As explained below, this relationship makes the ice strength strongly dependent on the amount of thin ice present, but also allows the ice to

strengthen as it becomes thicker. When small amounts of thin ice are present in a cell, the larger quantities of thick ice remaining are subject to deformation (ridge building) giving the ice high strength due to its increased thickness. Conversely, for a cell containing a large amount of thin ice, mostly thin ice is deformed which yields a lower ice strength.

The overall model is an interaction of the four major sections of the ice model (momentum, rheology, thickness distribution, strength). They are coupled and together form a complete system of equations where ice velocities depend upon the ice thickness and concentration through the ice strength term (and internal interaction) while the ice thickness and concentration depend upon ice velocity through advection and convergence. Figure 2.5 shows a general flow chart of the dynamic-thermodynamic ice model. Subsequent versions of this model essentially follow the same equations as the original. The model version used in this study is described in the next section.

B. SPECIFICS ON MODEL USED FOR STUDY

The specific version of the dynamic-thermodynamic sea ice model used in this study (termed the NPS model) was one used by Lemke, Owens and Hibler in their studies of the Weddell Sea and Southern Ocean (Lemke et al., 1990; Owens and Lemke, 1990; Stossel et al., 1990). It is similar to the original Hibler model. The model code was kindly provided by Breck Owens of Woods Hole Oceanographic Institution along with a set of Weddell Sea data to verify the model output after adapting it to run on the NPS mainframe computer.

The NPS model uses a seven level ice thickness distribution vice the earlier two level level distribution. The PIPS model at FNOC also currently uses the seven level ice thickness distribution, a feature developed when it was found that the original two level approach produced an average ice thickness that was too thin compared to observations. The seven level approach resulted in an increase of ice thickness of approximately 0.5

m over the PIPS domain (Preller and Posey, 1989). In the thermodynamic part of the model, the ice growth rate is formulated as a highly nonlinear function of ice thickness while each grid cell is assumed to be covered by a distribution of ice thicknesses which are averaged to give the thickness h for that cell (Owens and Lemke, 1990). Ice growth rates were calculated from the seven-level thickness distribution function bounded between zero (thin or no ice) and twice the average thickness following the procedure of Hibler (1984).

The model code includes a one-dimensional mixed-layer pycnocline ocean model developed by Lemke (1987) that is coupled to the ice model growth subroutine in order to determine the vertical oceanic heat flux. Hibler's earlier (1979) model treated the ocean as a two layer fluid and specified the vertical oceanic heat flux as either a constant or a monthly varying value. The main feature of the Lemke subroutine is the prognostic calculation of the mixed layer temperature, salinity and depth and profiles of the thermocline and halocline as a function of ice production and ice velocity (Stossel et al., 1990; Owens and Lemke, 1990; Lemke et al., 1990). Figure 2.6 depicts the prognostic mixed layer model. These calculations were based on conservation of heat and salt, potential energy considerations, and parameterization of entrainment heat fluxes (Stossel et al., 1990). The PIPS model does not use this prognostic mixed layer ocean subroutine but instead holds the mixed layer constant at 30 m depth and provides ocean currents and oceanic heat fluxes via the Hibler-Bryan (1984) coupled ice ocean model. This latter model couples a three dimensional ocean model to a sea ice model and is discussed more fully in a later section. In order to emulate PIPS as much as possible, the NPS model runs for this study held the mixed layer depth constant at 30 m and variable oceanic heat fluxes were inputed as monthly gridded data. Comparison of model runs using the Weddell Sea data demonstrated that the prognostic and constant mixed layer approaches showed similar results during both periods of maximum ice

concentration (winter) and during summer when the ice extent was at a minimum (Lemke et al., 1990).

The model codes are modular in design allowing for increased flexibilty in adapting the model to different experimental conditions. Model parameters and forcing input data were read in by separate subroutines. Most of the calculations were also handled by separate subroutines and brought together by a main computational loop that directed the flow of the model at each time step. The model equations were run in the following order. The model parameters and initialization fields (either through restart data or basic initial data fields) were read in first. Then, at the beginning of the main loop, the forcing data were read in for that time step. Next, the ice pressure or strength was calculated, which was followed by the ice velocity integration to calculate the new ice velocities and viscosities through an over-relaxation scheme. The relaxation scheme starts out with a first guess for a value at a grid point (usually the previous time step's value). It then runs through an iteration procedure until a specified condition is met and that value is accepted. The goal is to force the routine to converge to a solution as close as possible to the true value. The next part of the program deals with the changes to ice thickness and concentration due to horizontal advection and diffusion of the ice field. This was follo ed by the thermodynamic growth calculations for ice thickness and concentration. It is at this point that the heat budget is calculated and used in the growth calculations. After the output of data and statistics the old values of the previous time step which had been retained for the present time step were replaced by the new values and a new time step was begun. The horizontal grid scheme was a staggered spatial grid, better known as an Arakawa B grid, with u and v ice velocities on the points of the grid cell and thickness and concentration offset to the center of the grid cell (Mesinger and Arakawa, 1974; Hibler, 1979). The time stepping was accomplished by a leapfrog-

13

trapeziodal scheme (Owens, 1990). Figure 2.7 depicts a ˜ odel grid cell with the variables arranged to a "b" grid scheme (Hibler, 1979).

The flexible model codes allowed for adaptation of the model to Arctic data and to the PIPS model domain with little change to the model code. Once the model was adapted to the NPS mainframe computer with the Weddell Sea data and satisfactory results were obtained (from comparison to runs of the same data provided by Owens), it was adapted for Arctic use. Parameters used in the model were reviewed to ensure they were appropriate for the Arctic. The PIPS grid was incorporated and the time step was reduced to 12 hours to match the Arctic input data sets. Most changes to the model occurred in the data input section. The model was run for three years to initialize the output using 1986 forcing data (discussed later) similar to PIPS (Preller and Posey, 1989) to acheive a steady state.

C. MODEL DOMAIN

The domain of this model is the same as that used by PIPS at FNOC. The grid as described by Preller (1985) is a subsection of the FNOC northern hemisphere polar stereographic grid illustrated in Figure 2.8. The domain of the grid covers the central Arctic basin, and the Barents, Greenland, and Norwegian Seas, essentially covering the Arctic basin from the Bering Strait to the north of Scotland. Figure 2.9 shows the PIPS grid superimposed on the Arctic Ocean with the land and ocean boundaries masked out (Preller, 1985). An averaged mapping factor is used to approximate equal spacing for the FNOC northern hemisphere polar stereographic grid in the region of the model domain (Preller, 1985). The ice model grid has dimensions of 47 by 25 grid points with 127 km spacing at all grid points. Figure 2.9 shows the grid laid over the Arctic region (Preller and Posey, 1989). The velocity grid is 46 by 24 with the same horizontal spacing.

The PIPS boundary masks provided by NOARL for ice velocities, thickness, and outflow are also used in this model. The purpose of the masks is to ˜ fine the bounda-

ries of the model. The velocity masks were on a 46 by 24 grid with constant values at the outer boundary and all land equal to zero and ice and open water equal to one. Thickness masks were in a 47 by 25 grid with zero's for the outer boundary and land and one elsewhere. The outflow masks were similar to the thickness masks except that the outflow cells were also set to zero. The combination of ice thickness of one and outflow of zero represented an outflow condition. Outflow for this model was permitted only at the southern boundary of the Greenland and Norwegian seas (Preller, 1985).

D. MAINFRAME USE

The ice model was run on the Naval Postgraduate School's IBM 3033 mainframe computer. Though the model has been run on a Sun Computer workstation (personal communication, Breck Owens at Woods Hole) the NPS mainframe was selected for its easy accessibility and ability to store and process large data sets.

The model was run on a batch processor due to its large size and the large amount of data involved, which required the adding of job control lines to the begining and end of the FORTRAN code. The increase in model size occurred because the Arctic data sets were about ten times the size of the Weddell Sea data sets and the model was run at 12 hour time steps vice once a day. This resulted in long computer processing times, so the model was run in segments during initialization and subsequent runs utilizing re-start records for continuity. At its best the model ran at 300 time steps per hour of cpu clock time.
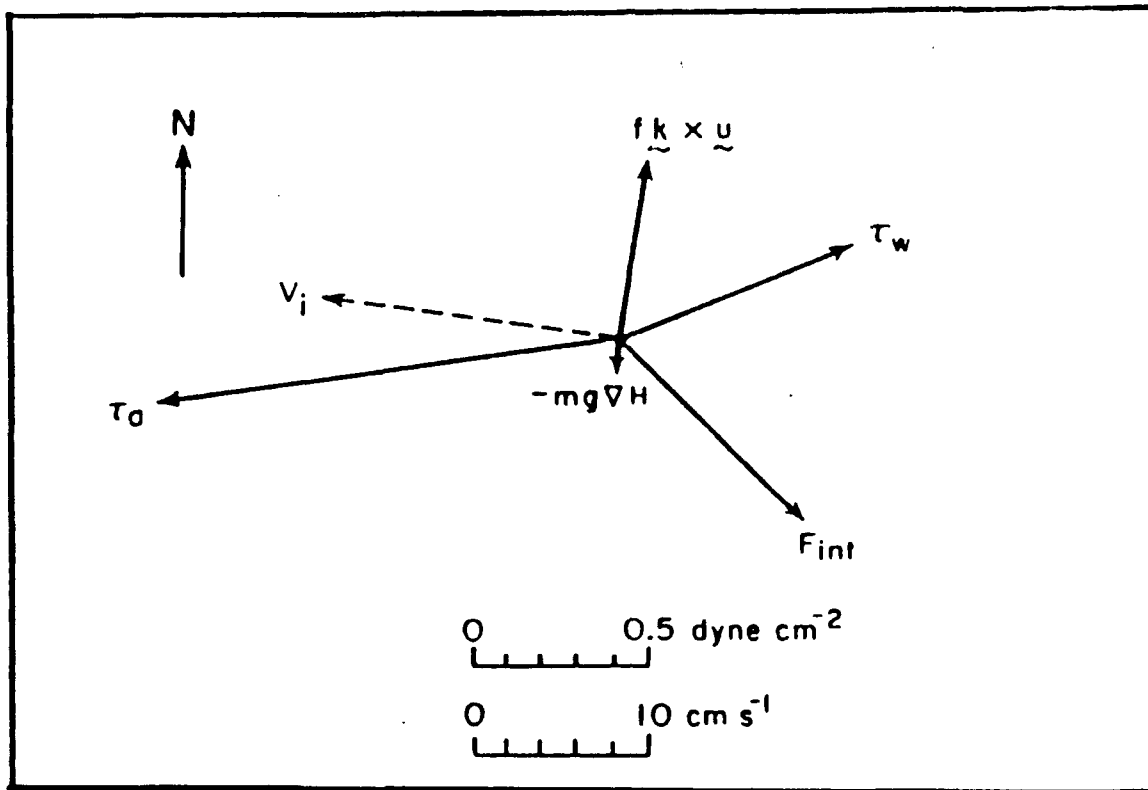
Figure 2.1 An illustration of the force balance on sea ice movement. The ice velocity (vector v_i) is acted upon by a strong wind stress (vector τ_a), a water stress acting in the opposite direction (vector τ_w), Coriolis force ($fk \times u$) acting to the right of the ice velocity, a small surface tilting term ($-mg\nabla H$), and a force resulting from internal ice stress (F_{int}), a term highly variable in magnitude and direction (Hibler, 1979).
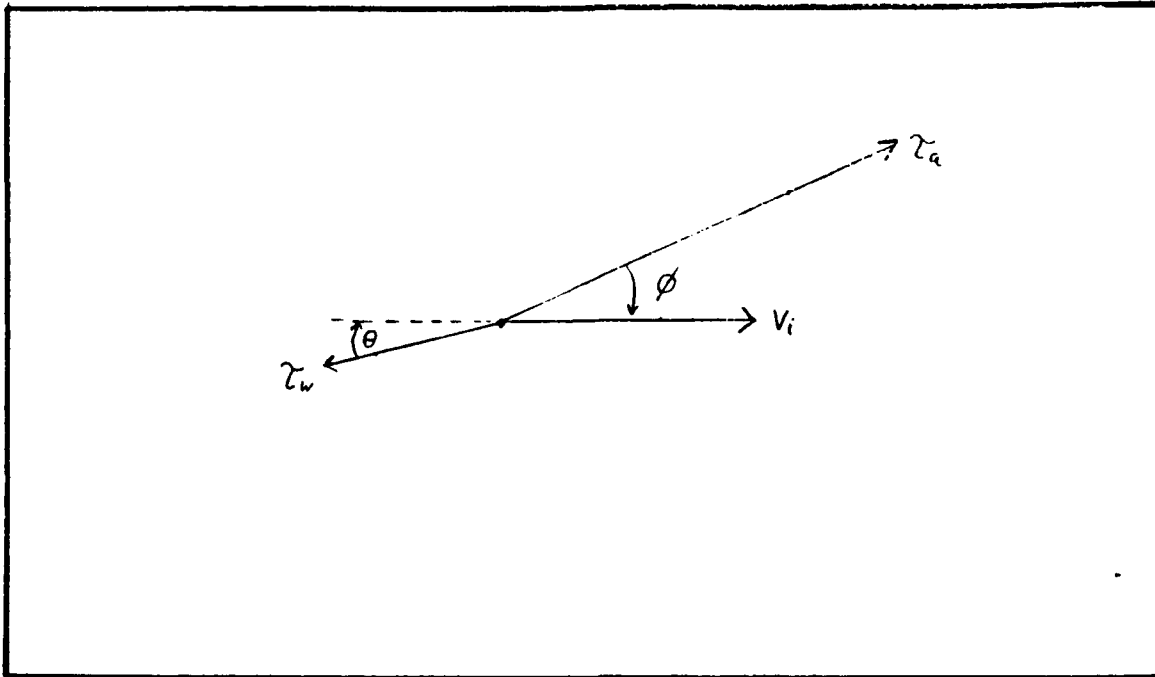
Figure 2.2 An illustration of turning angles. The vectors τ_a and τ_w represent air and water stresses, respectively. The vector v_i is the ice velocity. The angles θ and ϕ represent the boundary turning angles for water and air, respectively (McPhee, 1979).
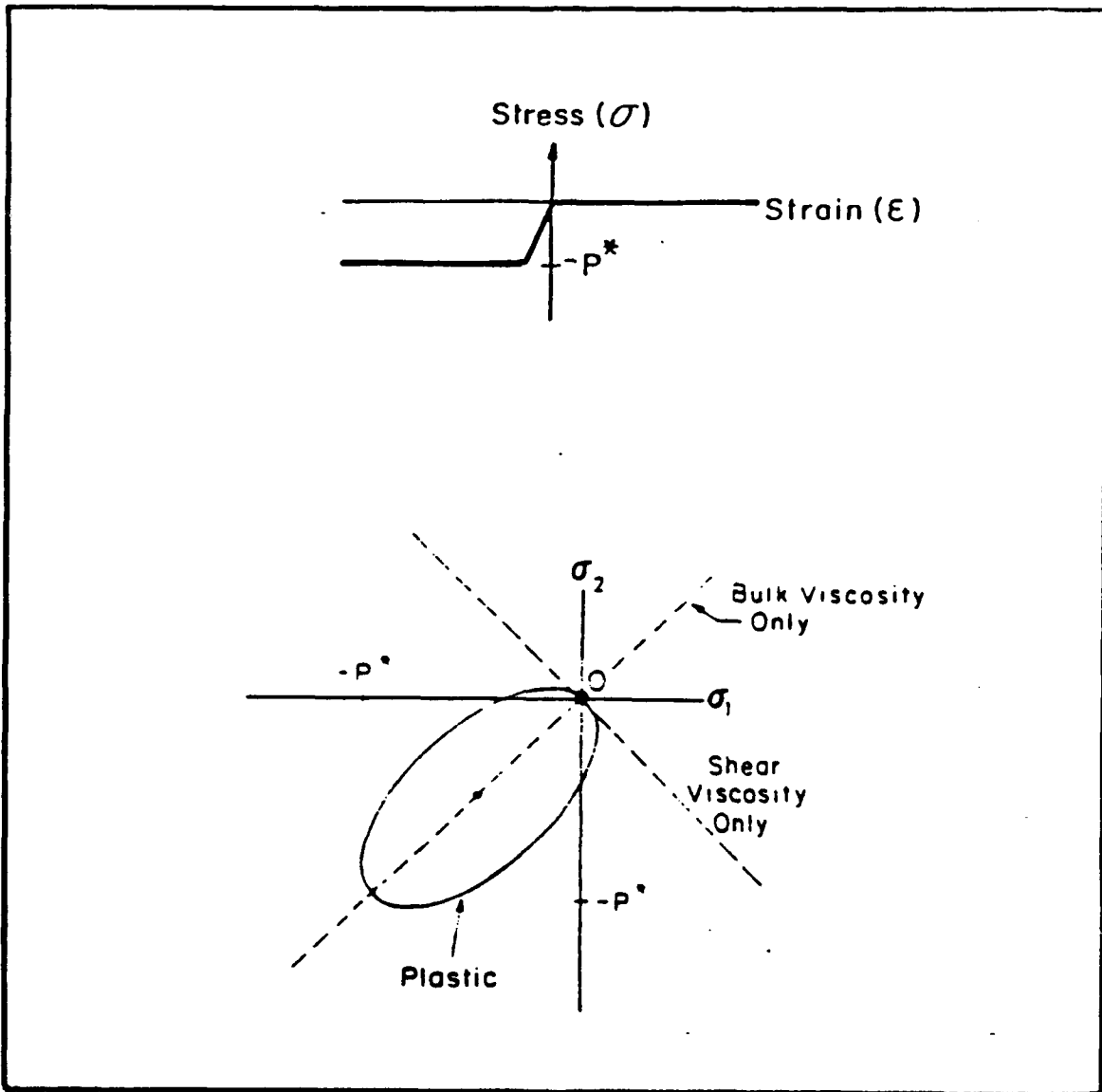
Figure 2.3 A visual illustration of the viscous-plastic constitutive law. The top figure is a one dimensional illustration of the law where as a function of ice strength, P^*, the ice behaves as a plastic under a negative strain rate and negative stress; as strain rate and stress near zero the ice behaves as a highly viscous fluid. There is no stress for positive strain rates (spreading). The lower figure illustrates the allowable stress state for a linear viscous rheology with either bulk or shear viscosity, and for a rigid plastic rheology with an elliptical yield curve. The stress states are plotted as a function of the principle components of the stress tensor σ (Hibler 1979).
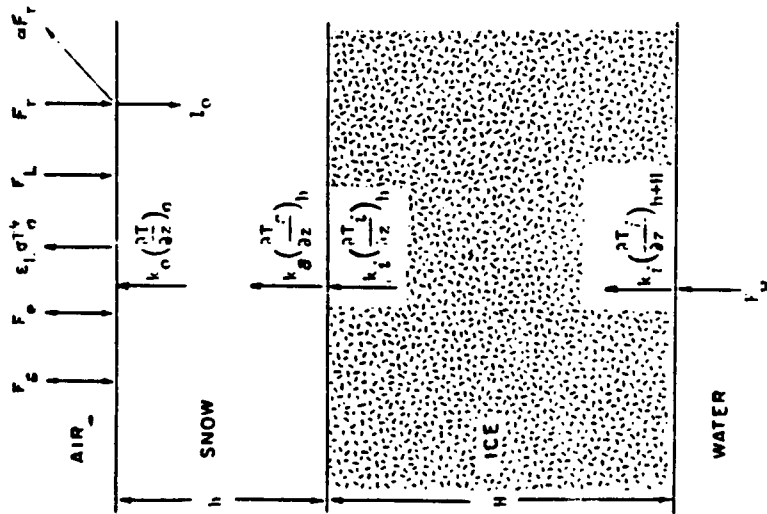
Balance of fluxes

$$(1-\alpha)F_r - I_o + F_L - \epsilon_L \sigma T_o^4 + F_s + F_e + k_o\left(\frac{\partial T}{\partial z}\right)_o + \left|\rho L \frac{d}{dt}(h+H)\right|_o = 0$$

$$(\rho c)_o \frac{\partial T_o}{\partial t} = k_o \frac{\partial^2 T_o}{\partial z^2} \quad \text{Heat conduction}$$

$$k_o\left(\frac{\partial T_o}{\partial z}\right)_h = k_i\left(\frac{\partial T_i}{\partial z}\right)_h \quad \text{Balance of fluxes}$$

$$(\rho c)_i \frac{\partial T_i}{\partial t} = k_i \frac{\partial^2 T_i}{\partial z^2} + \kappa_i I_o \exp(-\kappa_i z)$$

Heat conduction with internal heat source

$$k_i\left(\frac{\partial T_i}{\partial z}\right)_{h+H} - F_w = \left|\rho L \frac{d}{dt}(h+H)\right|_{h+H} \quad \text{Balance of fluxes}$$

$$\text{where} \quad (\rho c)_i = \rho c_o + \frac{\gamma S(z)}{(T_i - 273)^2}, \quad k_i = k_o + \frac{\beta S(z)}{T_i - 273}$$

Figure 2.4.a A schematic diagram of the thermodynamic heat balance in the sea ice model (Maykut and Untersteiner, 1971). It shows a balance of fluxes at 3 interface layers of air-snow, snow-ice, and ice-water with the conduction of heat in between each layer.
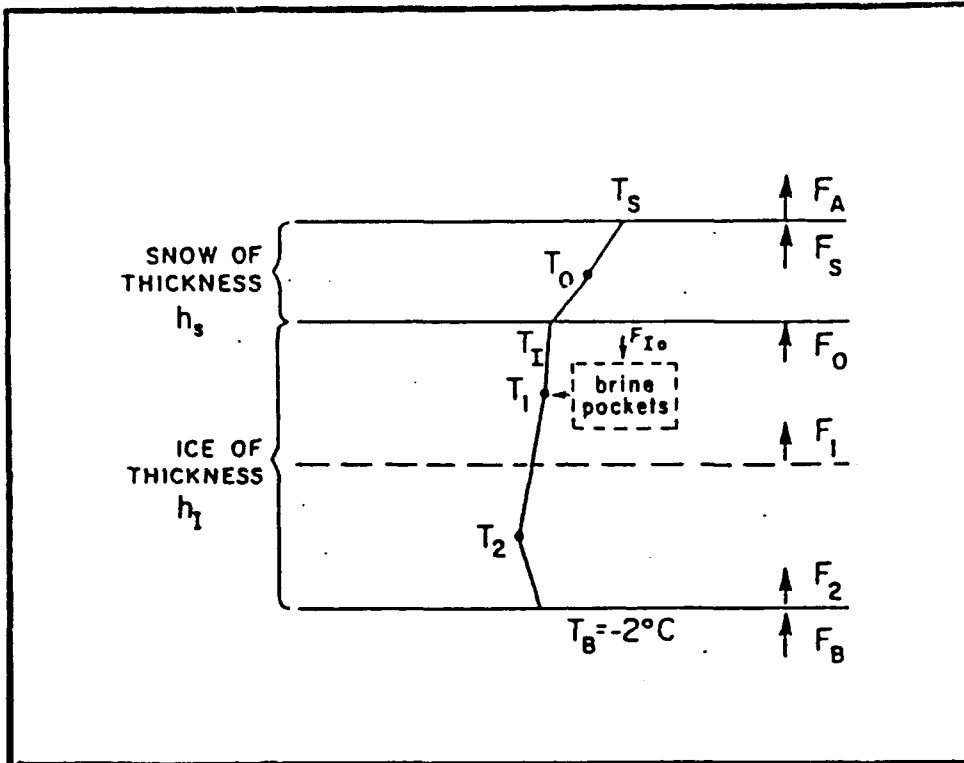
Figure 2.4.b A schematic diagram of a 3 layer model. Temperatures in the layers and thicknesses of the snow and ice are predicted on the basis of fluxes across internal and external boundaries (Semtner, 1976).
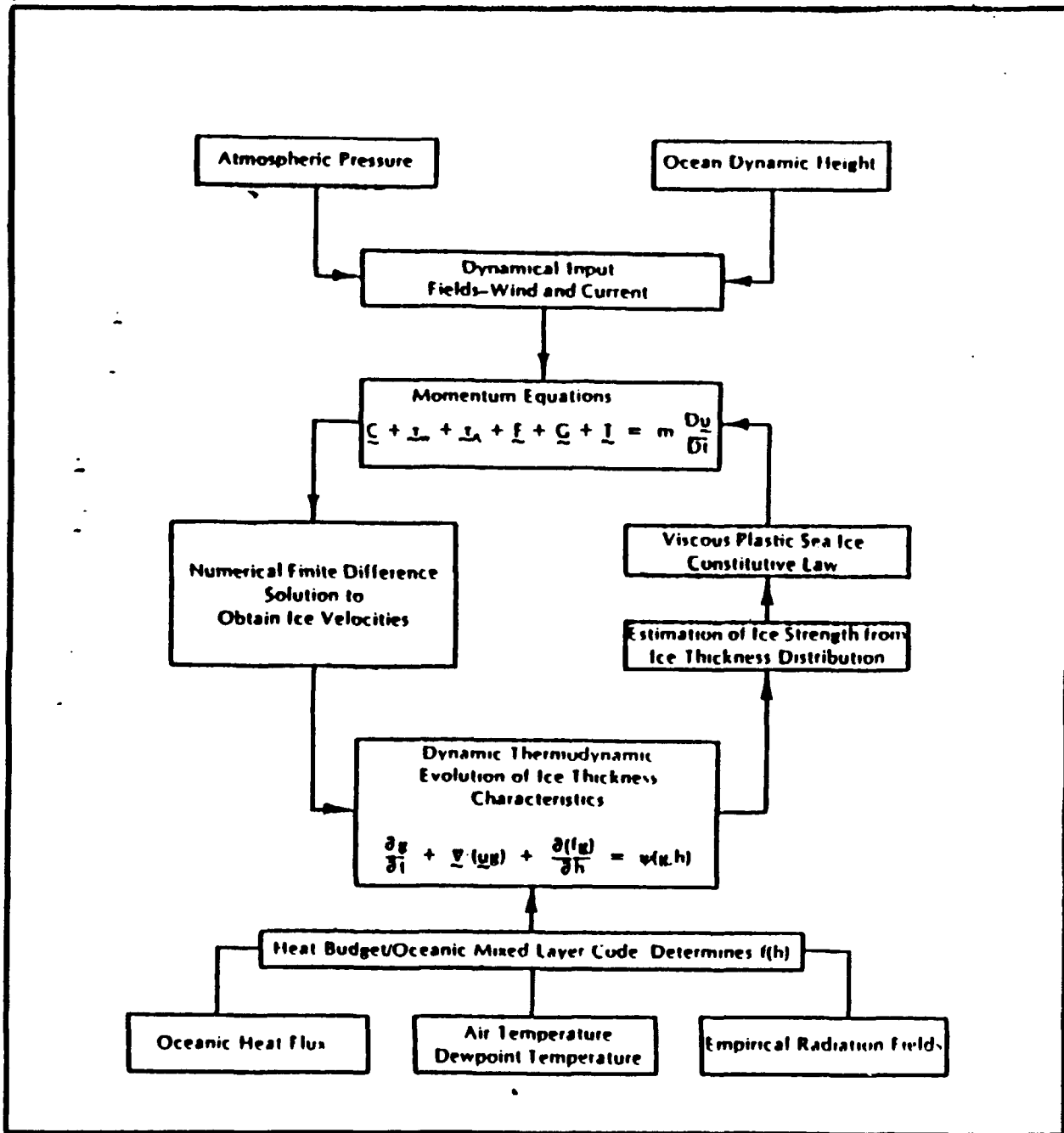
Figure 2.5 A flow chart for the dynamic-thermodynamic ice model. At the top winds and ocean currents are fed into the momentum equation to determine ice velocities. Thermodynamic fluxes are inputed into a heat budget that influences ice thickness along with ice advection. This is sent to an estimation of ice strength which is used to determine the internal ice stress which in turn is used in the momentum balance. In this figure C represents Coriolis force, τ_a the wind stress, τ_w the water stress, F the internal ice stress, G ocean currents, and T the surface tilting term, h the ice thickness, and f(h) the growth rate (Hibler, 1979).
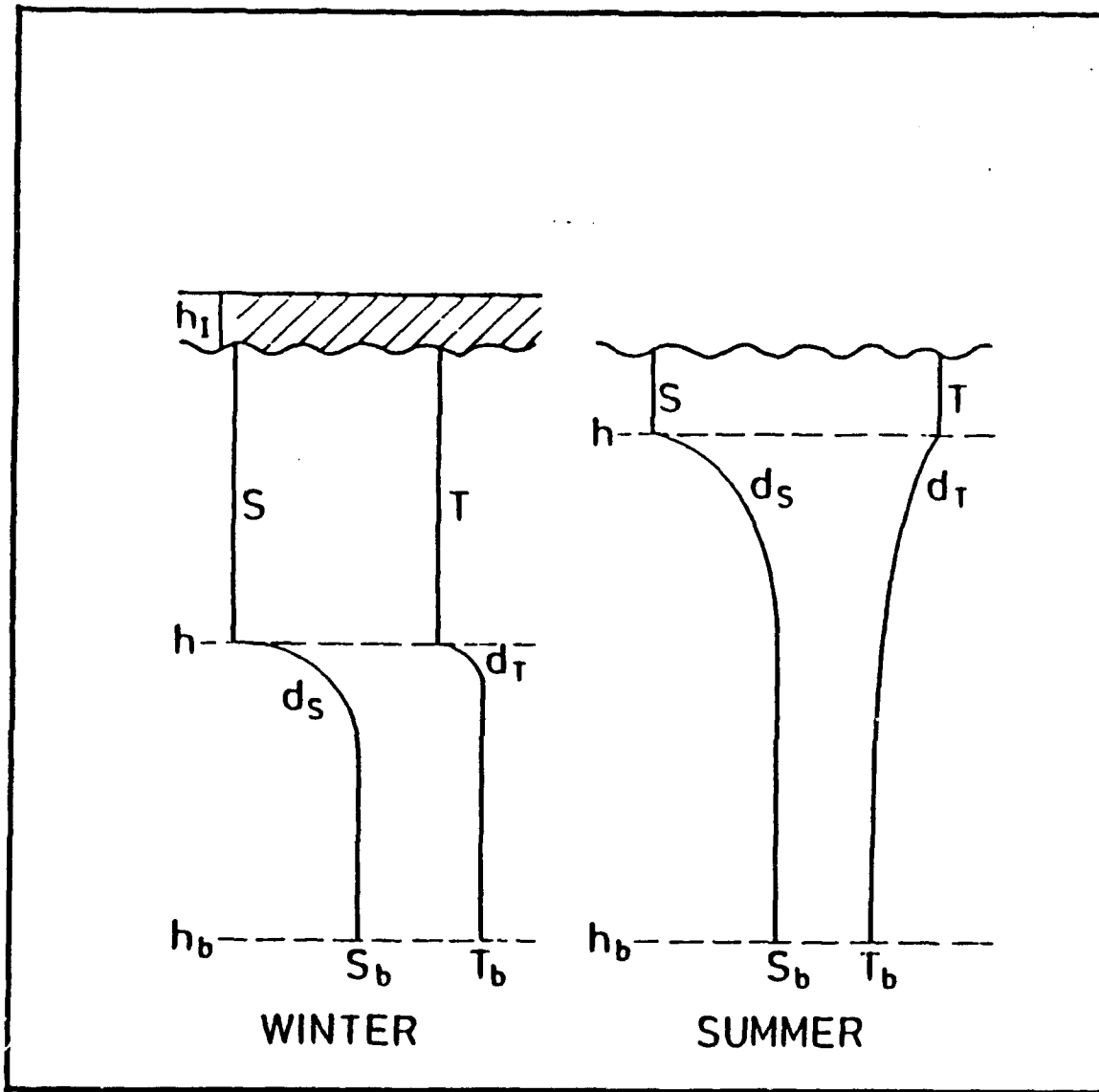
Figure 2.6 A profile of Lemke's (1987) one-dimensional ocean mixed layer model where h_I is the ice thickness, h the mixed layer depth, h_b is the bottom layer depth, S and S_b are the respective layer salinities, T and T_b are the respective temperatures, and d_s and d_T are the changes in salinity and temperature, respectively (Lemke et al., 1990).
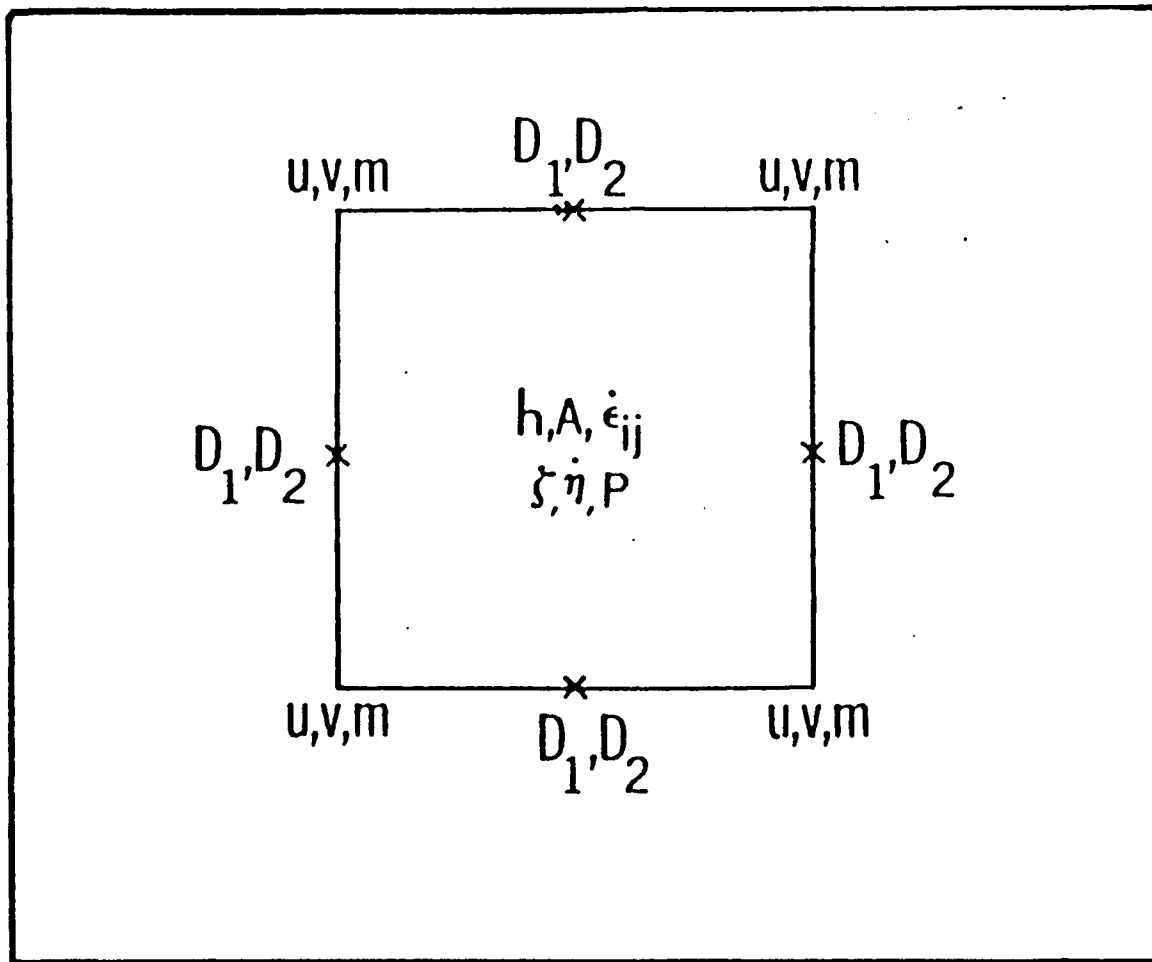
Figure 2.7 The spatial arrangement of variables used in the ice model. The variables u and v are the components of ice velocity, m is the ice mass, h is ice thickness, A is ice concentration, P is ice strength, $\dot{\varepsilon}$ is the ice strain rate, ζ and η are the bulk and shear viscosities, and D is the spatial difference (Hibler, 1979).
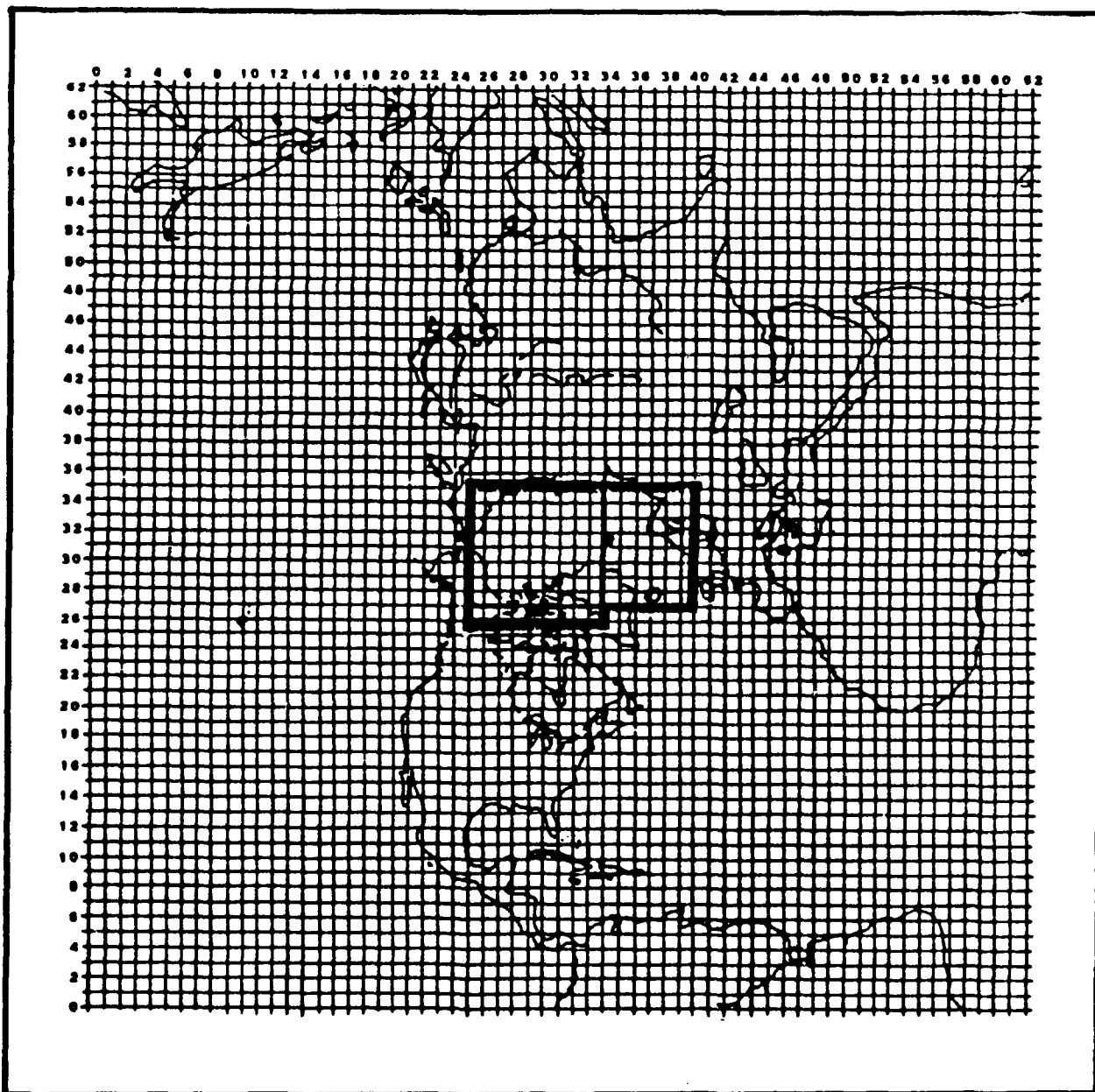
Figure 2.8 An illustration of the standard FNOC 63 x 63 northern hemispheric stereographic grid. The solid line boundaries show the regions used for the Arctic and PIPS domain (Preller, 1985).
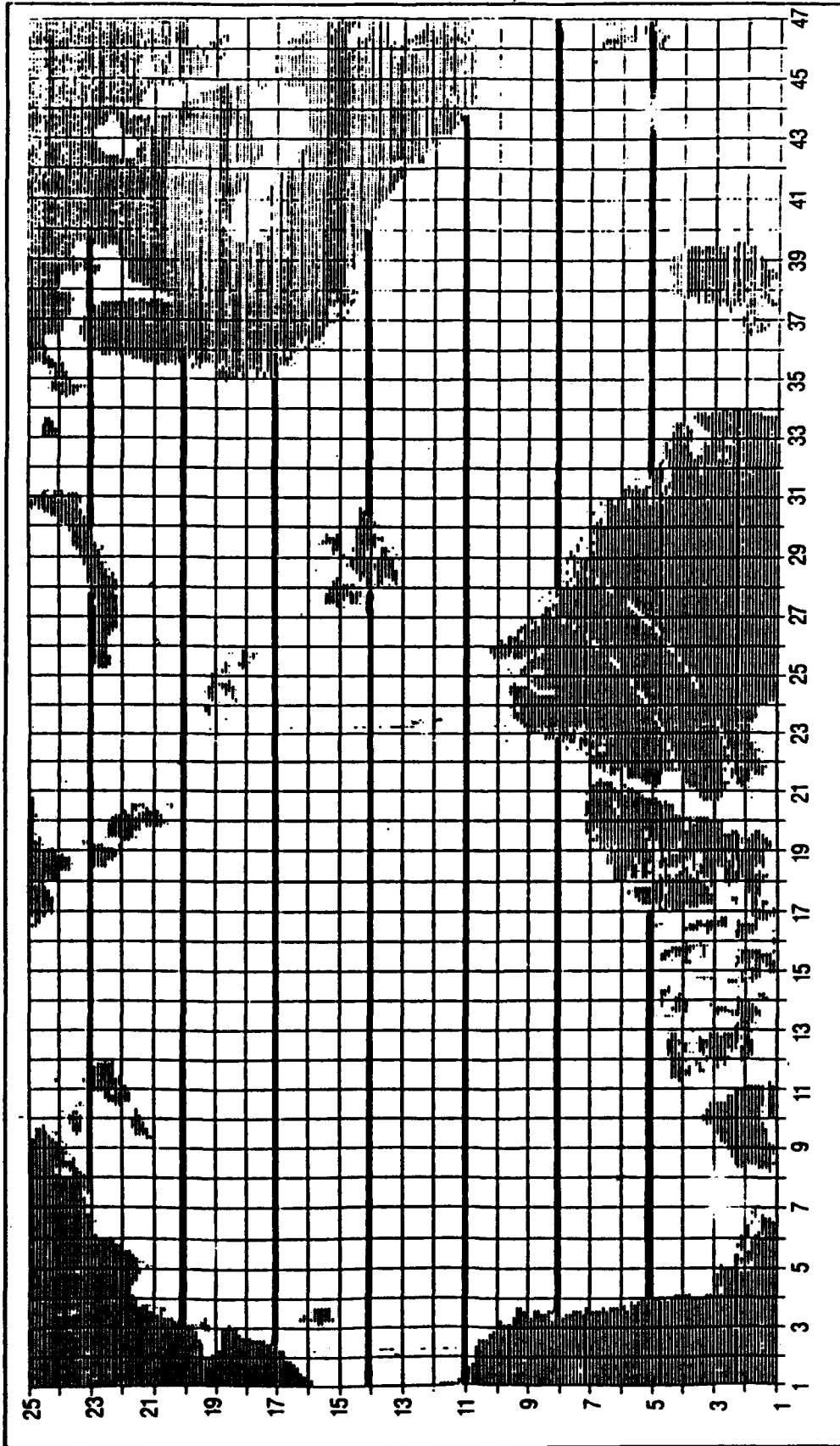
Figure 2.9 The PIPS model domain which is a 47 by 25 grid with a spatial resolution of 127 km. The land areas and the outer edge are masked as boundaries in the model (Preller, 1985).

25

III. FORCING DATA

A. DESCRIPTION OF THE DATA

Four categories of forcing data are required to run the ice model. They are wind stress, geostrophic ocean currents, atmospheric thermodynamic variables, and oceanic heat fluxes. The forcing data used in this study were kindly provided by Ruth Preller and Pam Posey (personal correspondance, 1990) of the Naval Ocean and Atmospheric Research Labratory (NOARL). The data covered the year 1986 and were in a gridded format when received.

The source of all the atmospheric data used in the model originated from 1986 analysis fields of the Naval Operational Global Atmospheric Prediction System (NOGAPS) model in use at FNOC. NOGAPS is a global atmospheric spectral model which, at the time this data set was created, was a 47 wave, 18 layer resolving model covering the globe (current version 3.2 is an 80 wave model). Spectral models resolve waves vice distinct grid points in their computations via Fourier transforms. The older version of NOGAPS had a coarser resolution than the current model (4.5 degrees of longitude) and orographic details (mountains) were not well resolved. Data sparse regions (like the Arctic) are filled in through an optimal interpolation process. The atmospheric model does make use of satellite imagery and buoy data (Wash, personal comunication). The current NOGAPS model is run at six hour intervals. At the time of the 1986 data set, however, it was run at twelve hour intervals. Originally the PIPS model was run once a day. An improvement in the ice model was noted when the model was upgraded to a six hour time interval to take advantage of the higher accuracy in the atmospheric fluxes from NOGAPS (Preller and Posey, 1989).

The forcing data included data necessary to derive the geostrophic winds and thermodynamic variables. The raw data fields included surface pressure fields in millibars (mb) for deriving geostrophic winds, surface vapor pressure in mb for deriving specific humidity, surface air temperature in degrees Celcius, solar radiation in calories per square centimeter per hour, and total heat flux and sensible heat flux also in the same units. The last three fields were used in determining the net long wave radiation.

Winds have a large influence on ice movement. The PIPS model originally ran with planetary boundary layer winds (marine surface winds); however, comparison tests between PIPS , free drift models (which use geostrophic winds), and buoy data showed that the boundary layer winds yielded less accurate results (Hibler and Tucker, 1986; Preller and Posey, 1989). As a result, the PIPS model was modified to use geostrophic winds derived from NOGAPS surface pressure fields. Geostrophic winds are used in the NPS model.

Monthly mean geostrophic ocean currents (cm/sec) and oceanic heat fluxes (meters of ice melted per month), also in gridded format, were derived from the H   er-Bryan (1984, 1987) coupled ice ocean model. This model is a climatological model which uses a three dimensional baroclinic ocean model (Bryan, 1969) coupled to a two layer dynamic-thermodynamic sea ice model (Hibler, 1979). The sea ice model supplies heat flux, salt flux, and momentum exchange for the top of the ocean. The ocean model supplies current velocity and heat exchange information to the ice model. Mean annual observed oceanic temperature and salinity data were used to weakly force the ocean model. This allowed the ocean model to be relaxed to available climatological ocean data, while allowing significant adjustment in the upper ocean layer as a result of effects of ice-ocean interaction. Currents due to surface stress were a part of the model predictions.

The resulting monthly ocean currents and ocean heat fluxes have significantly improved the ice model's ability to predict ice edge locations compared to constant heat flux ice models especially in the Greenland and Barents Seas (Hibler and Bryan, 1984; Preller and Posey, 1989). Figure 3.1 compares ice edges between a constant heat flux ice model and one that uses monthly oceanic heat fluxes. Preller (personal communication) has indicated that a three dimensional ocean model is under development for possible inclusion into PIPS in the future. Though winds have a much greater effect than ocean currents over short time scales, ocean currents can be a factor at long time scales (months to years) where the currents have an almost equal effect as winds for modelling ice movement (Preller and Posey, 1989) and at the ice edge where strong currents can advect heat to melt back the ice edge in a complex fashion.

B. READING IN THE DATA

The following section discusses how the raw data are converted and input for model use. Program codes for reading the data from tape and deriving the necessary forcing fields were provided by Ruth Preller and Pam Posey along with the raw data fields previously described. Using these programs separately from the model, the data were read from tape and converted to a form appropriate for use in the model and sent to mass storage files that could be called up by the batch processing component of the mainframe computer.

Surface pressure fields were converted into u and v components of geostrophic winds (as well as combined wind magnitude for heat budget calculations) through pressure gradients. A one degree Celcius correction was added to the surface air temperature fields to correct for an underestimate in the NOGAPS forcing fields (Posey, 1990). Specific humidity was calculated from the surface pressure and surface vapor pressure fields. Net long wave radiation was derived from solar radiation, total heat flux and sensible heat flux fields. Surface air temperature, geostrophic wind magnitude, specific

humidity, incoming solar radiation, and net long wave radiation were grouped into the atmospheric thermodynamic forcing terms for use in the model's heat budget routine. The u and v components of geostrophic wind and ocean currents were read in for use in the momentum balance portion of the ice model. Oceanic heat fluxes were read in to the ocean mixed layer portion of the model with a fixed mixed layer depth of 30 m coupled to the ice growth section of the model and brought into play after the atmospheric heat budget was determined.

C. UNITS AND PARAMETERS

The ice model was designed to run with all data fields in mks units. Where possible labels describing the units were placed in the model for better understanding for follow on users. Much of the forcing data had to be converted to mks units for use in the model and such changes are included in the program codes. Pressure fields were converted from mb to N/m^2. Geostrophic winds and oceanic currents are in m/sec. The heat fluxes were converted to W/m^2.

The parameters used in this model (Table 1) can have a large effect on the ability to accurately portray the ice floe characteristics properly. The ice strength parameters, P* and C, have been demonstrated to have a significant effect on ice thickness when varied (Owens and Lemke, 1990). Snow fall precipitation rates can also greatly affect ice thickness (more about this in the next chapter). Turning angles and coefficients affect ice motion through calculation of ice stresses. Their values were determined through studies by McPhee (1979) and others. The wind drag coefficient was determined through studies conducted on PIPS when its wind forcing fields were converted from marine boundary layer to geostrophic winds.

Table 1. ICE MODEL PARAMETERS.

| Parameter Name	Value
x-distance	127 km
y-distance	127 km
time step (dt)	4.32E+04 sec
Coriolis parameter	1.46E-04 sec^{-1}
Density of ice ρ_{ice}	0.91E+3 $kg\,m^{-3}$
Density of water ρ_w	1.0E+3 $kg\,m^{-3}$
Density of air ρ_a	1.3 $kg\,m^{-3}$
Density of snow ρ_{snow}	0.33E+3 $kg\,m^{-3}$
Thick ice cutoff h_o	0.5 m
Ice strength P*	2.75E+04 $N\,m^{-3}$
Compactness parameter C	20.0
Wind drag coefficient	0.8E-3
Water drag coefficient	5.5E-3
Air turning angle ϕ	25
Water turning angle θ	25
Reciprocal of heat of fusion	3.31E-9
Bulk sensible heat transfer coefficient	2.284
Water latent heat transfer coefficient	5.6875E+3
Ice latent heat transfer coefficient	6.4474E+3
Stefan-Boltzman constant	5.5E-8 $cal\,m^{-2}\,s^{-1}\,^{\circ}K^{-4}$
Conductivity of ice	2.1656 $W\,m^{-1}\,^{\circ}K^{-1}$
Albedo of ice	0.75
Albedo of water	0.10
Freezing temperature in the ocean	-1.96 $^{\circ}C$

(a)

(b)
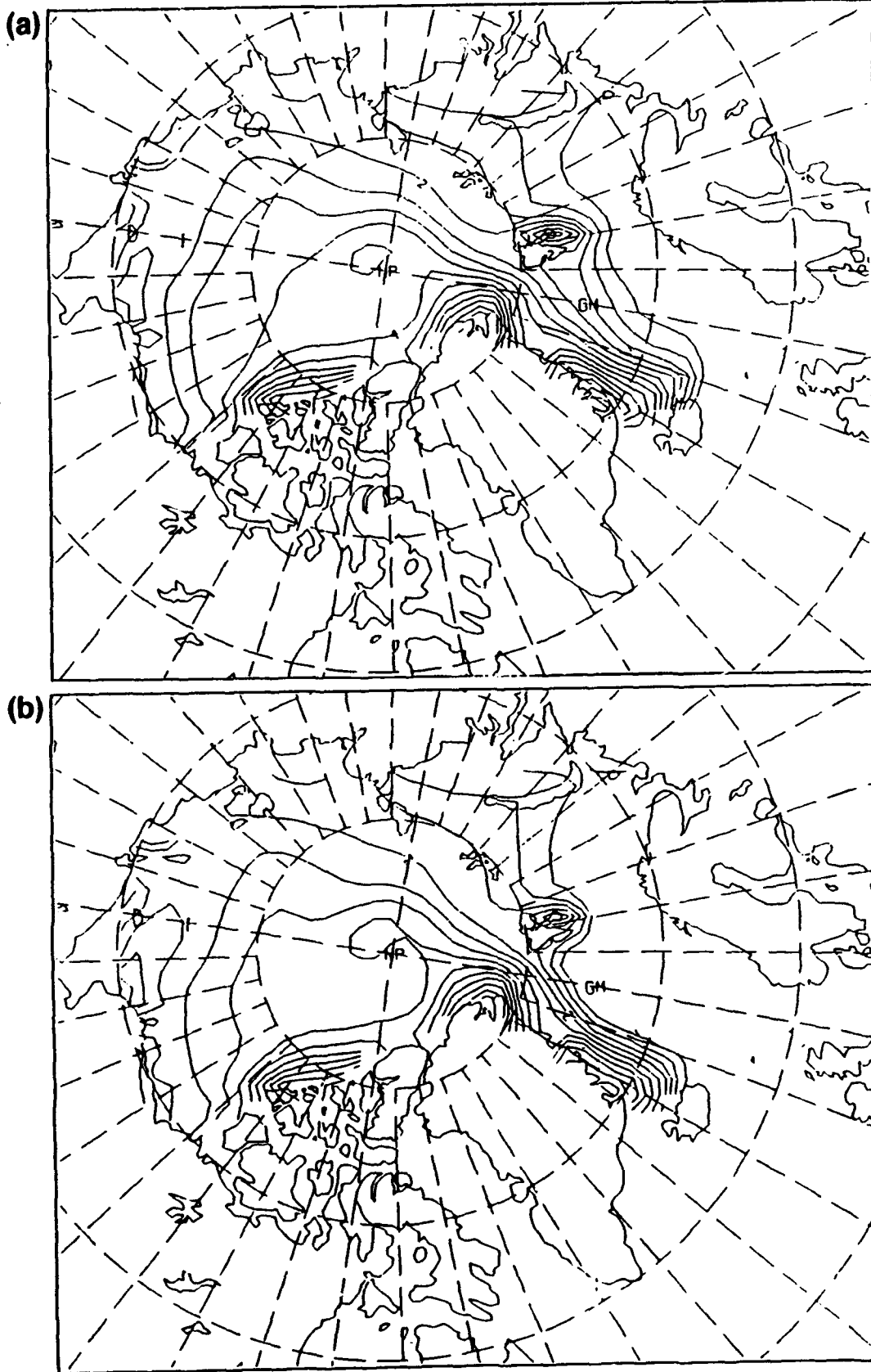
Figure 3.1 Model simulated thickness using (a) a constant oceanic heat flux of 2 W-m^2, (b) monthly mean Hibler-Bryan oceanic heat flux. The southernmost contour approximates the model ice edge. Contour interval is 0.5 m (Preller and Posey, 1989)

IV. RESULTS AND DISCUSSION

The ice model was initialized with a uniform ice thickness of 3 m, an ice concentration of 100 percent, ice velocity of nearly zero, and air temperature at freezing over most of the model domain except for the southern Greenland and Norwegian Seas where ice concentration is zero. The model was allowed to "spin up" to a stable condition for a period of 3 years using the 1986 data input forcing fields described previously. At the end of each year period the model output was placed in a restart file for use in the next year's run. Analysis of the total ice volume and ice extent of preliminary runs showed that the model stabilized fairly rapidly in the latter part of the first year and throughout the second year. The remainder of this chapter is focused on the analysis and discussion of the results from the last (third year) run of the ice model. This involved examining the ice model output ice drift rates, ice extent, and ice edge concentration and comparing them to ground truth data for the same time period. Ice thickness, also an ice model output, has no independent equivalent measure for comparison so only a qualitative description will be given where necessary.

A. ICE EXTENT

The actual sea ice area within a given basin as defined by Comiso (1990) is the sum of the products of the area of each data element or grid cell and the corresponding ice concentration (in which $0 < A < 1$) of that grid cell. Ice extent is defined as any area that contains 15 percent or greater ice concentration (Parkinson et al., 1987). Ice extent includes areas of open water such as leads and polynyas whereas ice area considers only that part which is ice. Articles by Parkinson and Cavalieri (1989), Zwalley et al. (1987) Comiso (1990), and Gloersen and Campbell (1988) have noted an annual oscillation in ice extent that is fairly stable (see Figure 4.1). During the summer the ice area is on

33

average observed to be about 78 percent of the ice extent in the Arctic basin (Comiso, 1990).

Ice model runs conducted during this study showed a seasonally varying ice extent that had a maximum of $9.41 \times 10^6 km^2$ at day 130 (10 May 1986) and a minimum of $7.3 \times 10^6 km^2$ on day 260 (17 September 1986) or a 22 percent change in ice extent. The modeled ice extent is plotted in Figure 4.2. These values are compared to those determined from a study conducted by Parkinson and Cavalieri (1989) using satellite passive microwave energy which estimated the sea ice extent both regionally and over the entire Arctic region. A combination of regions including the Arctic basin, Kara, Barents, and Greenland Seas approximated the NPS sea ice model's domain. The Parkinson and Cavalieri maximum ice extent was found to be $10.15 \times 10^6 km^2$ and minimum ice extent $7.59 \times 10^6 km^2$ or a 25 percent change in ice extent. The difference between maximum ice extent values ($0.74 \times 10^6 km^2$ or 8 percent) is a result of the difference in the size of the areas under consideration. The southern portions of the Greenland, Kara, and Barents Seas are not included in the ice model domain, thereby reflecting a smaller maximum. The difference between minimum ice extent values ($0.29 \times 10^6 km^2$ or 4 percent) is consistent with the difference in maximum ice extent in that the ice model domain encompasses less area than the satellite coverage. The smaller difference during the period of minimum ice extent is reflected in the fact that more was ice melted outside the model domain than was melted inside.

Figure 4.3 is a plot of the model ice area. On day 130 (10 May) the ice area is $9.02 \times 10^6 km^2$ or 4 percent less than the ice extent. On day 260 (17 September) the ice area is $5.74 \times 10^6 km^2$ which is 21 percent less than the ice extent, similar to the summertime difference reported by Comiso (1990).

Figure 4.4 is a plot of the model ice volume which is the summation of the product of the thickness of each grid cell and the ice area of that cell. The maximum ice volume

occurred on day 130 (10 May) with a value of $32.09 \times 10^3 km^3$ which equates to an average ice thickness of 3.55 m. The minimum ice volume occurred on day 260 (17 September) with a value of $19.47 \times 10^3 km^3$ which equates to an average ice thickness of of 3.46 m. Discussions with Ruth Preller (personal communication) indicated that the NPS ice model's thickness was a little larger (up to 0.5 m of thickness difference) than similar runs with PIPS. A possible reason was that the NPS ice model was run without a snow layer which allowed thicker ice to grow due to a lack of insulation, and which subsequently was not melted as fast as thinner, snow-covered ice might have been. Also in support of the snow argument is the finding by Owens and Lemke (1990), who noted in Weddell Sea runs of the ice model, that the presence of snow substantially lowered the summer minimum ice extent.

B. COMPARISON OF MODELLED ICE DRIFT TO BOUY DATA.

The ice model drift rates or ice velocities were studied in a qualitative manner under several different environmental conditions such as calm or light winds, strong storms, large broad pressure gradients, gyre reversals, and minimum and maximum ice conditions at selected geographic regions. The focus was to see how the ice motion behaved under each of these conditions. Ultimately seven cases were selected for comparison. Each is described below. The modeled ice drift rates were compared to Arctic buoy drift information. These buoys, part of the Arctic Ocean Buoy Program first established in 1979, are dropped in the Arctic ice pack, and stay with the ice until it melts or departs the Arctic region. Buoy postions, as well as pressure and temperature, are relayed via System ARGOS to a processing center where drift rates and pressure fields are derived (Thorndike and Colony, 1980). The results of this data processing are described in annual reports; the 1986 results are in Colony and Rigor (1989).

Since the buoys are not uniformly distributed throughout the Arctic basin, comparisons between the ice model and buoy drift rates were restricted to those areas of the

Arctic where the buoys we present. Buoy drift rates were determined directly from the plots of buoy drift and surface pressure fields provided in the reports, where 1 cm was equal to 20 km per day or 23.1 cm/s. The ice model drift rates were measured directly from the vector plots of the model output data in which a 5 cm/s, 10 cm/s, and 20 cm/s scale was provided on each plot. General descriptions of buoy direction were made relative to the surrounding geographic features and prevailing winds.

It is important to note that a perfect correlation between buoy and model ice drift rates is not expected to be exact since the pressure analysis fields depicted in the buoy reports do not exactly match the NOGAPS surface pressure fields used to drive the ice model. The plotted surface pressure fields in the buoy reports were derived directly from the buoy measurements and additional observation stations around the periphery of the Arctic. The NOGAPS pressure fields are derived from a combination of data sources. These sources include the measurements taken from the buoys, satellite temperature soundings, satellite cloud winds, the previous time period's pressure analysis, and direct observations from ground based and air observation stations. These diverse inputs are weighted as to their accuracy as they are incorporated and smoothed into the NOGAPS analysis for the most complete and accurate analysis possible (Wash, personal communication). Though NOGAPS pressure would be expected to be more accurate than buoy pressures alone, there might be instances where buoy-derived pressure fields pick up a weather feature that was missed or smoothed out of the NOGAPS processing. Generally, in most cases the buoy pressure fields and NOGAPS will show similar weather patterns over the Arctic.

An exagerrated or extreme example of this difference is illustrated in Figures 4.5 and 4.6. Figure 4.5 is a plot of the surface pressure and buoy trajectories typical of plots from the Arctic buoy reports. It shows that the eastern Arctic is dominated by one low pressure center north of Svalbard. Figure 4.6 is a plot of the geostrophic wind trajecto-

ries derived from the NOGAPS pressure fields for input into the ice model. Since the winds are geostrophic, their direction can be equated to isobars of pressure. What can be seen from this figure is that there are two low pressure centers (vice one) depicted by the NOGAPS data; with one north of Svalbard and one north of Ellsmere Island in the Canadian Archipelago. The presence of these two cyclones is reflected in the model ice drift trajectories (Figure 4.7) which also show the two cyclonic vortices in the ice movement. Figures 4.6 and 4.7 illustrate the importance of accurately portraying the wind fields for modelling ice movement since the ice flow pattern predominately mirrors the wind flow pattern above it. This is especially true for regions dominated by high wind speeds.

1. Case One: Decreasing High Wind Conditions

This case study examines the ice model's ability to model ice movement under declining wind speed conditions; specifically to see if a time lag occurs between wind speed changes and subsequent ice motion. The region examined considers only one side of the Arctic, i. e., north of the coasts of Alaska, the Canadian Archipelago, and Greenland where the buoys for this case study are clustered. Figure 4.8 (a,b,c,d) shows the prevailing wind conditions over the Arctic region and the buoy trajectories for the period 18-21 January 1986. Strong winds were prevalent over the region where the buoys were located as a result of an interaction between a high pressure center over the western Arctic and a low pressure center stalled over Greenland. These high winds steadily decreased in intensity through 21 January as the low filled and moved eastward out of the area.

The buoy drift rates reflected these high winds reaching velocities as high as 24 cm/s north of Ellsmere Island on the 18th, but declining thereafter on each successive day (16 cm/s on the 19th, 9 cm/s on the 20th, 3-7 cm/s on the 21st). A large drop in buoy speed between the 19th and 20th occurred even though the su: ace pressure gra-

dient was still fairly strong at that time; however, it is noted that ice was moving toward the coast at the time. The buoy trajectories indicated that on the 18th to 20th the ice was moving pretty much as a unit but by the 21st shear zones must have formed as the ice north of Ellsmere had come to a stop while ice near Alaska and Greenland continued moving.

The modeled ice drift output for the area where the buoys were clustered during 18 and 19 January exhibited the same type of westward ice flow north of the Canadian Archipelago as the buoy trajectories. Good agreement in trajectory direction is noted but the model indicated higher speeds (up to 38 cm/s on the 18th, 23-38 cm/s on the 19th). On the 20th the wind backed forcing the ice and buoys to a more southerly course toward the coast (Figure 4.8.c) but remained essentially unchanged in the ice model simulation (Figure 4.9). Model trajectories were as large as 45 degrees to the right of the buoy drift tracks. The ice model simulation continued to follow the wind flow pattern shown in Figure 4.10 with modeled ice drift speeds of 20-25 cm/s near Ellsmere Island. By the 21st the model ice drift had changed to a more southerly direction toward the coast and its speed had decreased to 10 cm/s (Figure 4.11). In comparison, buoys in this area had already stopped moving by the 21st (Figure 4.8.d), but 12 hours later (one model time step) the model ice drift had also stopped moving. This would seem to indicate a 12 hour time lag in the response of the model to decrea.ing wind speeds, possibly indicating that the effects of friction and ridging in reducing momemtum are parameterized weaker than they should be. In summary, during high winds, the model speeds are slightly too fast. A delay of one day in the model to shift the trajectory to the south vice southwest, and a 12 hour delay in response to decreasing wind speed is also noted.

2. Case Two: Light Wind Conditions

This case study examines the ice model's performance under the absence of any strong wind forcing. There were several occasions for which the winds over the Arctic basin were calm. Figure 4.12 (a,b,c,d) shows the pressure field and buoy trajectories for 18-21 February 1986, a period of generally calm wind conditions resulting from an absence of any strong pressure gradients. The buoys were located mostly clustered in the same location as in the previous case but also with two buoys located north of Bering Strait. Generally little buoy movement was noted during this time period except near the Alaskan coast where buoy speeds varied from 4 to 7 cm/s. Little directional movement is noted.

During this period the ice model exhibited slow movement of the ice field with speeds under 5 cm/s. Figure 4.13 is the model ice drift for 19 February. It shows very slow ice drift rates except in the vicinity of Svalbard (the result of a low pressure system) and a small area where ice is being driven towards the Alaskan coast. The NOGAPS winds (Figure 4.14) driving the ice model show wind speeds less than 10 m/s over the Arctic basin except as previously mentioned. The ice model drift rates for the 19th compare favorably with the buoy trajectory drift rates for this date; however, considerable difference in the direction of flow between ice model and buoy trajectories was noted. The buoys demonstrate a westward drift in the area north of Greenland and Ellsmere, while the model exhibited a more northerly direction indicating a directional difference of 90 degrees to the right of buoy drift. The ice trajectories appear to be generally following the wind pattern in this location.

In comparing the light forcing from wind fields to the model ice drift there appears to be some agreement in that light winds generated very little ice motion. There is considerable variability in direction however, also a reflection that under lighter wind stress other components of the momentum equation such as ocean currents, Coriolis

39

force, and internal ice stress exert a larger effect on the ice drift than during periods of high wind stress. Also at lower wind speeds the turning angle between wind and ice is expected to be larger which would create a large difference in direction between wind and ice motion.

Calm conditions also existed on 1 March, 21 March, and 31 March 1986 as well. The modeled ice drift speed was in agreement with that indicated by the buoy drift report. As before, under these light wind conditions, the buoy and modeled ice floe trajectories were highly variable from day to day. Considerable differences in direction of drift existed between the buoy reports and the model output with ice motion varying as much as 45 degrees to the right or left of buoy drift direction. In summary, under light wind conditions ice model speeds are handled well but direction is poor with disagreement in excess of 45 degrees. Direction did vary to either the right or left of buoy direction.

3. Case Three: Gyre Reversal

One of the better known features of the Arctic basin circulation is the anticyclonic rotation of the Beaufort Gyre in response to the atmospheric high pressure center resident over it throughout most of the year. During the summer, however, the gyre rotation is reversed by the action of storms or atmospheric low pressure centers that move into the area (McLaren et al., 1987; Serreze et al., 1989). This case study looks at the ice model's ability to respond and depict this gyre reversal. The 1986 buoy reports show several instances of gyre reversal, two of which occurred on 12-17 June (Figure 4.15) and 26 July to 1 August(Figure 4.16), respectively. The buoys are located in an area extending from Bering Strait to Ellsmere Island. On 12 June the buoy trajectories show a clockwise rotation with a drift rate of 7 cm/s off the coast of Alaska which was associated with an atmospheric high in the area. By 15 June a developing low had moved into the area and begun turning the ice counter-clockwise near the Canadian

40

Archipelago. Peak reversal occurred on 16 June with velocities reaching 20 cm/s. This change in buoy drift indicates that the movement of ice appears to be strongly tied to the large scale wind forcing.

For the period of 12-17 June the ice model closely followed the ice flow pattern depicted in the buoy drift reports. The modeled ice drift for 12 June (Figure 4.17) demonstrated a similar anticyclonic rotation of the gyre off Alaska to the one depicted in the buoy report but at speeds of 2 to 3 cm/s less than the buoy drift rate. Both the model and buoys showed little or no ice movement near the Canadian Archipelago. By 15 June a developing low had begun to turn the ice cyclonically. Again the buoy reports displayed buoy drifts that were a little faster (2 to 3 cm/s) than the modeled ice drift; the same was true for the 16th. On the 17th the model ice speed increased becoming similar to that reported by the buoys (Figure 4.18) possibly indicating a slight lag in speed of 2-3 cm/s. At this time the gyre reversal was fully developed with the ice off the Alaskan coast moving at approximately 16 cm/s toward the coast. Off the Canadian coast ice was moving northwestward away from the coast at approximately 4 cm/s.

Another gyre reversal took place on 26 July to 1 August (Figure 4.16). The buoys were distributed over a wide area of the western Arctic basin from Siberia to just north of Greenland. On the 26th the ice was rotating in a clockwise manner off the coast of Alaska at 7 cm/s in response to a weak high pressure ridge in the vicinity. By 28 July a developing low began turning the ice counter-clockwise. This pattern persisted through the 3rd of August with drift rates up to 14 cm/s. The modeled ice drift on 26 July showed similar drift speeds and an anticyclonic trajectory with ice floes moving up to 10 cm/s off the coast of Alaska, and varying between 5 and 7 cm/s elsewhere (Figure 4.19). The modeled ice drift did not show a complete gyre but did show a clockwise turning of the ice. The model matched the buoy reports in showing the counter-clockwise turning of the ice commencing on the 28th of July in the presence of a devel-

oping low showing no lag in response time. The ice model speeds and directions closely matched those of the buoys. Speeds up to 17 cm/s were indicated off the eastern Siberian coast by both the buoy data and the model. The model picked up the sharp clockwise turn in ice drift direction north of the Bering Strait which was reflected in the buoy reports. Around the center of the growing cyclonic gyre, model drift speeds of 12 cm/s were measured which was close to the 14 cm/s measured from the buoy reports. Like the buoy reports, the modeled cyclonic gyre persisted in the presence of the storm showing good agreement in speed and direction. By 1 August the counter-clockwise (cyclonic) gyre had come to clearly dominate the central Arctic basin (Figure 4.20). The ice model indicated drift rates that were 2 to 3 cm/s higher than the comparable buoy reports but directions of movement were similar.

The model response to both gyre reversals was virtually immediate and matched the movement of the buoys. The small difference in speeds between model and buoy was possibly a reflection of errors in the wind forcing fields. Differences in direction were also small but the model ice floe pattern closely matched the buoy trajectories. Both the model output and the buoy report for 1986 appear to indicate that the cyclonic nature of the Beaufort Gyre was more of a transitory feature in the ice pack rather than a persistent one lasting throughout the summer. The gyre shows up more clearly when a storm stalls over the basin permitting more energy to be pumped into the cyclonic circulation. In summary, the ice appears to follow the movements and direction of the wind more than any other factor.

4. Case Four: Large Strong Pressure Gradient

This case study examines the model's performance under high wind conditions resulting from a strong surface pressure gradient, i. e., under conditions when the wind velocity is already high. A subsequent case study will examine the model response to a growing storm.

42

Examples of strong gradients were selected that covered a large portion of the Arctic basin to see how the model handled large scale movements of ice. One such example was during the period of 7-12 April (Figure 4.21) when a strong storm off the coast of Siberia had developed in the vicinity of the Kara Sea. This created a large, strong gradient pattern over much of the Arctic basin, especially in the eastern portion. The buoys at this time were mostly on the opposite side of the basin and on the periphery of the storm, but its effects on the ice movement could be discerned and compared to model results. Prior to April 7, buoys and model output indicated that much of the ice pack was motionless (except at the edges) with calm wind conditions prevalent. On the 7 April a sudden increase in ice movement was observed as the result of the storm. Between Svalbard and Greenland the buoy drift speed was measured at 16 cm/s. Closer to Ellsmere Island buoy drift rates attained values between 7-12 cm/s, and 2-4 cm/s near Alaska. The ice flow pattern paralleled the pressure contours. Figure 4.22 shows ice model drift trajectories for the 7 April. Model ice drift rates in the vicinity of the buoy near Svalbard showed speeds of 14 cm/s with an approximately 10 degree difference in direction to the left of the buoy direction. This difference is probably the result of inadequately modeling the flow of the strong East Greenland Current, i. e., the model uses monthly oceanic currents. North of Ellsmere model drift speeds of 11 cm/s were measured with a general agreement with buoy velocity direction. Modeled ice drift near Alaska matched buoy drift trajectories in the same area.

By 8 April (Figure 4.23) a wider area of the ice pack was influenced by the storm as it moved eastward. Both the model and buoy reports showed drift rates reaching 25 cm/s west of Svalbard, up to 14 cm/s north of Greenland, and 5 cm/s near Alaska. Modelled ice drift direction appeared to generally agree with the buoy trajectories showing a piling up of ice on the north Greenland coast and a southerly flow between Greenland and Svalbard. By 10 April the low had begun to fill and the pressure gradient

43

had begun to weaken. The buoys and model both output show drift rates of 9 cm/s for ice in the central Arctic. West of Svalbard the buoy had slowed to 14 cm/s and the model output reported 12 cm/s. Near the Canadian Archipelago the buoy reports showed very little movement of the thick ice; however, the model continued to indicate a 5 to 7 cm/s movement of ice in this area. By 12 April the pressure gradient resulting from the storm had virtually disappeared and calm wind conditions prevailed. Most buoys showed little or no movement; however, the model persisted in showing some movement off the Canadian coast of 3 to 4 cm/s which was consistent with the earlier case studies which demonstrated a 12 to 24 hour lag time in response to decreasing winds and ice velocities. Elsewhere the model agreed with the buoy reports.

Two other instances of strong gradients resulting from storms occurred on 27 September and 27 October and are reflected in the buoy reports. On the 27th of September (Figure 4.24) a strong pressure gradient extended from the Siberian coast to Greenland. Buoy drift rates of 14 cm/s near the high gradient region were recorded the with model output (Figure 4.25) for the same area exhibiting a similar ice drift rate and direction. In the center of the high gradient region modeled drift rates were calculated up to 18 cm/s. Near the Canadian Archipelago where the pressure gradient was weak the buoy reports showed little or no movement.

On the 27th of October (Figure 4.24) the surface pressure gradient extended from the northern Scandinavian coast to Alaska, cutting a wide swath through the central Arctic basin. Buoy drift rates were measured at 12 cm/s in the middle of the high gradient region; the model drift rates under these high wind speed conditions were overestimated by 3 cm/s (Figure 4.26). Near the Canadian Archipelago the buoys and model were in good agreement showing little or no movement. The ice flow direction from the model and the buoy data were a close match.

Overall in these different examples of strong pressure gradients the ice model performed well in matching the general flow pattern of the buoy drift trajectories. Differences in drift speed between between the model and buoys was not consistent with the modeled speed sometimes being higher or lower than buoys in the same area. The speed difference was never more than 2-3 cm/s and may be the result of the spatial resolution of the NOGAPS forcing fields not being able to completely match the local weather conditions over the data-sparse Arctic.

5. Case Five: Large storms

This case study examines the ice model's response to a growing storm or increasing wind flow pattern. Case One had noted a time lag of 12 hours under decreasing wind speed conditions. There were several large storms in 1986 and their impact on the ice pack could be seen on many occasions in both the buoy data reports and the ice model output. Examples of storms or low pressure centers were selected that were for the most part entirely contained within the Arctic basin with the idea of examining the cyclonic ice flow circulation generated by the storm. The pressure gradients generated by the storms investigated in this section were generally of smaller scale and more circular than those of Case Four. Storms that occurred on 16 to 19 August, 16 December, and 19 June will be discussed.

During the period of 11-15 August generally calm wind conditions prevailed over the Arctic with only modest ice drift rates of 5 to 7 cm/s being observed. On 16 August a large storm developed in the western Arctic basin creating a large cyclonic rotation of the ice (Figure 4.27). The storm's impact on the ice pack was immediate and this was reflected in both the buoy report and ice model output. Buoys located throughout the storm region displayed a cyclonic circulation recording drift rates as high as 18 cm/s in the strongest part of the storm and reducing to 14 cm/s toward the outside of the vortex. Near the center of the low one buoy was measured with a drift speed of

7 cm/s. The modeled ice drift rates (Figure 4.28) showed magnitudes as high as 17 cm/s in the same area as the buoy located in the strongest part of the storm. Near the center of the storm, buoy and modeled drifts indicated speeds of 6 cm/s. On the back side of the storm near the Siberian coast, buoy and model drift rates indicated speeds of 12 cm/s. The ice model drift directions compared well with buoy trajectories staying within 10 degrees of the buoy direction and usually to the left of the buoy direction. This result indicates the model trajectories more closely follow the pressure contours, an indication of the dominant influence of wind forcing relative to other forcing terms, i.e., the oceanic stress and internal ice stress may have been too weak. Though there were no buoys in the center of the low, the model correctly showed little movement at the center with speeds increasing toward the outside up to 22 cm/s (in areas other than where buoys were located). Overall the buoy drift and modeled ice drift agreed well with each other in both direction and speed, and showed an almost immediate response to the presence of the storm.

The storm continued to dominate the western Arctic during 17 and 18 August with buoy and model trajectories continuing to agree. Both indicated ice drift rates of upwards of 23 cm/s in the cyclonic vortex set up by the storm and less movement near the thicker ice of the Canadian Archipelago. By 19 August (Figure 4.29) the storm had begun to weaken with buoy reports showing speeds of 12 to 16 cm/s with the highest speeds occuring near the Alaskan coast. The model also indicated speeds of 12 to 20 cm/s with the highest drift rates off Alaska. The ice drift directions continued to remain in agreement between model and buoy except for a region near Siberia where a 45 degree difference to the left in heading was observed between the buoy and ice model drift. The buoy reports showed the buoys heading toward the Siberian coast while the model trajectory direction indicated that the ice was still caught up in the cyclonic circulation. This may be similar to the calm wind condition previously discussed where the drift di-

rection is highly variable at low wind speeds The speed of both reports w∷ 5 cm/s; a fairly slow speed. This difference may have been the result of a small scale weather feature in a data-sparse region that was smoothed over by NOGAPS but was picked up by the buoy drift. With the Arctic being such a data-sparse region there will always be a limitation on the accuracy of NOGAPS and PIPS to accurately predict ice movement.

On 16 December (Figure 4.30) a large storm was centered just north of Canada. It had a large effect over much of the Arctic basin setting up a cyclonic flow pattern in the Canadian basin. This storm resembles some of the large gradient features discussed in Case Four. But, unlike the previously discussed storm, this storm generated some movement of the thick ice near the Canadian Archipelago. This was detected by both the buoy reports and the ice model (Figure 4.31). Ice velocities of up to 17 cm/s were indicated by both the buoy drift and the ice model. Near the Canadian Archipelago both also indicated a general offshore direction of the ice drift. Where the storm pressure gradient was strongest the buoy reports indicated speeds up to 18 cm/s and the model had speeds up to 20 cm/s for ice drift. One buoy near the center of the storm exhibited an anomalously high drift rate of 14 cm/s, a speed inconsistent with its location in the buoy-derived cyclonic vortex. However, it matched the model drift speed and direction which suggests that the storm center was correctly placed farther west by NOGAPS. In the Beaufort Sea region (near Alaska) buoys flowing back toward the Canadian Archipelago were measured to be moving at speeds up to 12 cm/s. However, the model indicated slower speeds of 8 cm/s for the same area. The speed differential may be the model's attempt at parameterizing the effect of piling up of ice or a secondary anti-cyclonic circulation working to reduce the eastward drift.

An example of a summer storm occurred on 19 June where it was centered in the western portion of the Arctic basin (Figure 4.30). Generally calm wind conditions prevailed everywhere in the Arctic except in the immediate vicinity of the storm. This

is reflected in the buoy trajectories and model output. Figure 4.32 shows little ice movement outside the immediate storm area. Inside the storm area itself, speeds up to 24 cm/s are indicated by both the ice model and buoy drift rates with good agreement in direction. The high speeds generated may be the result of thinner ice at lower concentrations during this time of the year allowing less restriction in movement.

6. Case Six: Comparison at Maximum and Minimum Ice Extent

This case study compares model performance and behavior of ice drift at its maximum and minimum ice extent. The maximum ice extent occurred near 20 May and the minimum ice extent occurred near 17 September. The region to be examined extended from Alaska to Ellsmere Island where most of the buoys were located during both ice extent periods. Figure 4.33 shows the buoy and pressure fields for 20 May and '7 September. Though mostly light wind conditions prevailed some significant differences in the weather pattern is noted between the two dates. On 20 May a weak high pressure center was positioned north of Alaska. On 17 September a slight low pressure center was found north of the Canadian Archipelago. This resulted in buoy drift trajectories moving in somewhat opposite directions on these two dates.

What is interesting to note is that the wind forcing for both dates was under 10 cm/s for the area. Even though the wind forcing was similar on these dates the magnitude of the buoy drifts differed. On 20 May the buoys near Ellsmere Island were stationary while the buoys in the Beaufort Sea were moving westward at 6 cm/s. On 17 September the buoys near Ellsmere Island were moving eastward at 11 cm/s and a buoy near Alaska had a drift rate of 14 cm/s. This difference in speed is most likely related to the reduced ice concentration in summer and relatively thinner ice at this time with more leads and polynyas present in the ice pack. This allows for greater movement of the ice than would be permitted during a period of maximum ice extent.

48

Figures 4.34 and 4.35 depict the ice model drift trajectories for 20 May and 17 September, respectively. On 20 May the modeled ice drift rates were very slow throughout most of the basin, not attaining the velocities registered by the buoys in the Beaufort Sea. In the absence of strong winds the model does not move the ice much when the ice extent covers most of the basin. Very little can be said about the drift direction due to the slow rate of drift other than the direction is highly variable as the lesser effects of ocean currents and internal stress begin to more dominantly influence the ice drift. On the other hand the ice model performed well on depicting the ice drift on 17 September. The ice was moving a lot freer matching the buoy drift rate and direction with speeds of 11 cm/s eastward along the Canadian coast. The model also matched the 14 cm/s speed and direction of the buoy off Alaska on the 17th. Generally the model performed better during the period of minimum ice extent when free drift conditions were predominant.

7. Case Seven: Ice Movement in the Greenland Sea

This case examines model performance in the Greenland Sea area. No buoys are available for comparison however so this discussion will primarily be an observational one, looking at ice flow patterns. Figure 4.36 is the modeled ice drift for 23 January 1986. The group of high velocity vectors in the lower left represent ice flow in the East Greenland Current (EGC) near the ice edge jet with speeds in excess of 30 cm/s. Such high speeds are nearly always present as a result of the baroclinic flow caused by the strong East Greenland Polar Front (EGPF). Ice drift rates along the Greenland coast but well removed from the EGPF reach speeds up to 10 cm/s. Enhancing these high speeds was a storm located in the Norwegian Sea off the east coast of Svalbard which generated a strong atmospheric pressure gradient parallel to the axis of the EGC.

The modeled ice drift in the Greenland Sea can be highly variable depending on the prevaling weather as Figure 4.37 illustrates. Here the ice along the Greenland coast

has slowed almost stopping with no specific direction or drift. Away from the coast near the ice edge, a strong flow to the north is depicted. This is an example of the model basically failing to depict the ice drift in this area. The effect of the EGC is completely missing in this case. The ice movement appears to be tied more to the forcing of the wind than to the ocean current. The spatial resolution of 127 km for this basin-wide ice model is incapable of resolving the narrow jet like features of the EGC. Also monthly ocean currents are used to drive the model which also reduces resolution in a temporal sense.

C. ICE EDGE COMPARISONS

The location of the ice edge boundary calculated by the model was compared with that determined by the Naval Polar Oceanography Center (NPOC). Sea ice analysis ice edge locations, identified on a weekly basis by NPOC, are based on a compilation of satellite imagery, aircraft reconaisance, and direct observations by reporting stations on land and sea (NPOC, 1986). The comparison that follows is restricted to the eastern Arctic to take advantage of its high climatic variability and the fact that it lay entirely within the ice model domain. The ice edge will be compared for 5 different time periods: 11 March representing late winter; 20 May, the time of maximum ice extent; 8 July, the middle of the summer and time of maximum melt rate; 16 September, the time of minimum ice extent; and 25 November, the middle of autumn and a time of rapid ice growth.

On 11 March (Figure 4.38) the ice edge extended from the east coast of Greenand at 65°N to the western tip of Spitsbergen at 78°N and then extended around the southern tip of the island at 75°N, eastward to Novaya Zemlya, and then southward to the Kola peninsula. The modeled ice concentration for 11 March (Figure 4.39) appears to extend far south (an average of 180 km) of the actual ice edge line. The model ice edge appears to almost reach the northern coast of Scandinavia. The 50 percent concentration line appears to more closely match the real ice edge than any other ice concen-

tration level. One item of note is that the 40 percent and higher concentrations do recede back a little on the western side of Spitsbergen reflecting the presence of the warm influx of the West Spitsbergen Current indicating that the model is at least partially handling this heat flux correctly. The most likely explanation for the improper southerly projection of the ice edge is the use of climatology-derived oceanic heat fluxes which do not take into account the actual oceanic forcing. Also a factor is the large spatial resolution (127 km) which can not resolve the ice edge which frequently is less than 50 km wide, especially during periods of on-ice winds.

On 20 May the ice was at its greatest extent (Figure 4.40). The NPOC report indicated that the location of the ice edge was similar to that of 11 March, with the main difference being higher concentrations of ice inside the ice edge, especially between Spitsbergen and Novaya Zemlya. As in the previous case, the modeled ice edge (Figure 4.41) appears to extend south of the actual ice edge by approximately 120 km east of Spitsbergen and 180 km west of Spitsbergen. The 90 percent concentration line seems to best approximate the real ice edge.

By 8 July (Figure 4.42) the ice edge had begun to recede with the west coast of Spitsbergen and the southern coast of Novaya Zemlya becoming ice free. Open water was present above 80°N near Spitsbergen and the ice concentration near the ice edge between Spitsbergen and Novaya Zemlya had decreased to 30 percent. The modeled ice edge (Figure 4.43) had also receded northward but was still south of the actual ice edge by 100 km. The model shows incorrectly that the west coasts of Spitsbergen and Novaya Zemlya are ice bound (at least partially) and the warm influx of the WSC is not observed.

By 16 September the ice extent had reached its minimum. The ice edge depicted in Figure 4.44 starts at the eastern Greenland coast at 74°N and extends northeastward above Spitsbergen over to Franz Josef Land and then eastward to the northern tip of

Novaya Zemlya. Spitsbergen and Novaya Zemlya are virtually ice free. Low concentrations of ice extended deep into the Arctic. The model ice edge (Figure 4.45) was still 70 km south of the actual ice edge but it compares better this time. Spitsbergen and Novaya Zemlya are correctly shown to be virtually ice free and ice concentrations are down throughout the Arctic basin. The model still has difficulty representing the warm intrusion of the WSC west of Spitsbergen.

Figure 4.46 depicts the location of the ice edge on 25 November, examined for this period of rapid ice growth. The ice edge originated from the eastern Greenland coast at $65°N$ and extended to the northwestern tip of Spitsbergen and ran northeastward toward the northern tip of Novaya Zemlya. It picked up again at the southern tip of the island and extended over to Siberia. For this period of ice growth the ice model (Figure 4.47) correctly depicts the ice edge. It still tends to be too far south by 40 km but it is closer than the previous cases. The model seems to correctly reflect the warm heat flux of the WSC.

Overall, the ice model appears to do a better job of predicting the ice edge in the later part of the year (late summer,fall, early winter) than the first part of the year. Preller (personal communication) has indicated that PIPs behaves in a similar manner. Also of note is that PIPS is currently updated weekly with ice edge reports from NPOC and so never strays very far from the actual ice edge in the course of the week (Preller and Posey, 1989).

D. DISCUSSION

The main focus of this ice model study was to compare modeled ice drift to ground truth data using buoy trajectories in a qualatative manner. Ice drift and ice flow patterns were examined under a variety of environmental and forcing conditions at different locations. The entire ice field was not examined in detail; only that portion where buoys were present was studied (the exception being the Greenland Sea). Model performance

was studied under decreasing wind speed conditions, increasing wind speed conditions, steady state light or calm winds, steady high winds resulting from strong large pressure gradients, and gyre reversals.

The model performed well in depicting the general ice flow patterns in the central Arctic basin. Here wind forcing exerted the greatest influence on ice drift. This was reflected in both the ice model and in the buoy reports.

Some trends noted from the case studies are listed below. Under high wind speed forcing the ice model response was immediate and yielded an accurate depiction of the ice flow. Model speed differences varied 2 to 3 cm/s above and below the buoy drift speed. A 12 hour time lag (one time step) was noted for ice drift rates to slow during decreasing wind conditions. This probably resulted from an excessive build up of momentum from the movement of ice. No time lag was observed for rapid increases in wind speed (resulting from a moving or developing storm). Model response was immediate under these conditions. However, running the model at a shorter time step might detect the presence of a time lag. The response to the summer reversal of the Beaufort Gyre was also immediate.

Outside of areas of strong wind forcing the ice drift speed rapidly decreases, as in the 19 June storm, where the only ice moving was that located near the low pressure center. Under light or calm wind conditions, generally under 10 m/s, the ice model drift is generally very slow and highly variable in direction. Also at this level of forcing other factors in the momentum balance equation exert more of an influence such as ocean currents and internal ice stress. Floes in areas of thinner and less concentrated ice tended to move faster than in areas of thicker and more concentrated ice.

Some ice model differences with the buoy drift trajectories could be attributed to the inaccuracies in the NOGAPS pressure fields that drove the model. Instances were present where both pressure fields missed a small scale weather or oceanic circulation

feature indicated by the buoy drift pattern. Generally the pressure fields provided a reasonable depiction of the wind forcing. There were some trends in modeled ice drift direction as well. At low wind speeds the model had difficulty in assessing direction. Errors in excess of 45 degrees were noted. A possible reason is that oceanic forcing becomes important at low wind forcing and the data base for this is monthly climatology with poor spatial resolution. At high wind speeds, on the other hand, the model performed well generally remaining within 10 degrees of buoy motion. Accuracy now depends on the accuracy (spatial primarily) of input pressure (i. e., winds) field.

A comparison of model ice edge to NPOC ice edge reports was conducted for selected dates. It indicated that the model ice edge tended to be well south (> 100 km) of the actual ice edge through most of the year. Model performance was better in the latter part of the year than in the begining. Use of monthly oceanic heat fluxes with poor spatial resolution results in the loss of some detail in advected heat flux such as the West Spitsbergen Current. The 127 km resolution of the model grid will also result in some loss of detail along the ice edge. The PIPS model overcomes this by being updated by the weekly ice edge reports from NPOC, therfore maintaining a fairly accurate picture of the ice edge. Regional models along the ice edge currently being developed would also provide improved spatial resolution and depiction of the ice edge.
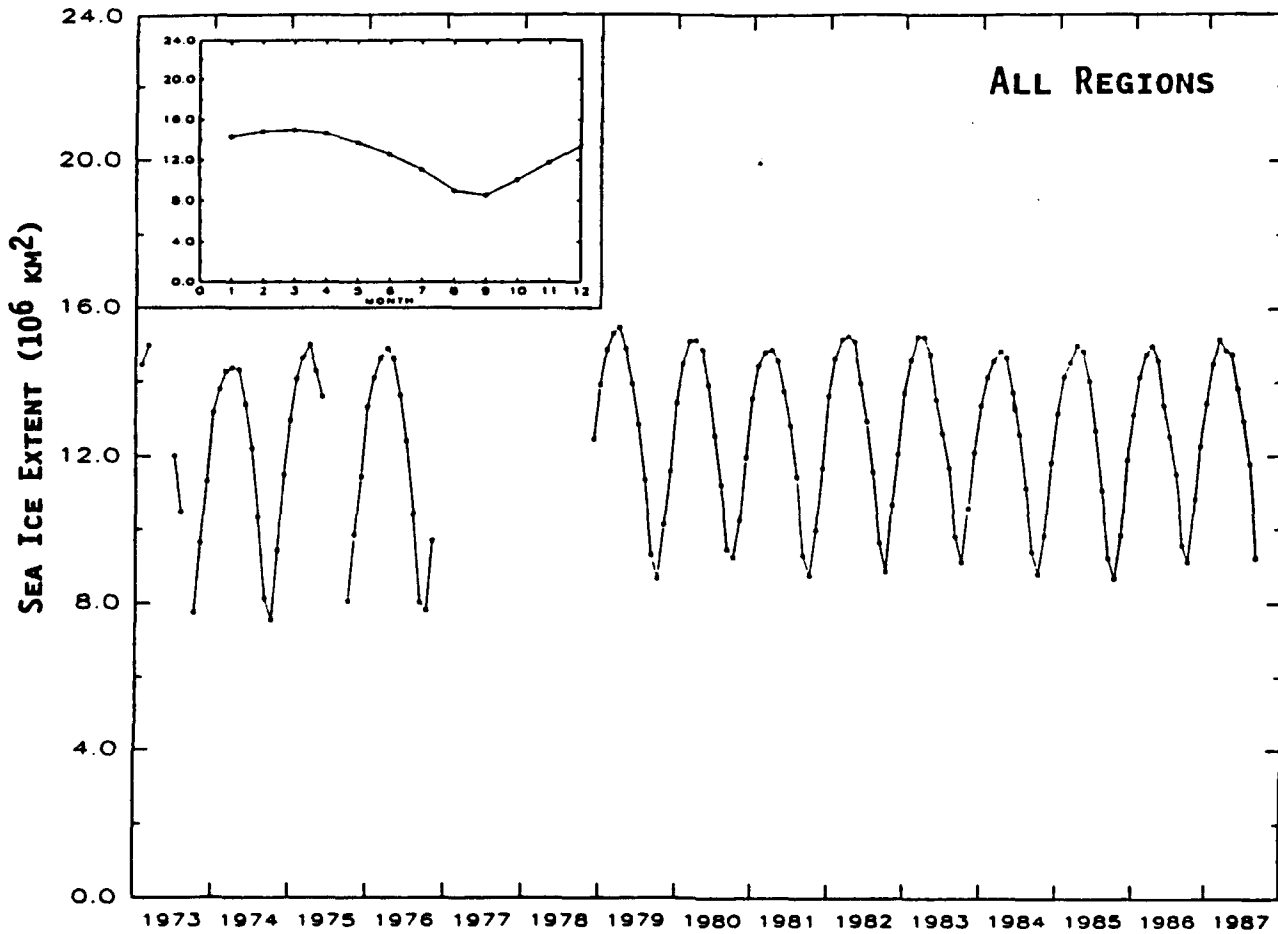
Figure 4.1 A time series of monthly averaged sea ice extents from the available ESMR and SMMR data, 1973-1987, for the entire Arctic polar region. The inset shows the average seasonal cycle over the years 1973-1976 and 1979-1986 (Parkinson and Cavalieri, 1979).
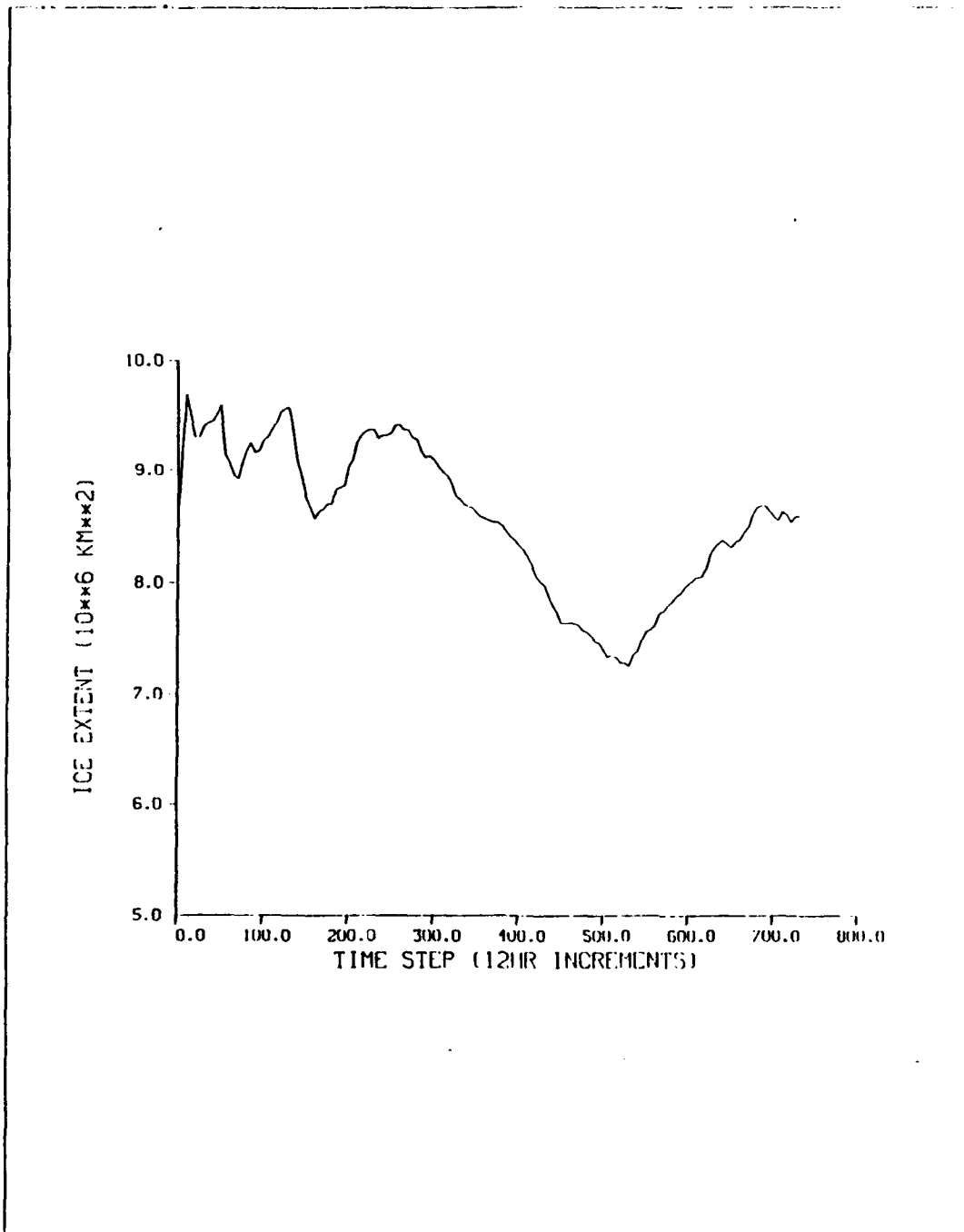
Figure 4.2 Model sea ice ext   for the year 1986. Ice extent is any defined area that contains 15 percent or more ice. The x-axis is in time steps of 12 hours for one year, and the y-axis is the ice extent in $10^6 km^2$.
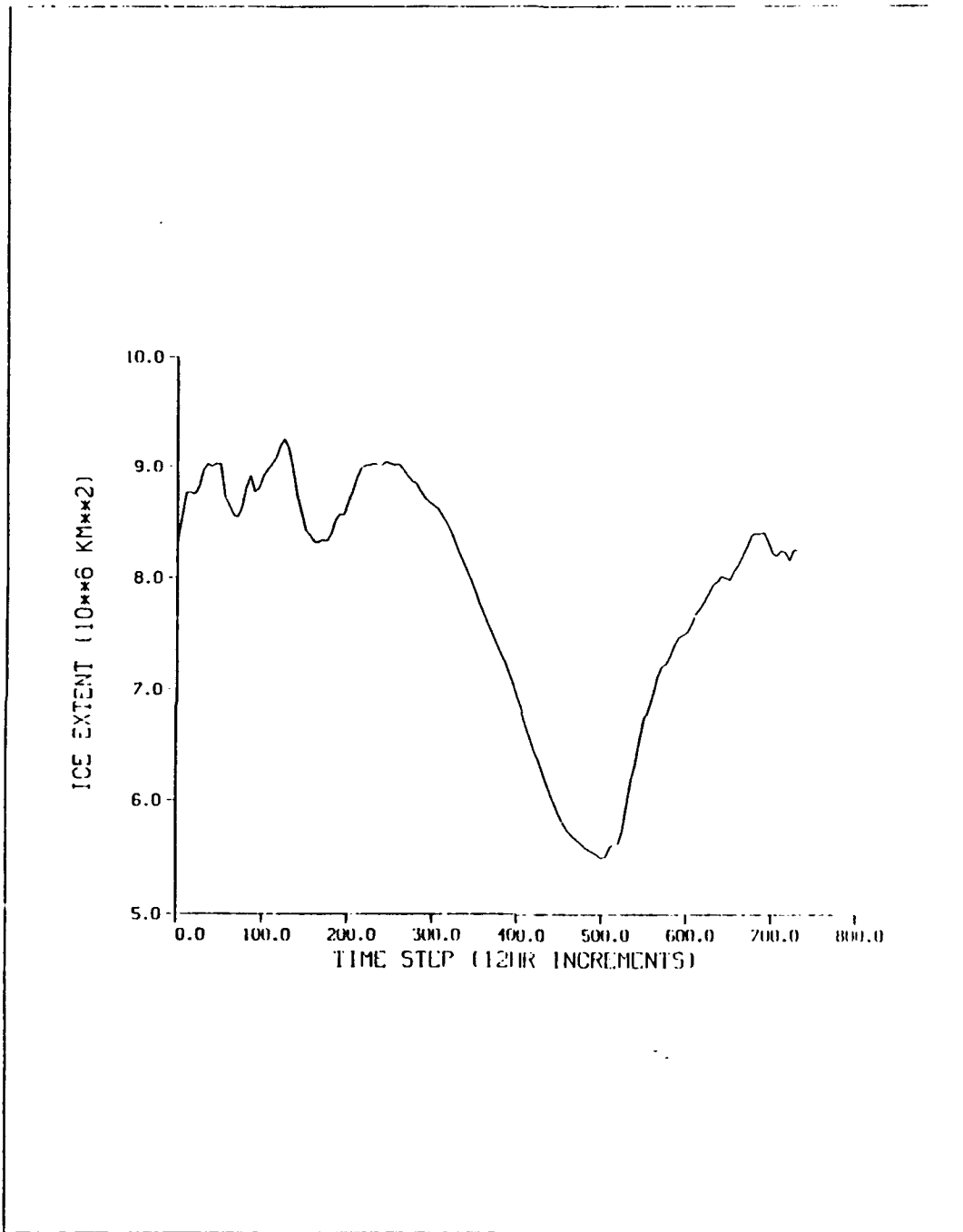
Figure 4.3 Model sea ice area for the year 1986. Ice area covers only the actual ice present within each cell. The x-axis is in time steps of 12 hours over a year, and the y-axis is the ice areal extent in $10^6 km^2$.
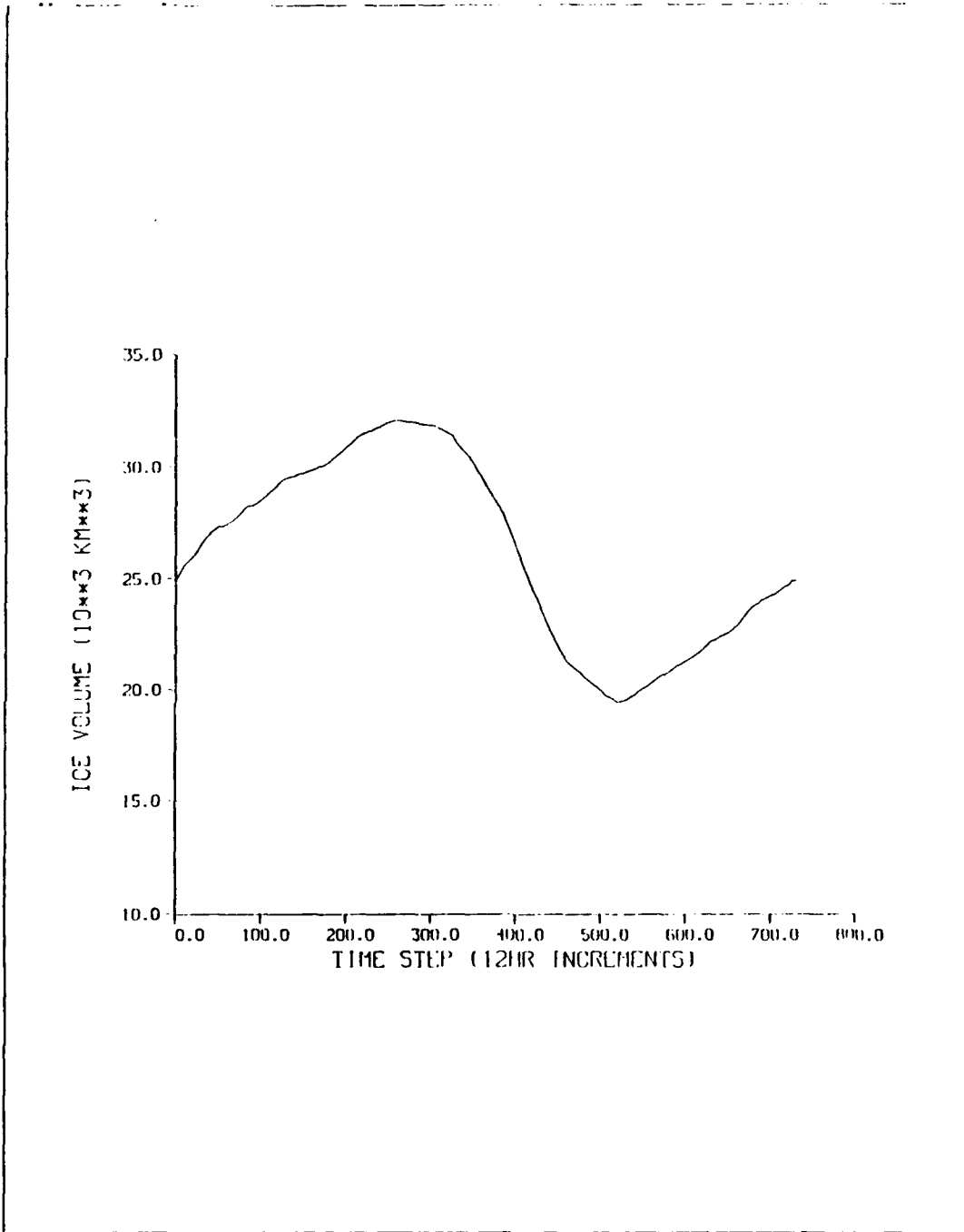
Figure 4.4 Model sea ice volume for the year 1986. Ice volume is the product of the ice thickness and the ice concentration. The x-axis is in time steps of 12 hours for one year. The y-axis is ice volume in $10^3 km^3$.
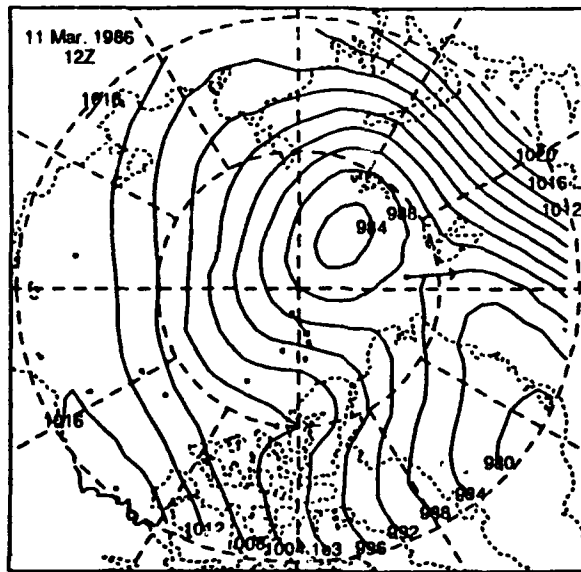
Figure 4.5 Buoy trajectories and buoy derived surface pressure for 11 March 1986. For estimation of buoy speed 1 cm equals 23.1 cm/s.
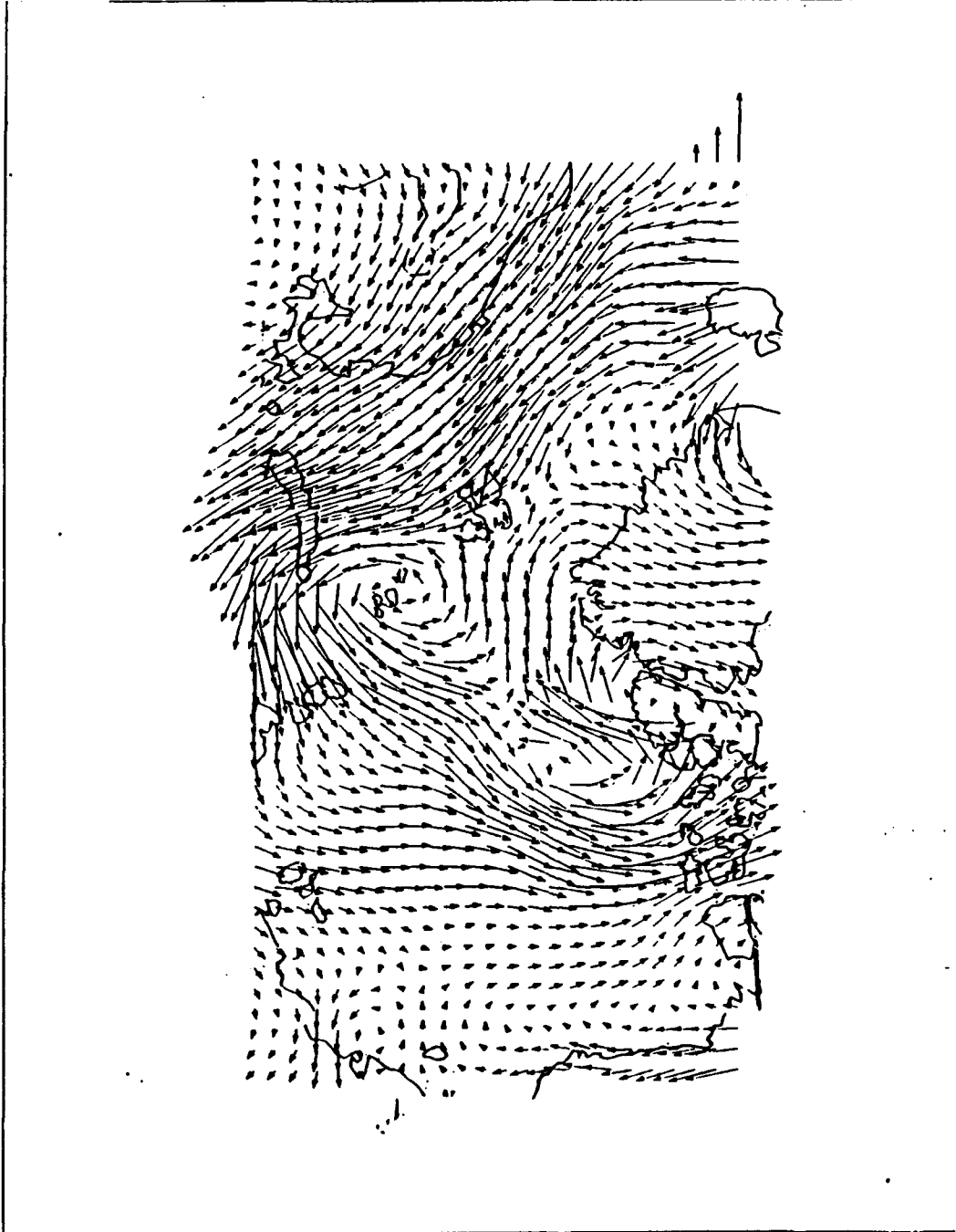
Figure 4.6 NOGAPS derived wind trajectories in m/s for 11 March 1986 The three vectors in the lower right corner represent speeds of 5, 10, and 20 m/s, respectively.

Figure 4.7 Model ice drift trajectories in cm/s for 11 March 1986. The three vectors toward the bottom center represent speeds of 5, 10 and 20 cm/s, respectively.
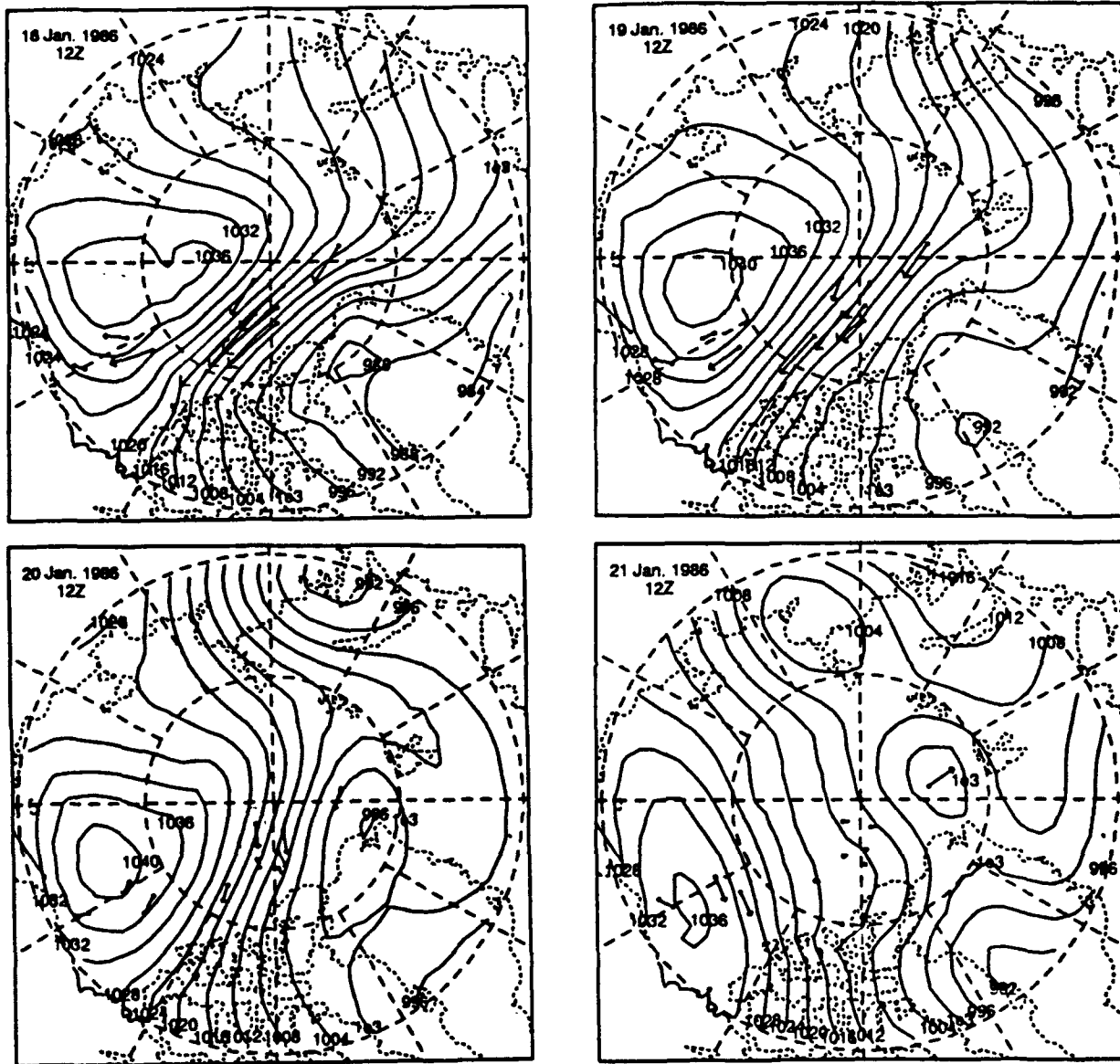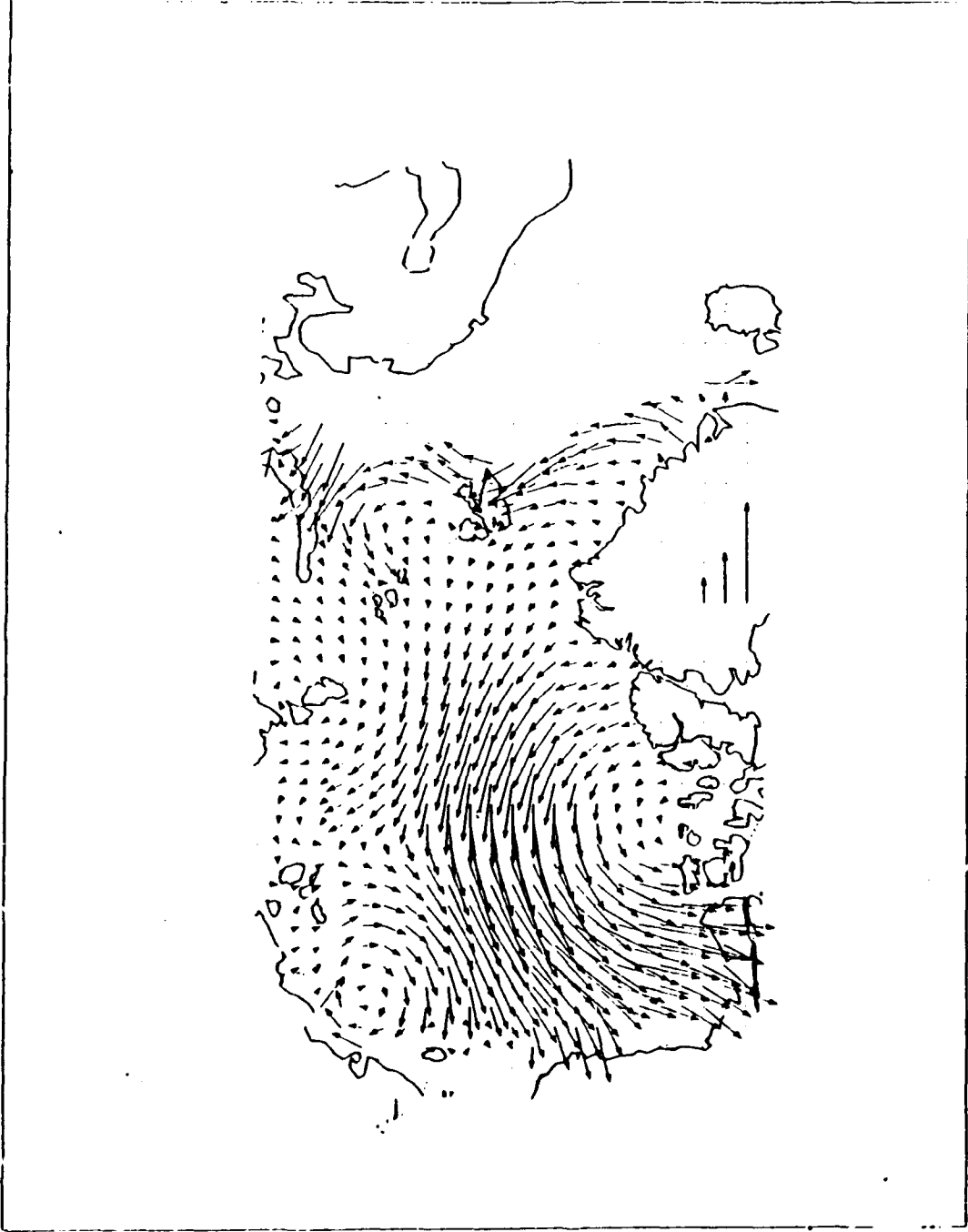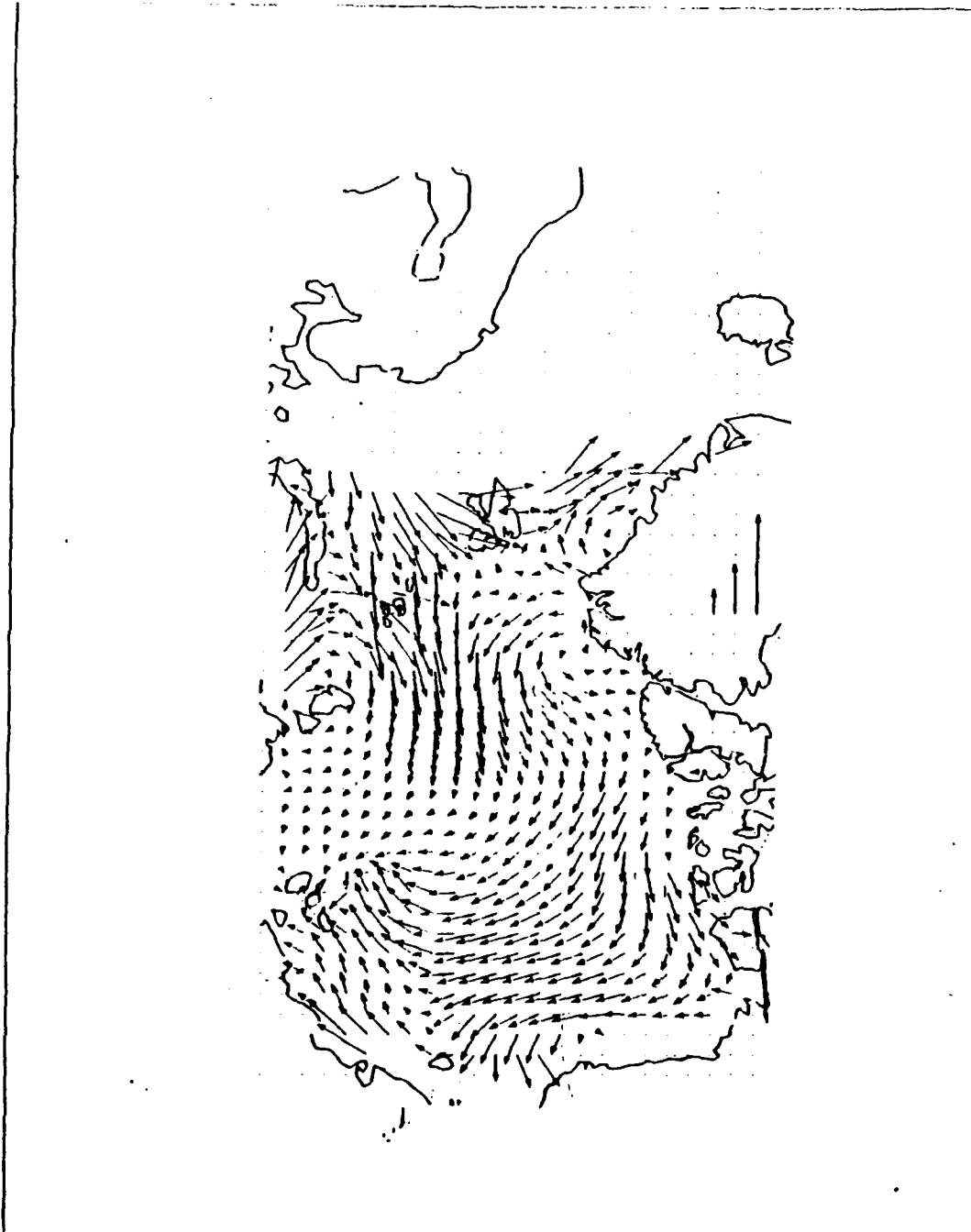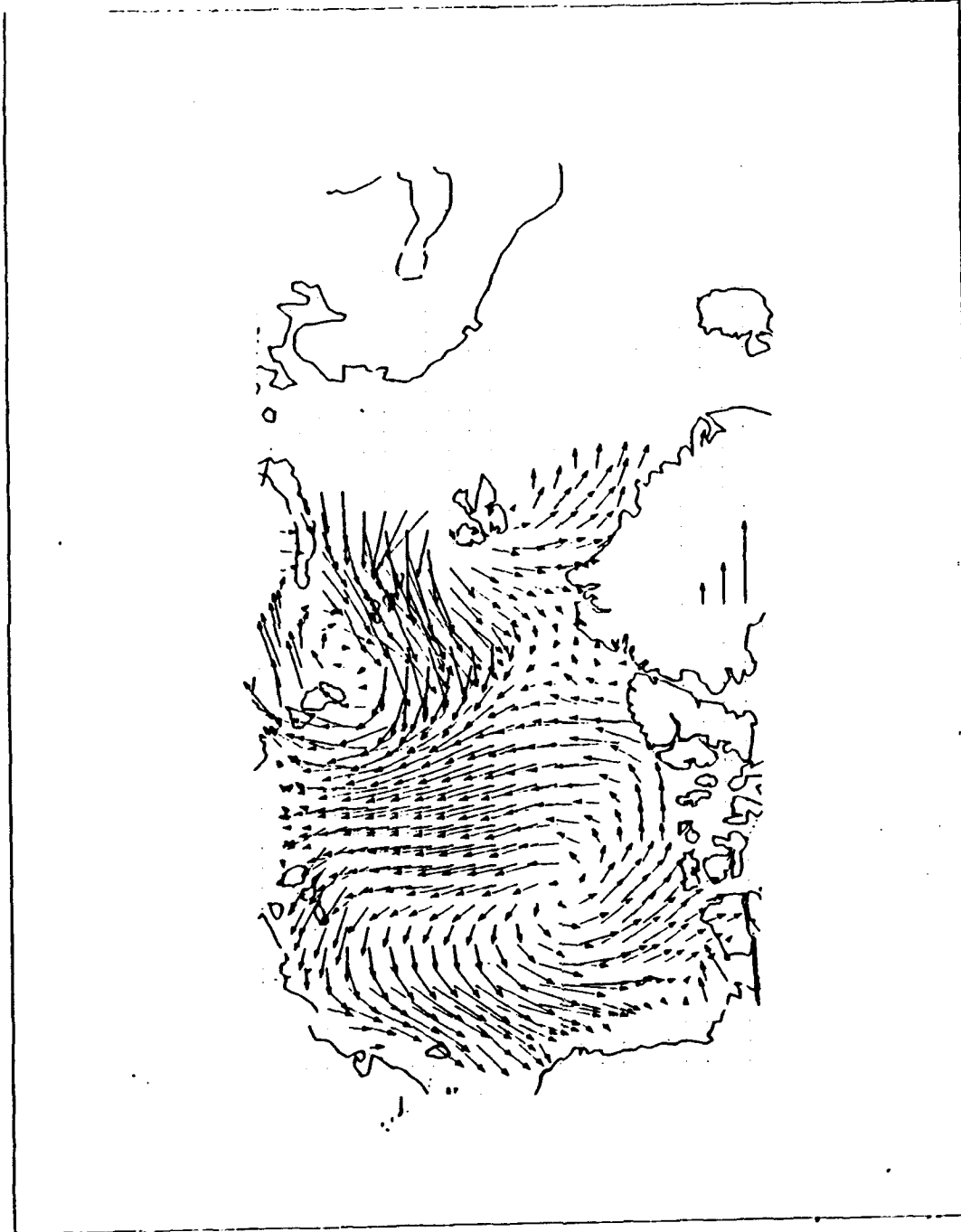
Figure 4.8 Buoy trajectories and buoy derived surface pressure for (a) 18 January, (b) 19 January, (c) 20 January, and (d) 21 January 1986. For estimation of buoy speed 1 cm equals 23.1 cm/s.
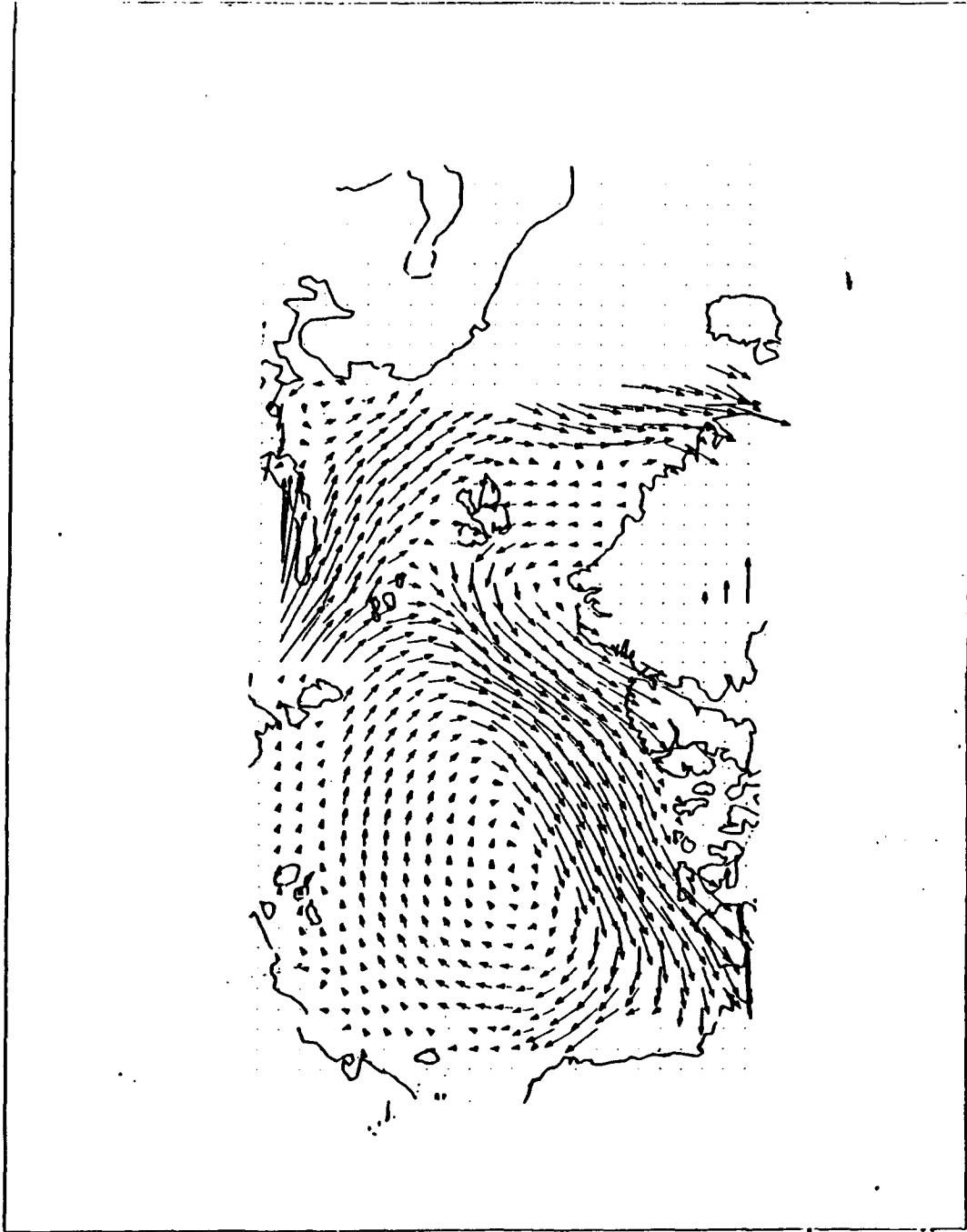
Figure 4.9 Model ice drift trajectories in cm/s for 20 January 1986. The three vectors toward the bottom center represent speeds of 5, 10 and 20 cm/s, respectively.
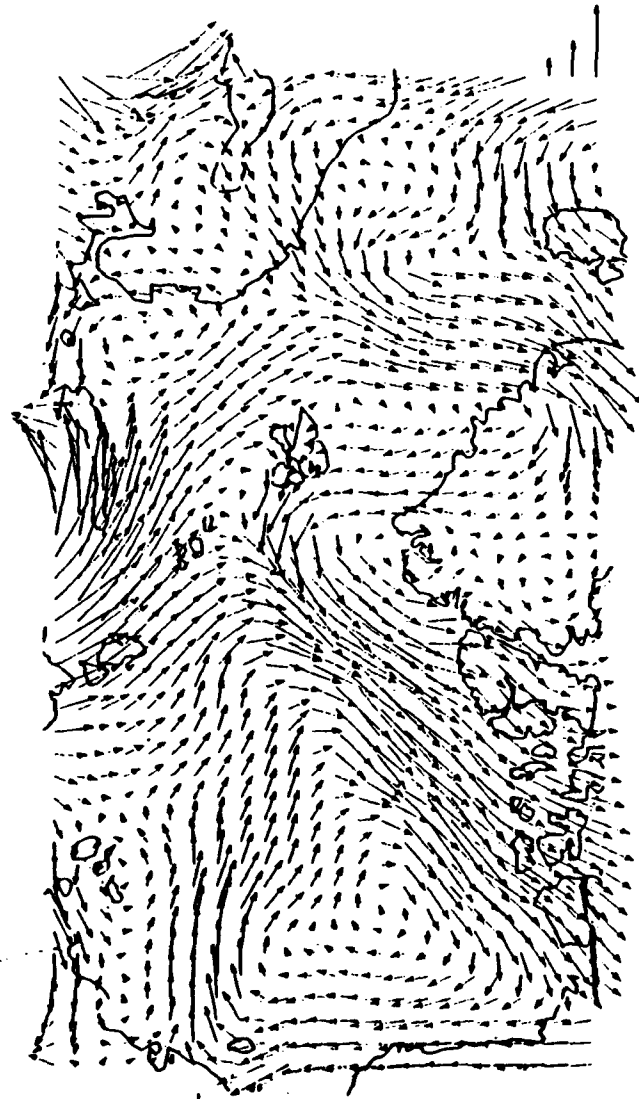
Figure 4.10 NOGAPS derived wind trajectories in m/s for 20 January 1986. The three vectors in the lower right corner represent speeds of 5, 10, and 20 m/s, respectively.
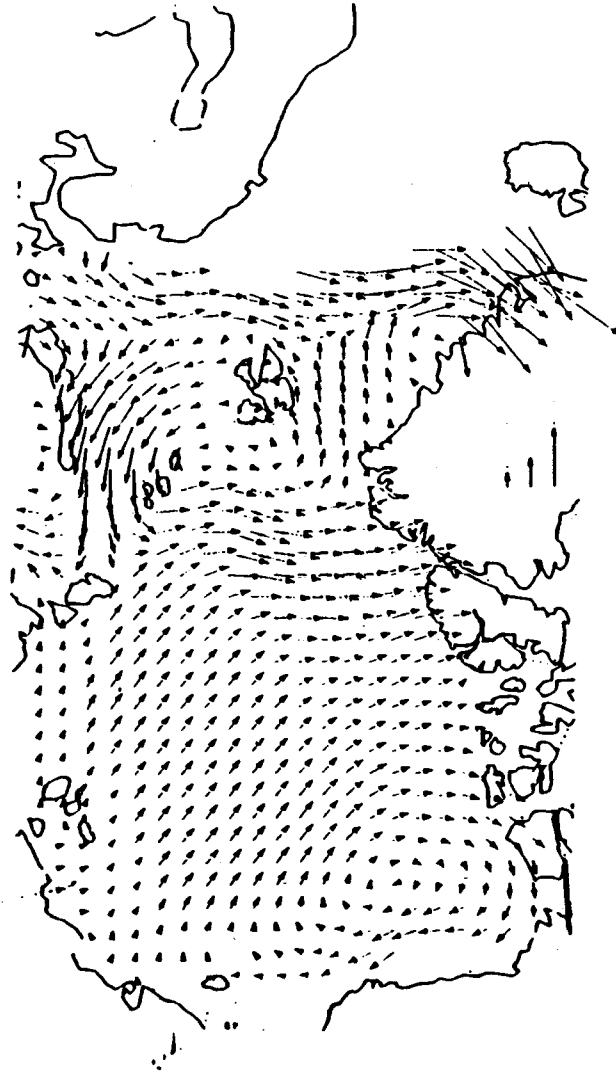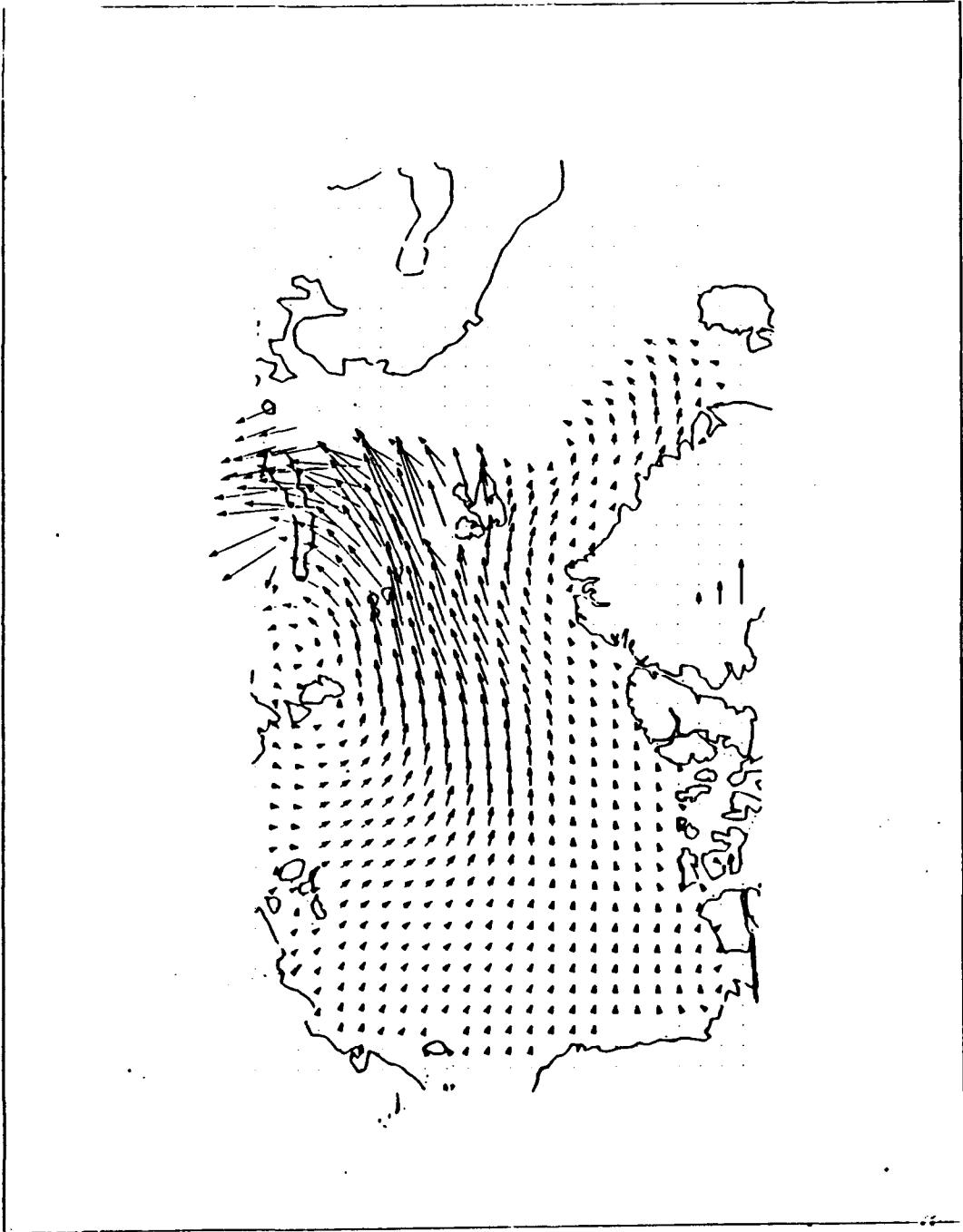
Figure 4.11 Model ice drift trajectories in cm/s for 21 January 1986. The three vectors toward the bottom center represent speeds of 5, 10, and 20 cm/s, respectively.
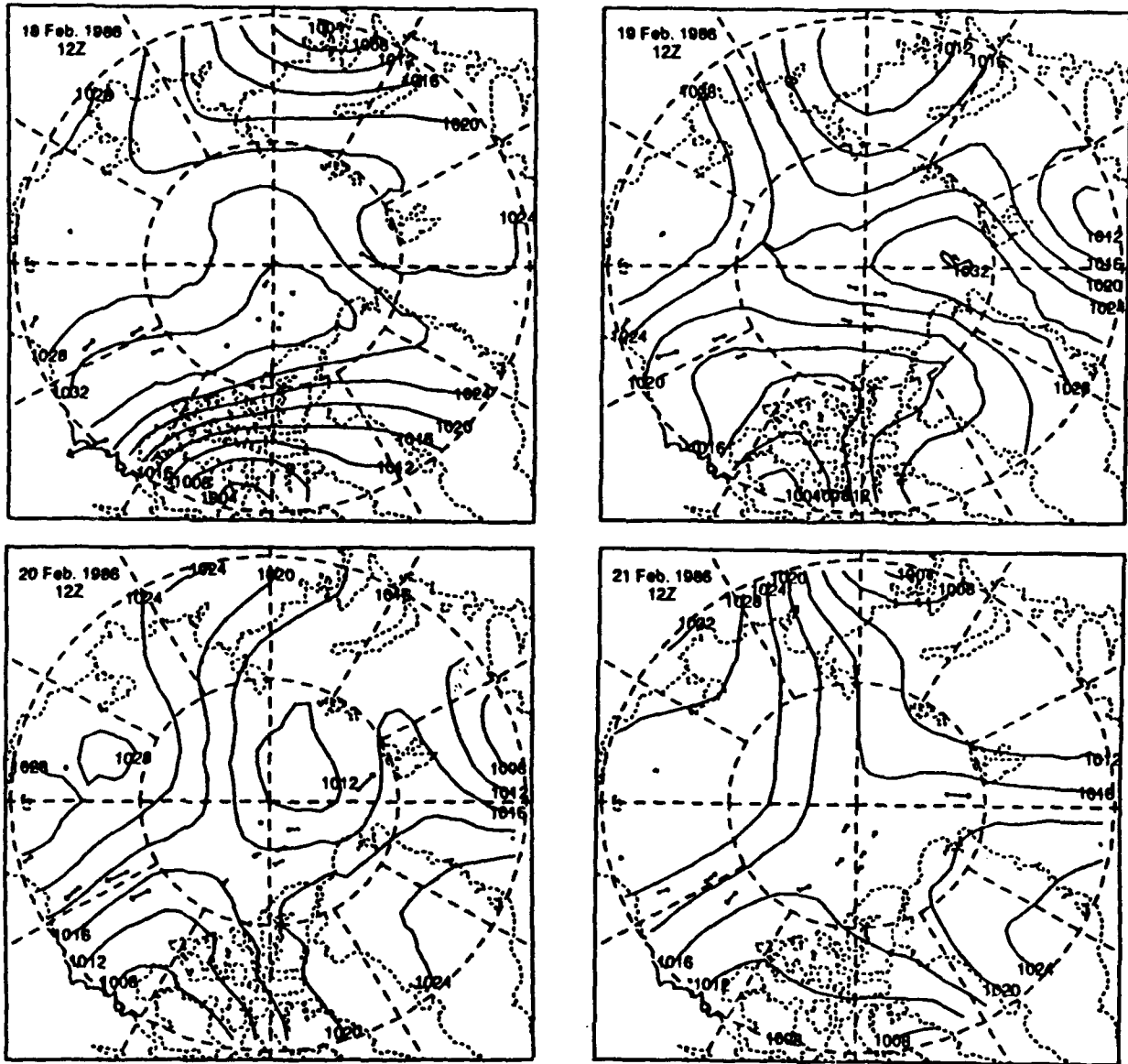
Figure 4.12 Buoy trajectories and buoy derived surface pressure for (a) 18 February, (b) 19 February, (c) 20 February, and (d) 21 February 1986. For estimation of buoy speed 1 cm equals 23.1 cm/s.
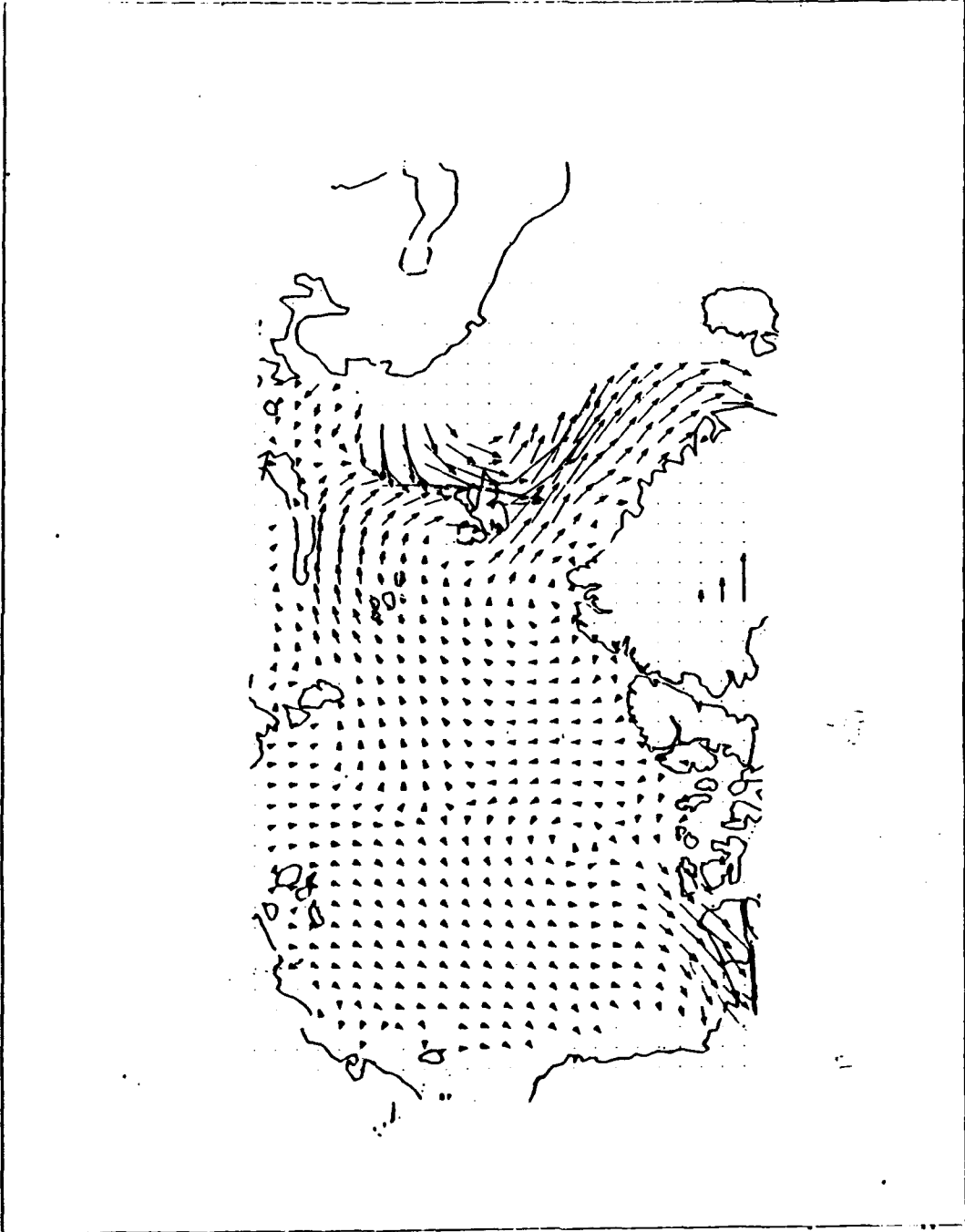
Figure 4.13 Model ice drift trajectories in cm/s for 19 February 1986. The three vectors toward the bottom center represent speeds of 5, 10 and 20 cm/s, respectively.
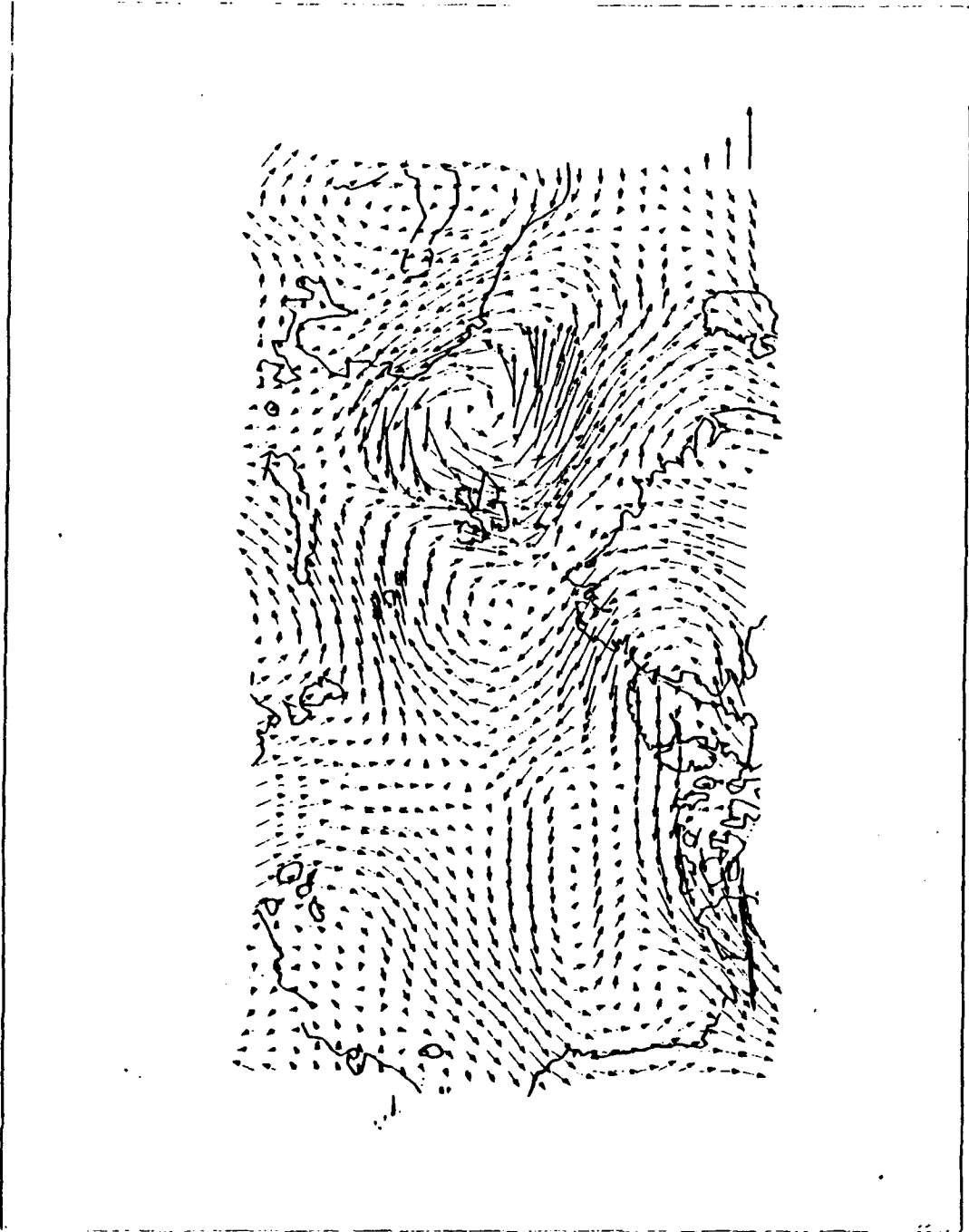
Figure 4.14 NOGAPS derived wind trajectories in m/s for 19 February 1986. The three vectors in the lower right corner represent speeds of 5, 10, and 20 m/s, respectively.
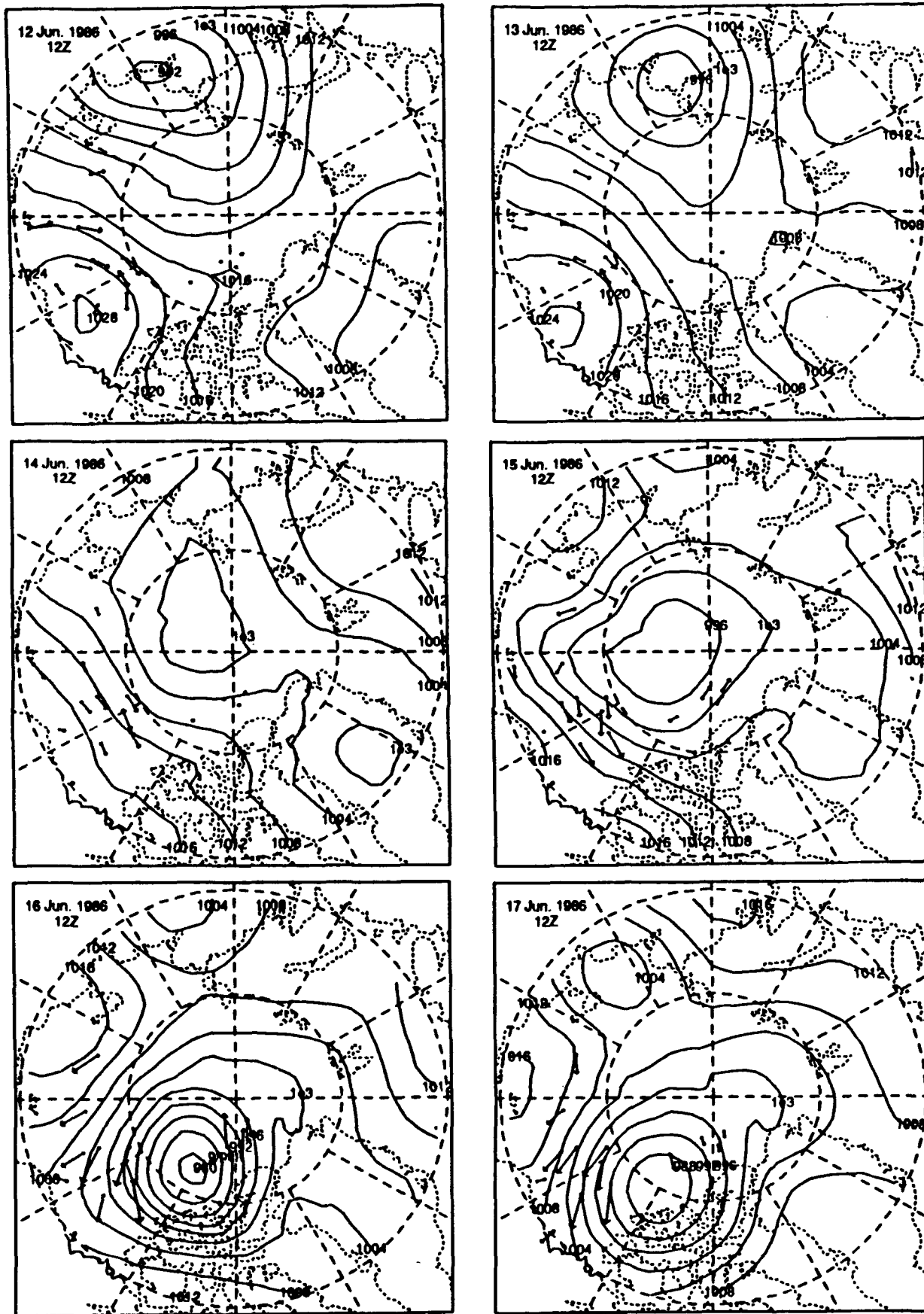
Figure 4.15 Buoy trajectories and buoy derived surface pressure for (a) 12 June, (b) 13 June, (c) 14 June, (d) 15 June, (e) 16 June, (f) June 1986. For estimation of buoy speed 1 cm equals 23.1 cm/s.
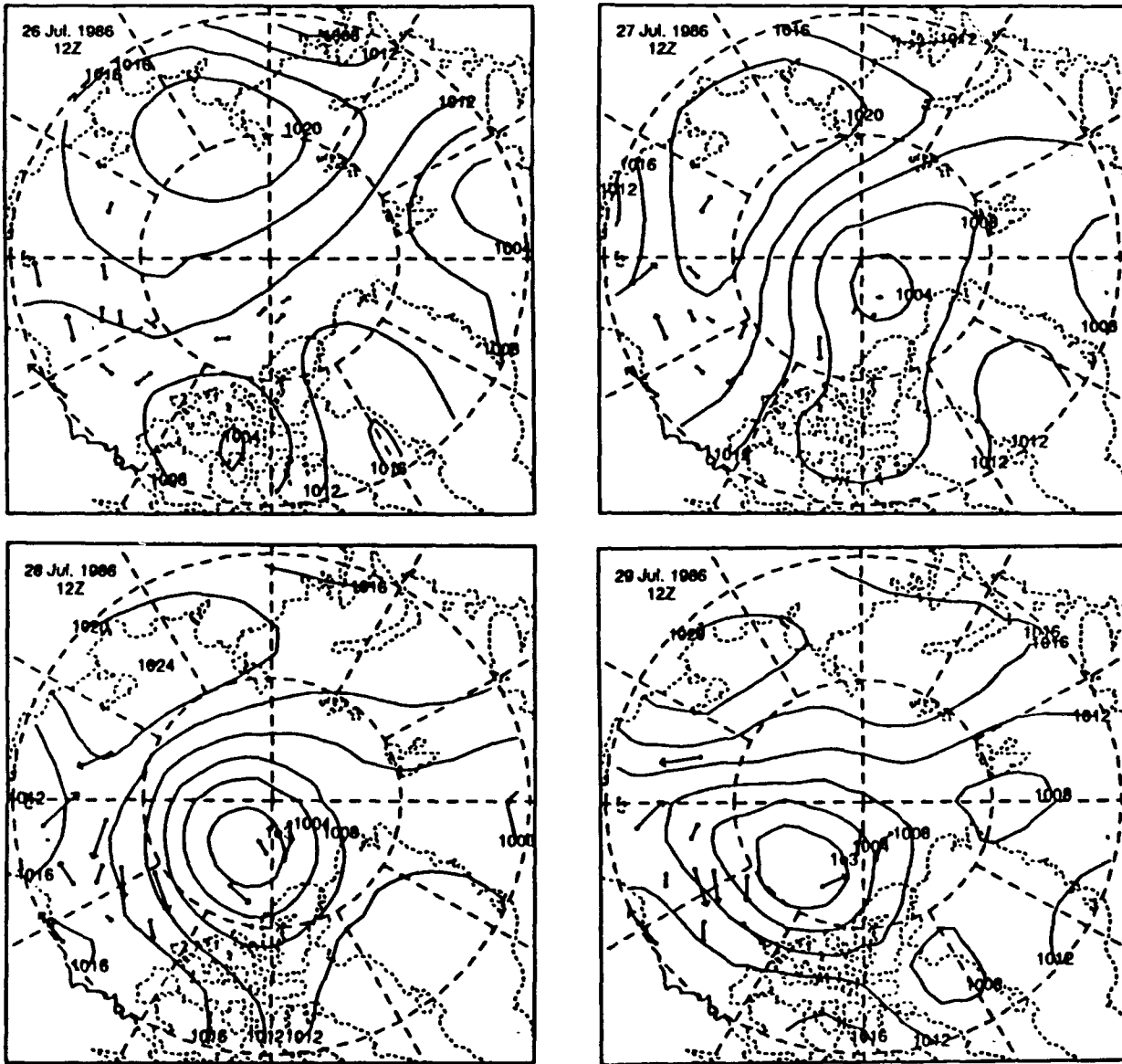
Figure 4.16 Buoy trajectories and buoy derived surface pressure for (a) 26 July, (b) 27 July, (c) 28 July, and (d) 29 July 1986. For estimation of buoy speed 1 cm equals 23.1 cm/s.

70
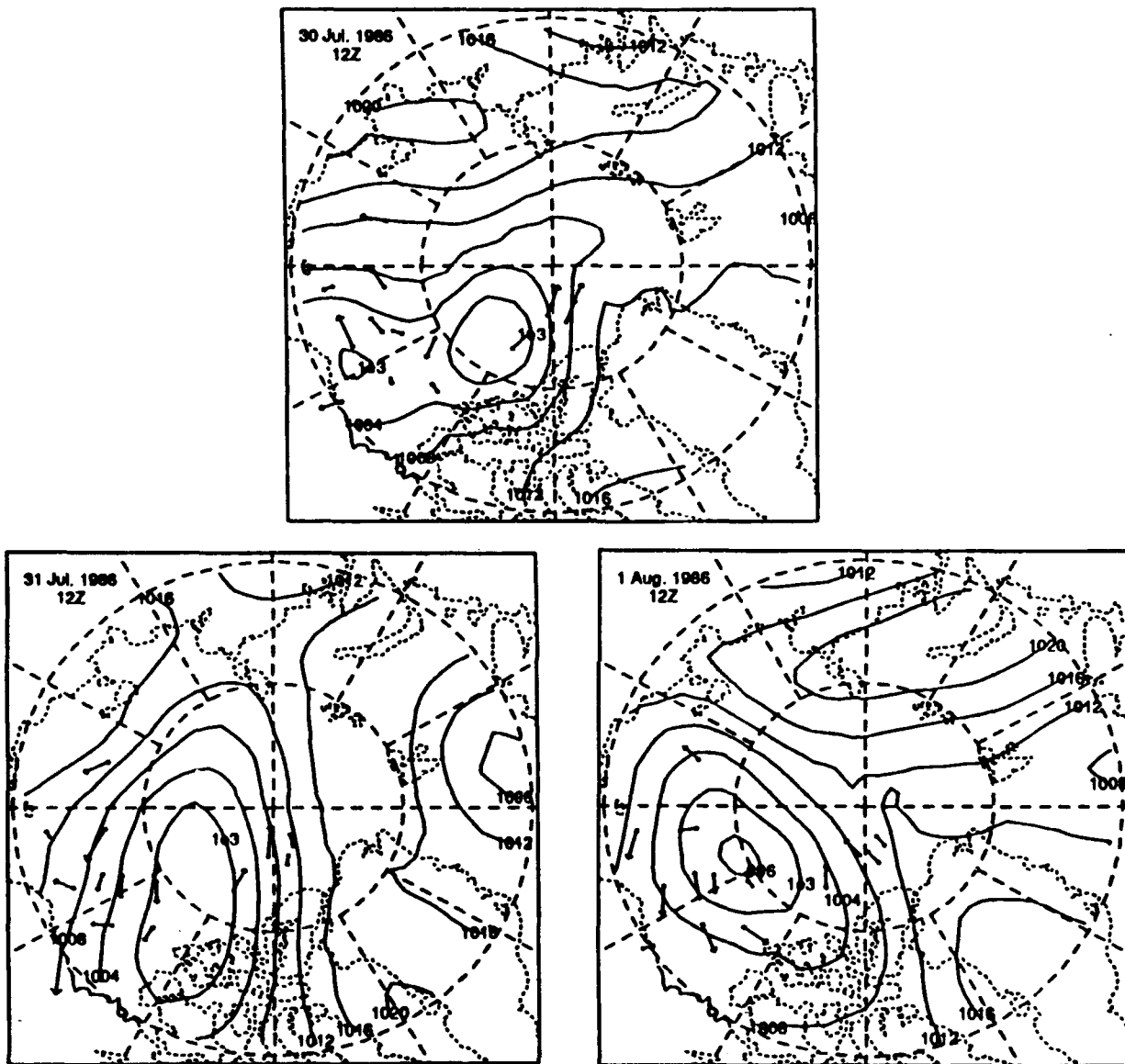
Figure 4.16 Buoy trajectories and buoy derived surface pressure for (c) 30 July, (f) 31 July, and (I) August 1986. For estimation of buoy speed 1 cm equals 23.1 cm/s.
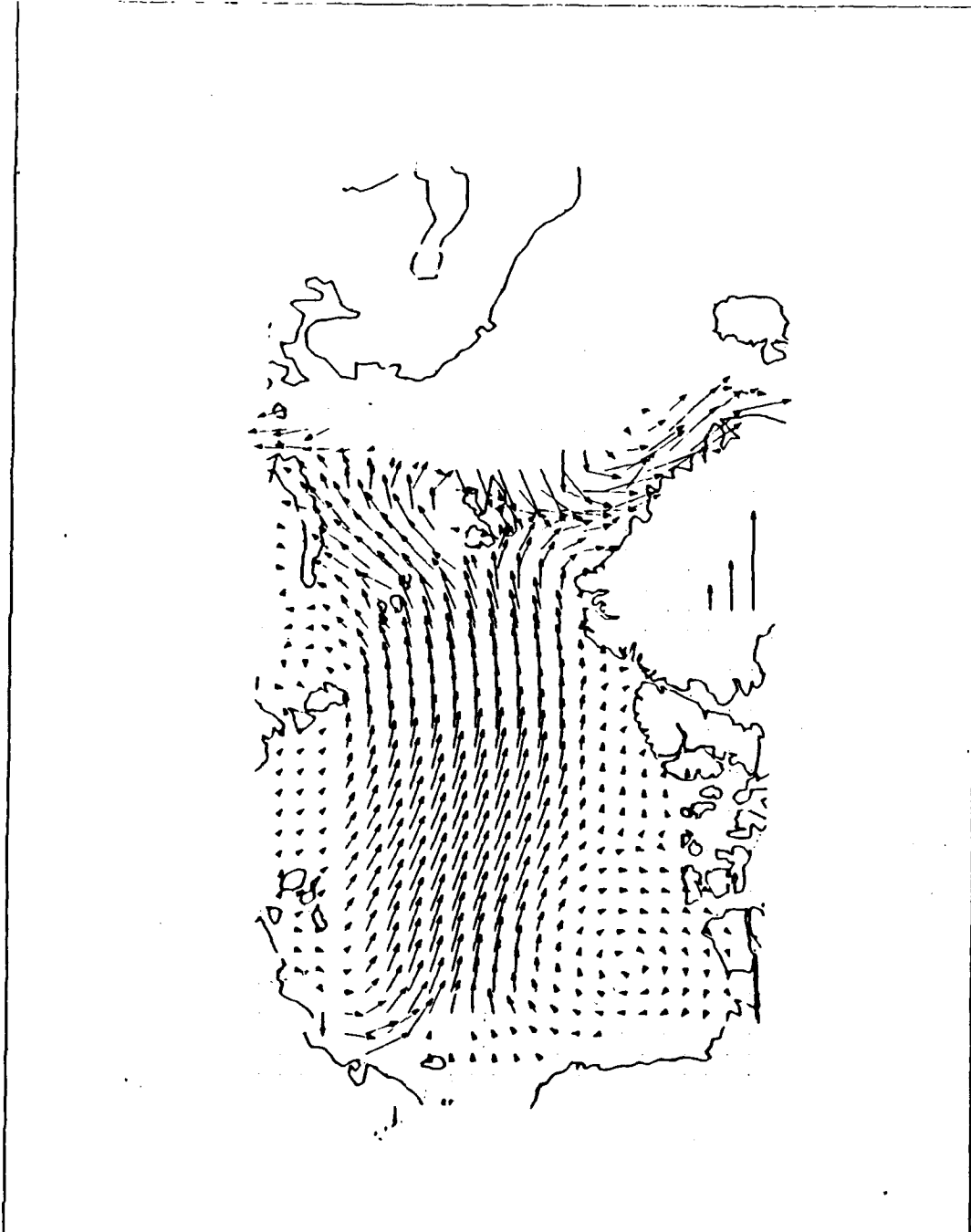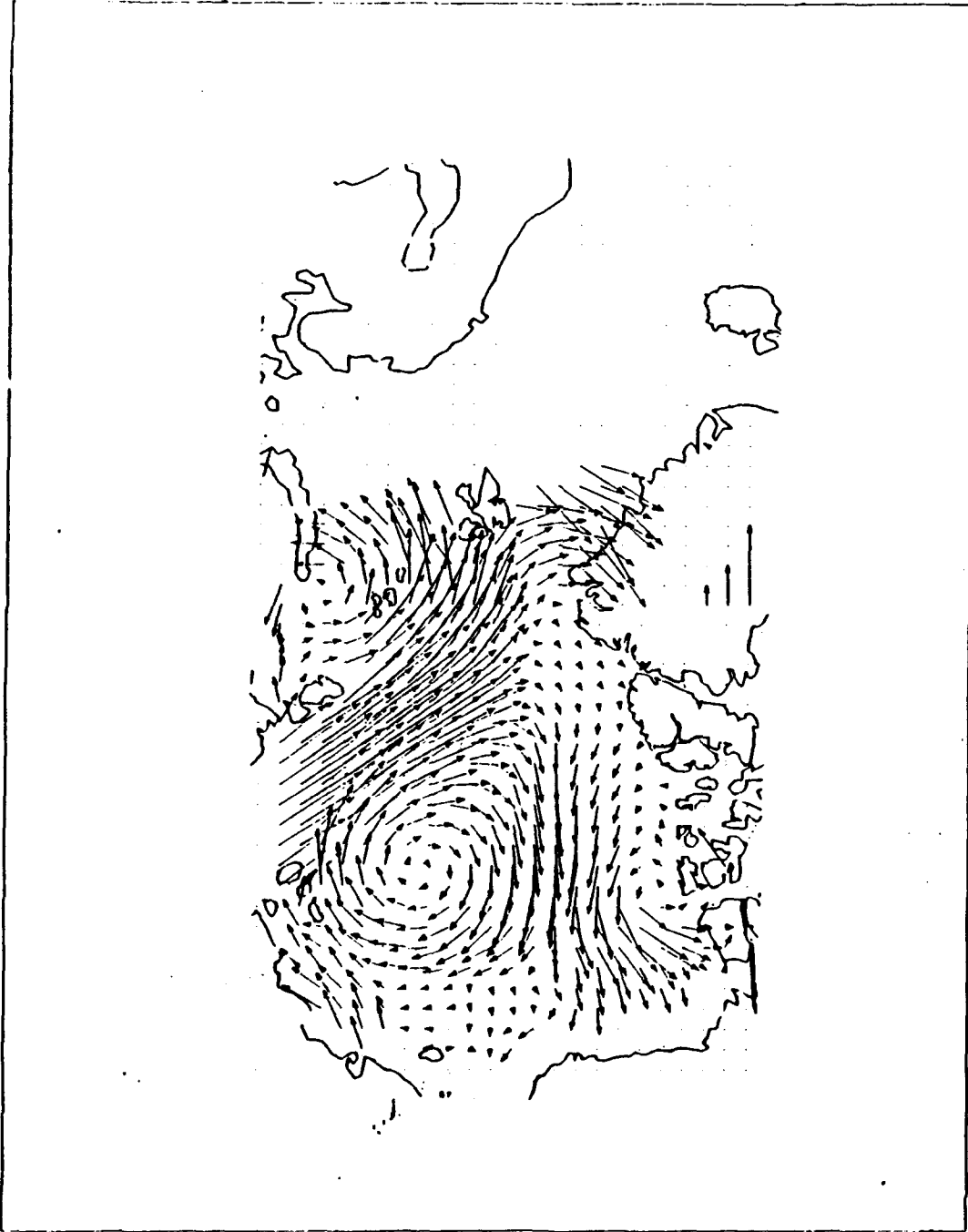
Figure 4.17 Model ice drift trajectories in cm/s for 12 June 1986. The three vectors toward the bottom center represent speeds of 5, 10 and 20 cm/s, respectively.

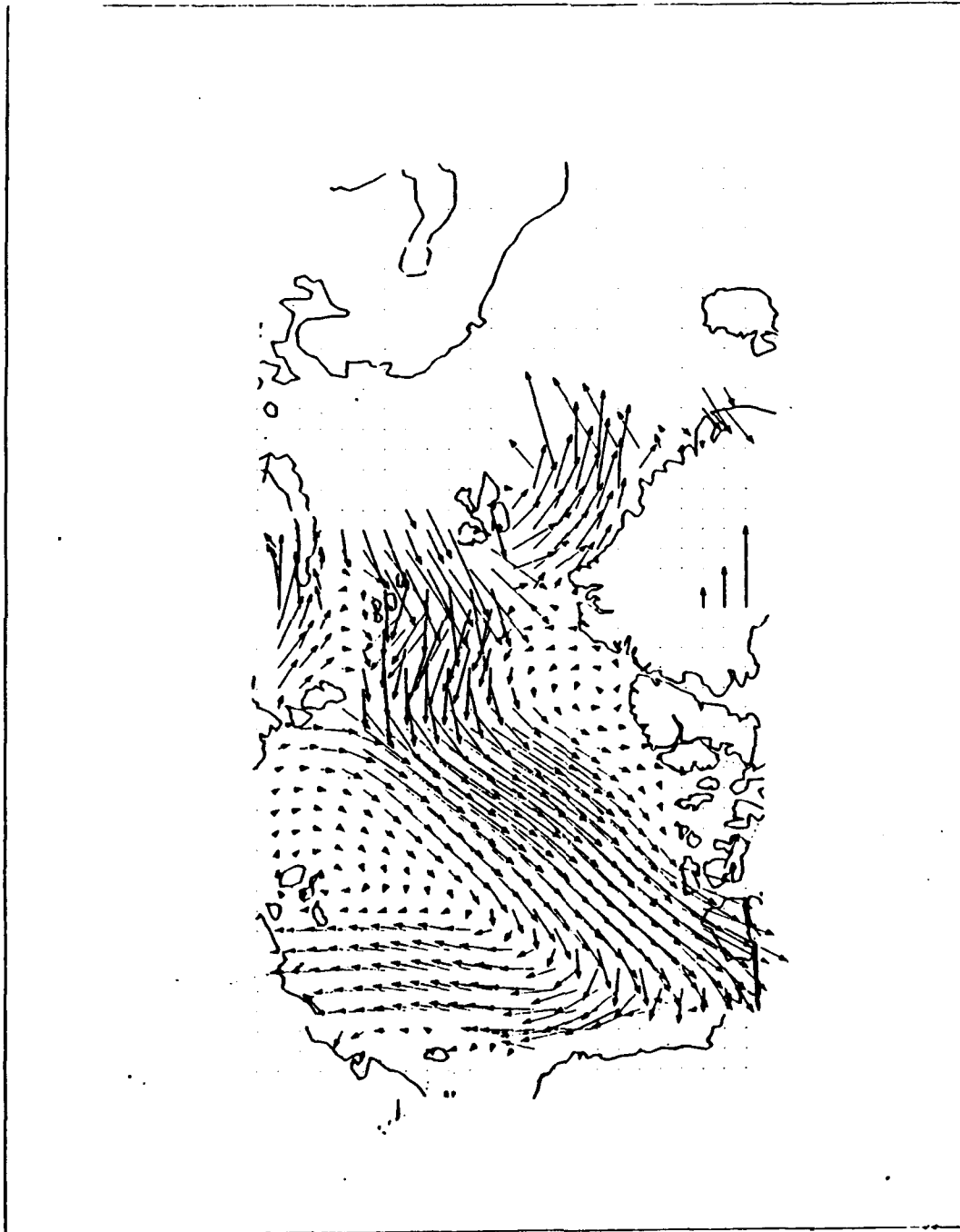Figure 4.18 Model ice drift trajectories in cm/s for 17 June 1986. The three vectors toward the bottom center represent speeds of 5, 10 and 20 cm/s, respectively.

Figure 4.19 Model ice drift trajectories in cm/s for 26 July 1986. The three vectors toward the bottom center represent speeds of 5, 10 and 20 cm/s, respectively.

Figure 4.20 Model ice drift trajectories in cm/s for 1 August 1986. The three vectors toward the bottom center represent speeds of 5, 10 and 20 cm/s, respectively.
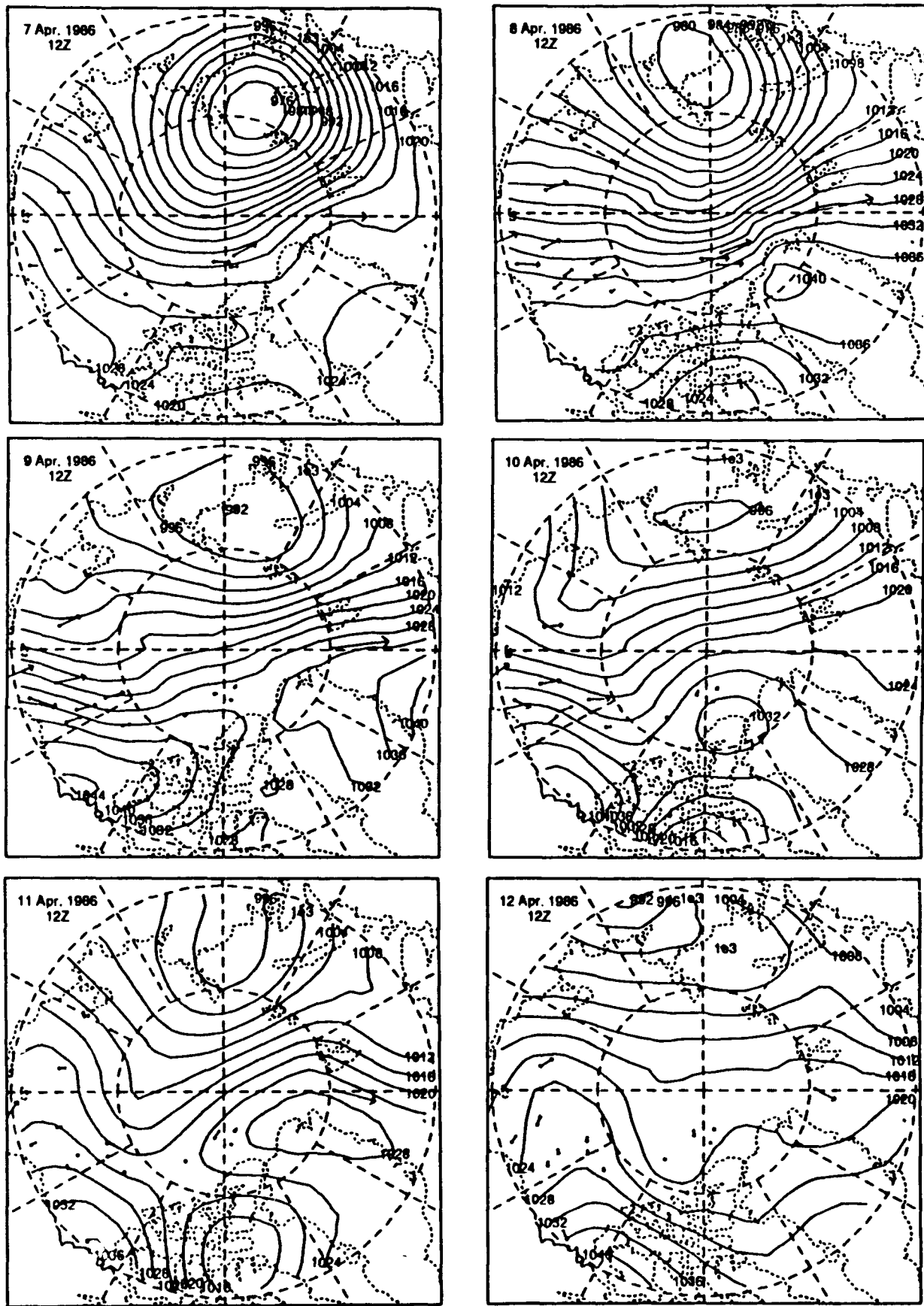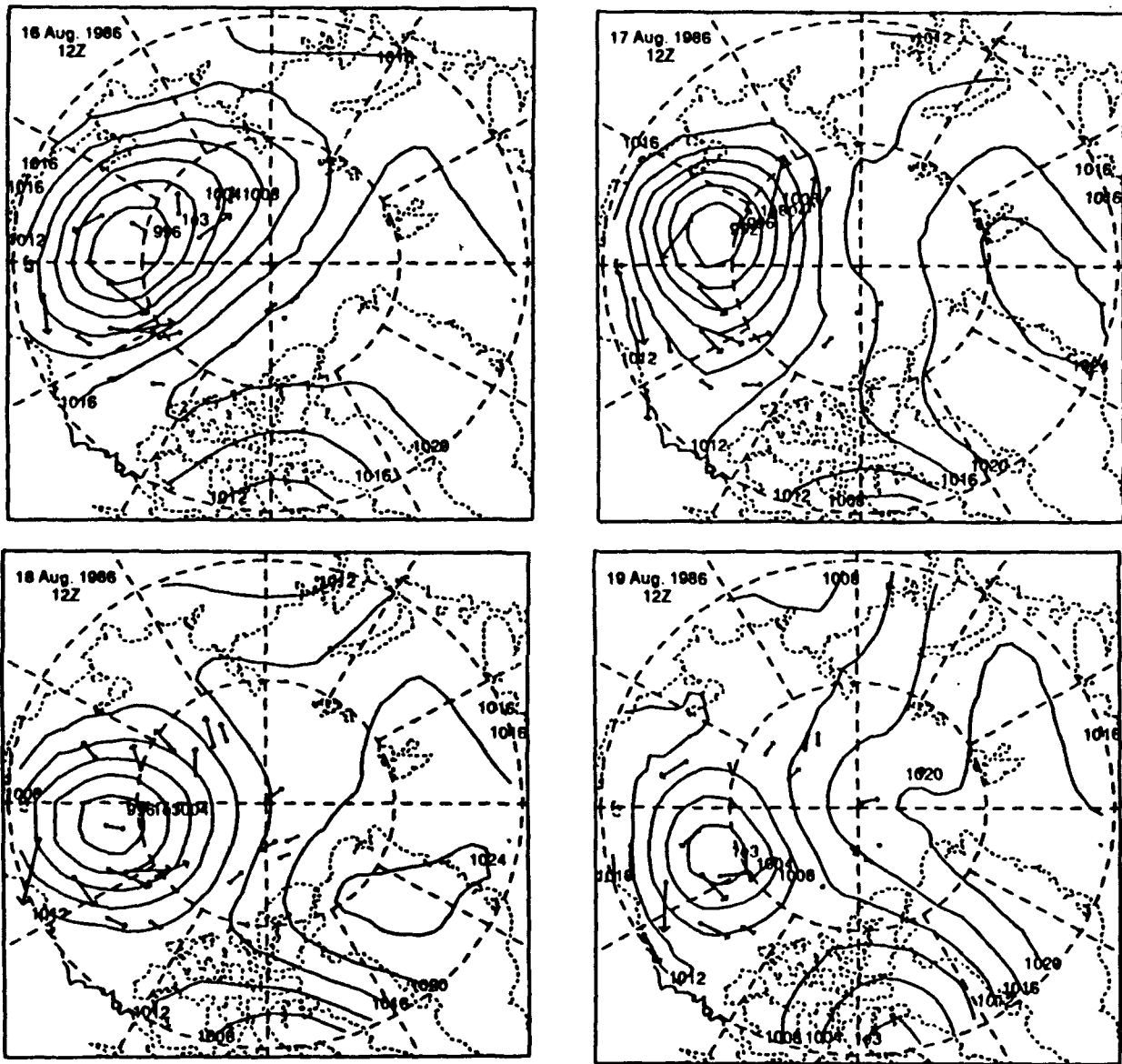
Figure 4.21 Buoy trajectories and buoy derived surface pressure for (a) 7 April, (b) 8 April, (c) 9 April, (d) 10 April, (e) 11 April, and (f) 12 April 1986. For estimation of buoy speed 1 cm equals 23.1 cm/s.
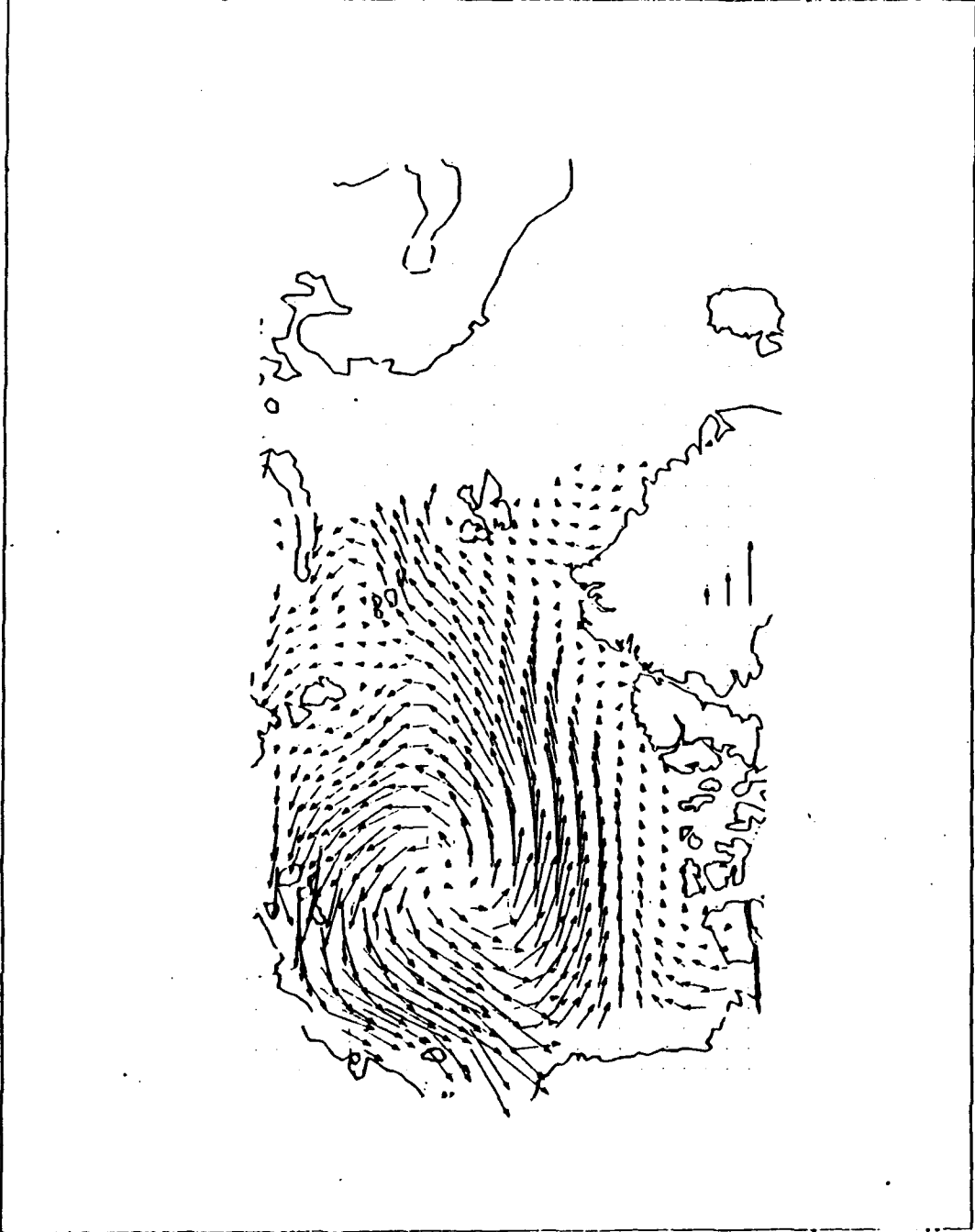
76

Figure 4.22 Model ice drift trajectories in cm/s for 7 April 1986. The three vectors toward the bottom center represent speeds of 5, 10 and 20 cm/s, respectively.
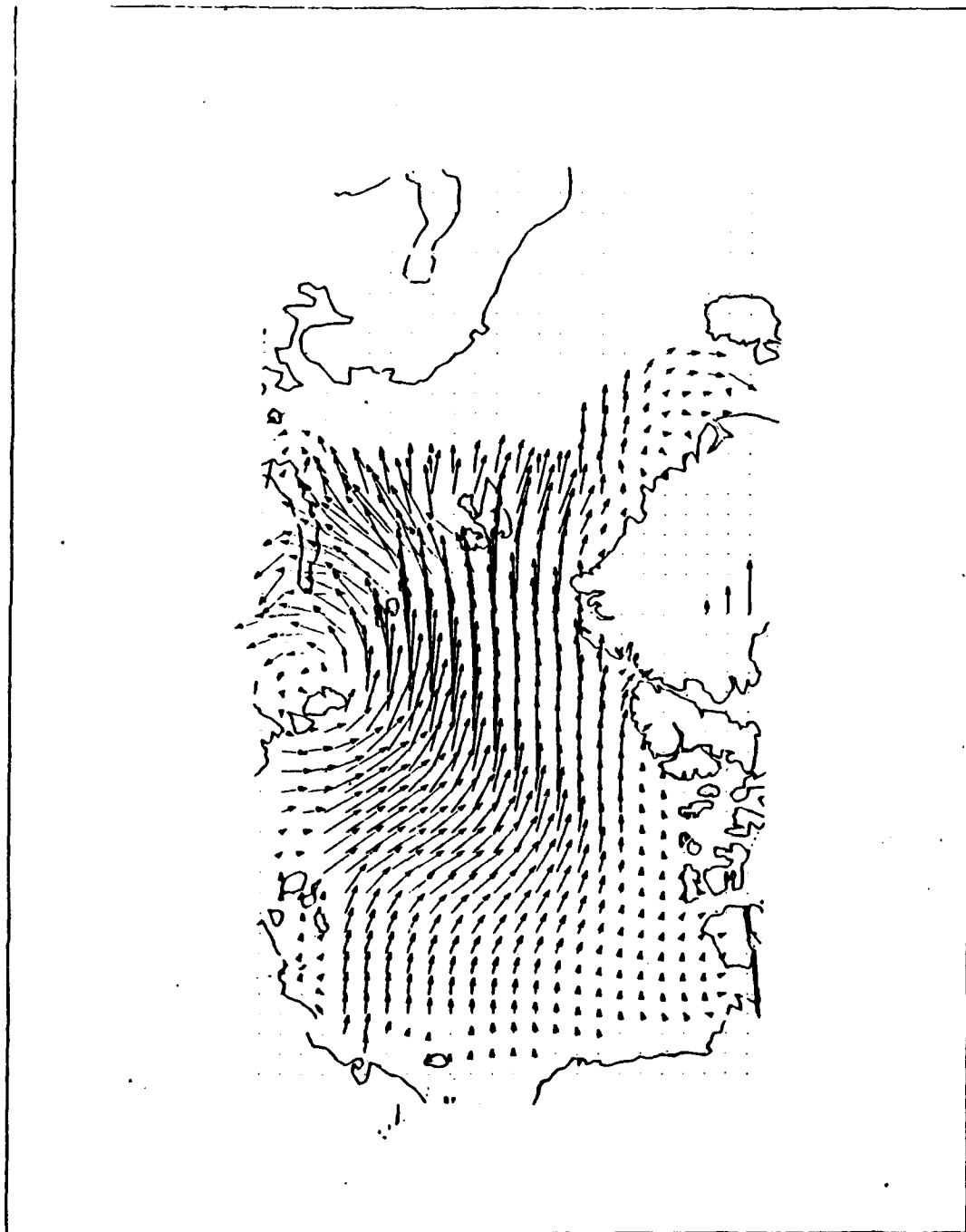
Figure 4.23 Model ice drift trajectories in cm/s for 8 April 1986. The three vectors toward the bottom center represent speeds of 5, 10 and 20 cm/s, respectively.
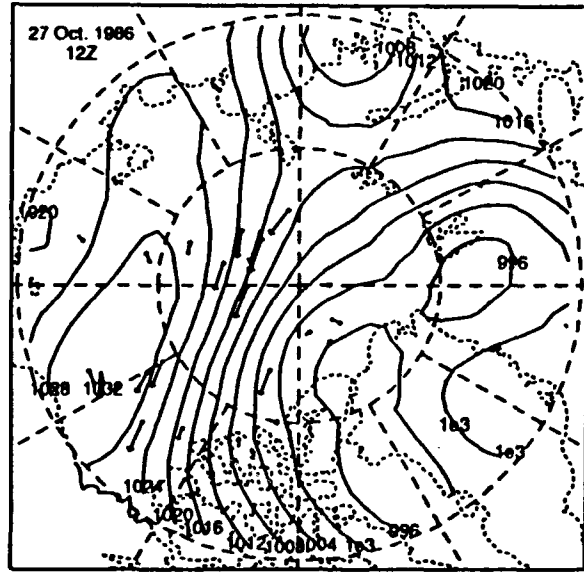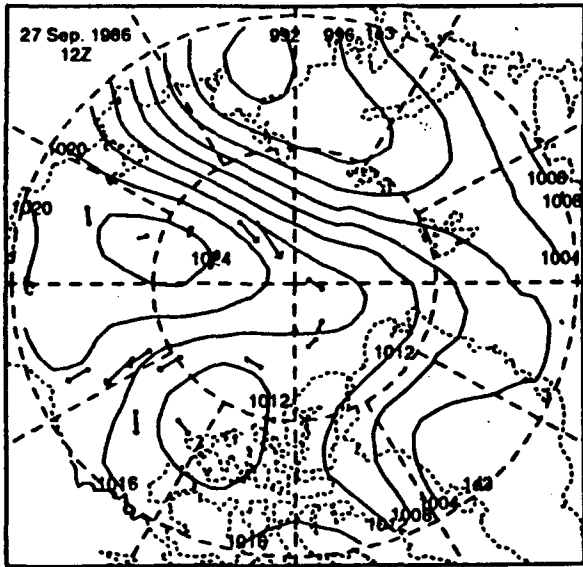
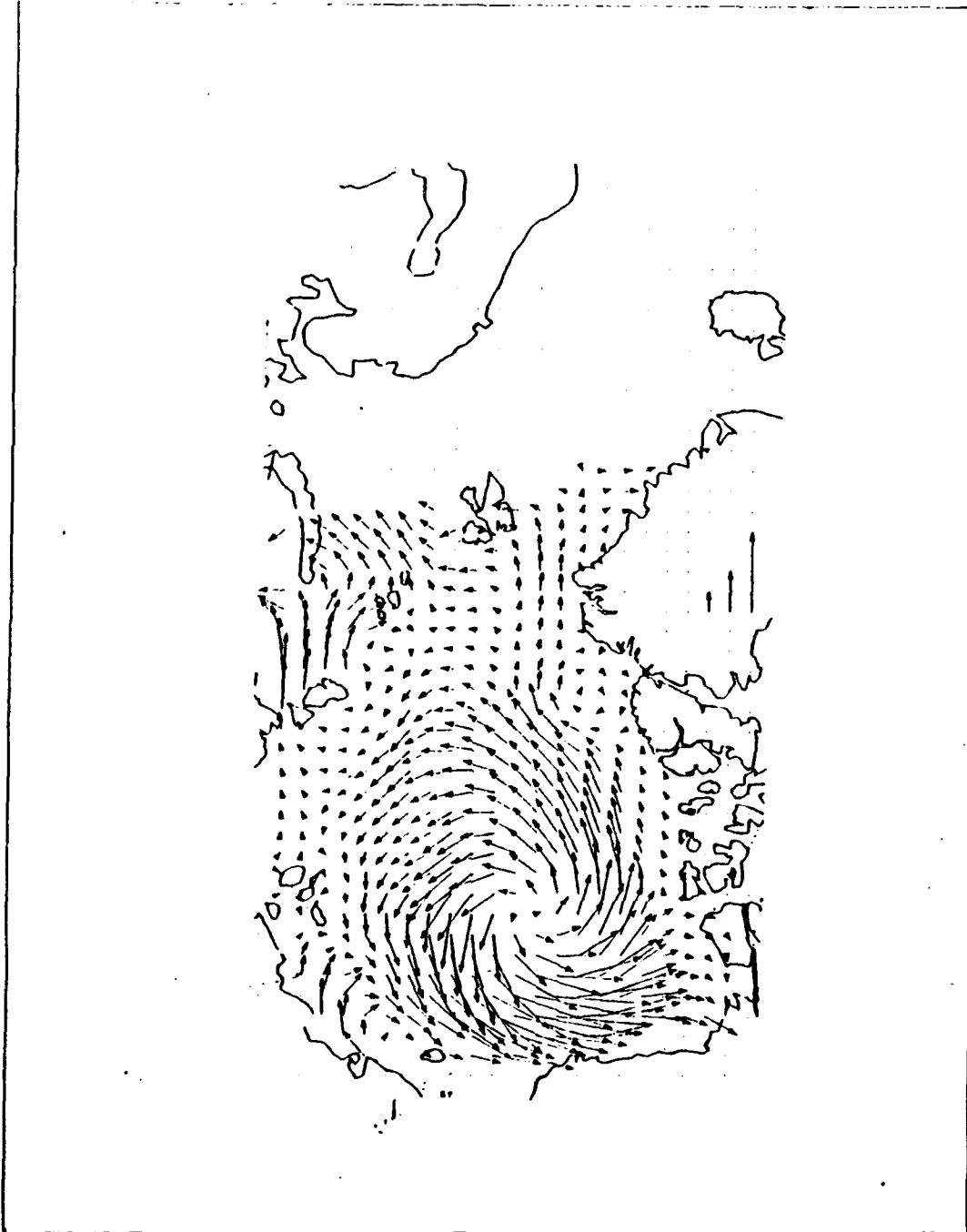Figure 4.24 Buoy trajectories and buoy derived surface pressure for (a) 27 September, and (b) 27 October 1986. For estimation of buoy speed 1 cm equals 23.1 cm/s.

Figure 4.25 Model ice drift trajectories in cm/s for 27 September 1986. The three vectors toward the bottom center represent speeds of 5, 10 and 20 cm/s, respectively.

Figure 4.26 Model ice drift trajectories in cm/s for 27 October 1986. The three vectors toward the bottom center represent speeds of 5, 10 and 20 cm/s, respectively.
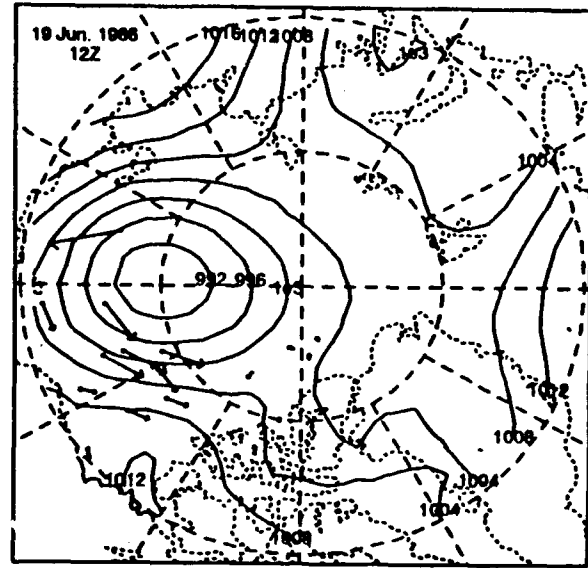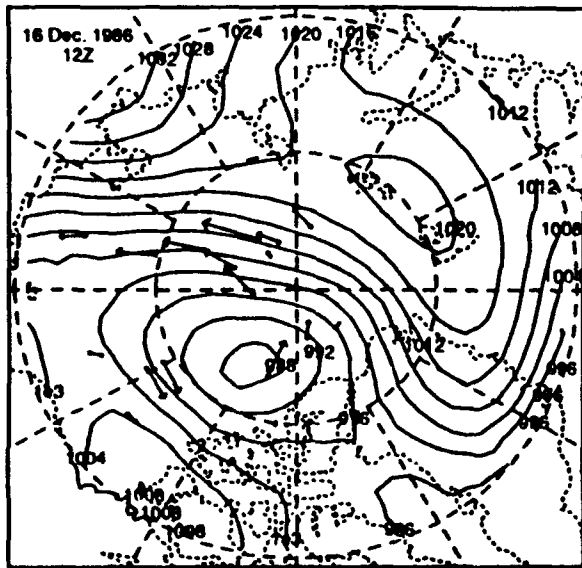
Figure 4.27 Buoy trajectories and buoy derived surface pressure for (a) 16 August, (b) 17 August, (c) 18 August, and (d) 19 August 1986. For estimation of buoy speed 1 cm equals 23.1 cm/s.

Figure 4.28 Model ice drift trajectories in cm/s for 16 August 1986. The three vectors toward the bottom center represent speeds of 5, 10 and 20 cm/s, respectively.

Figure 4.29 Model ice drift trajectories in cm/s for 19 August 1986. The three vectors toward the bottom center represent speeds of 5, 10 and 20 cm/s, respectively.

Figure 4.30 Buoy trajectories and buoy derived surface pressure for (a) 16 December, and (b) 19 June 1986. For estimation of buoy speed 1 cm equals 23.1 cm/s.
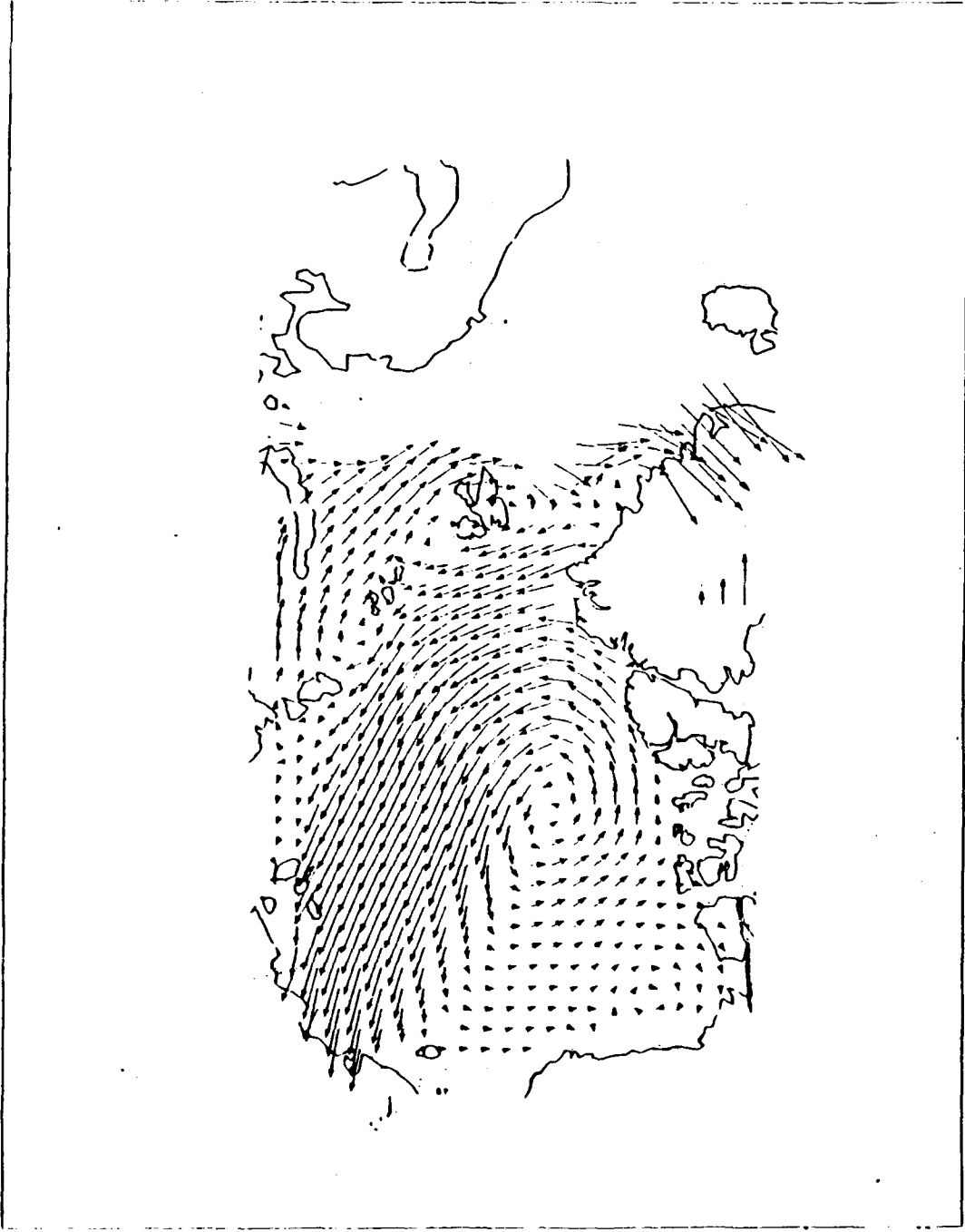
Figure 4.31 Model ice drift trajectories in cm/s for 16 December 1986. The three vectors toward the bottom center represent speeds of 5, 10 and 20 cm/s, respectively.
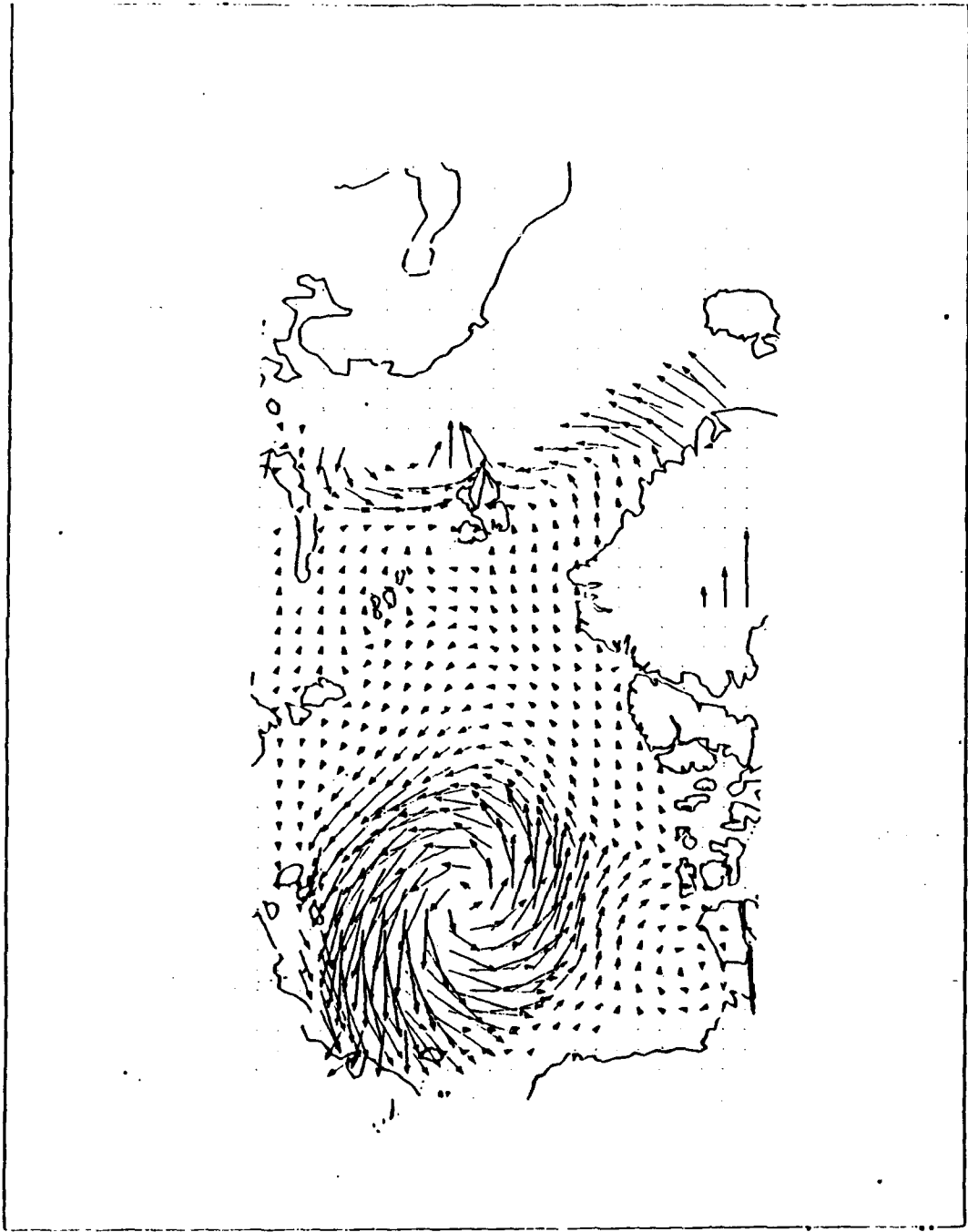
Figure 4.32 Model ice drift trajectories in cm/s for 19 June 1986. The three vectors toward the bottom center represent speeds of 5. 10 and 20 cm/s, respectively.
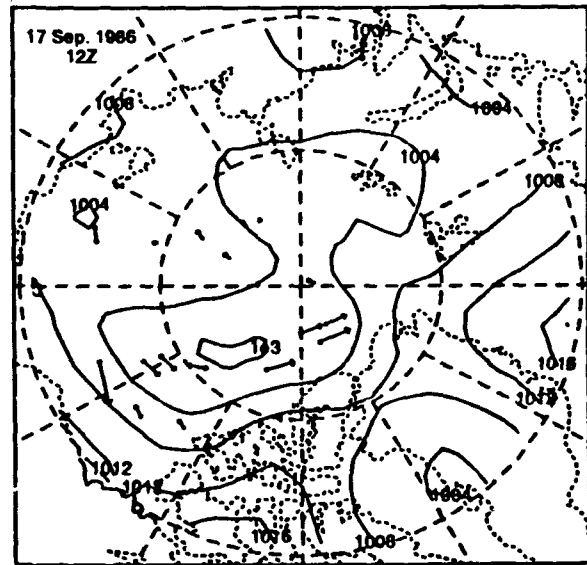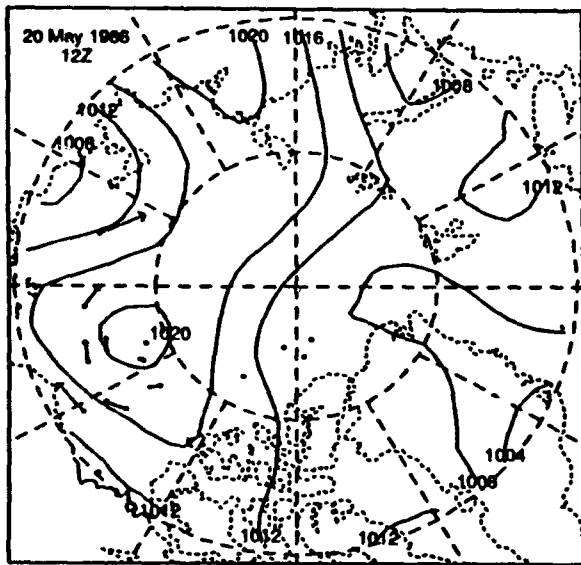
Figure 4.33 Buoy trajectories and buoy derived surface pressure for (a) 20 May, and (b) 17
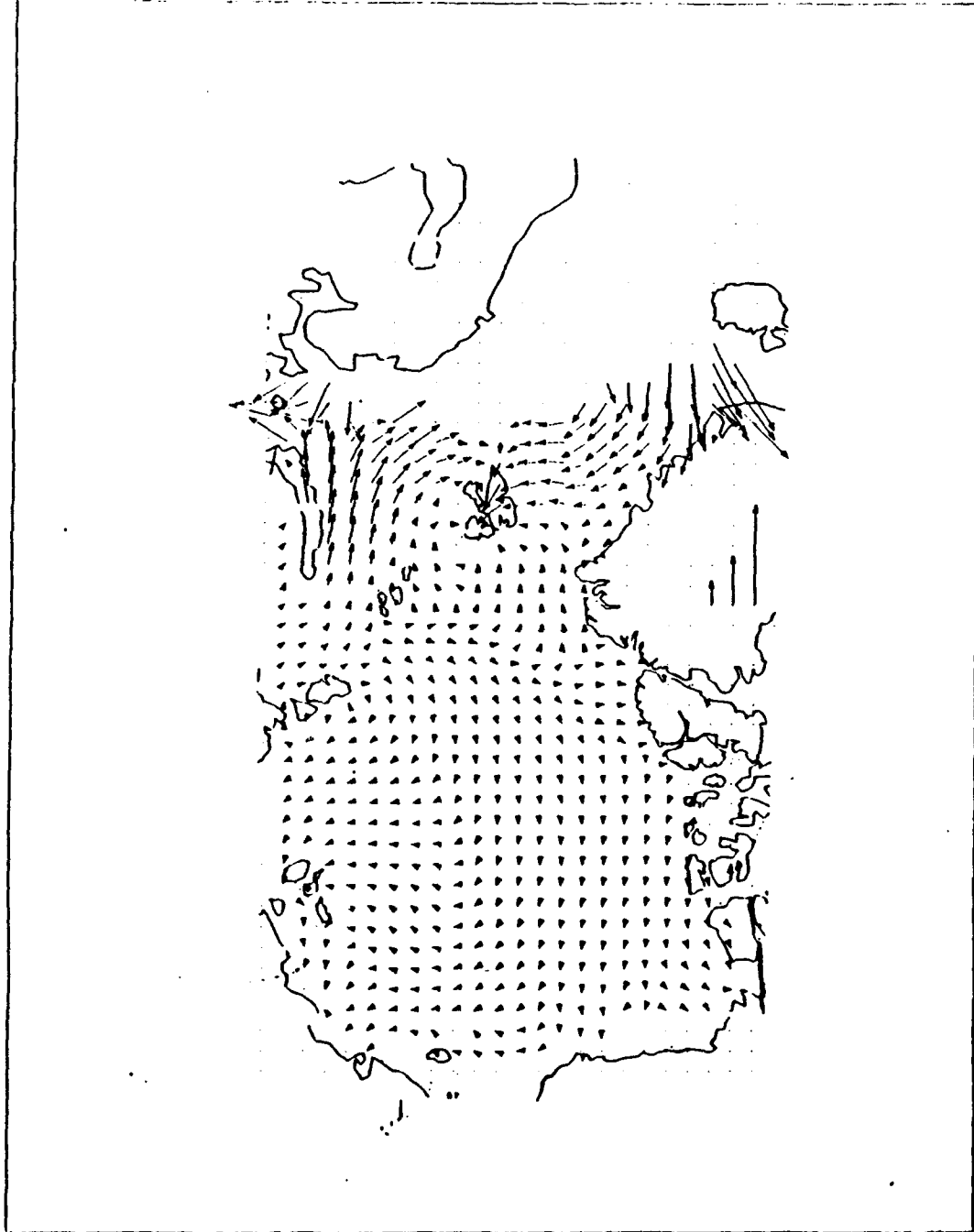September 1986. For estimation of buoy speed 1 cm equals 23.1 cm/s.

Figure 4.34 Model ice drift trajectories in cm/s for 20 May 1986. The three vectors toward the bottom center represent speeds of 5, 10 and 20 cm/s, respectively.
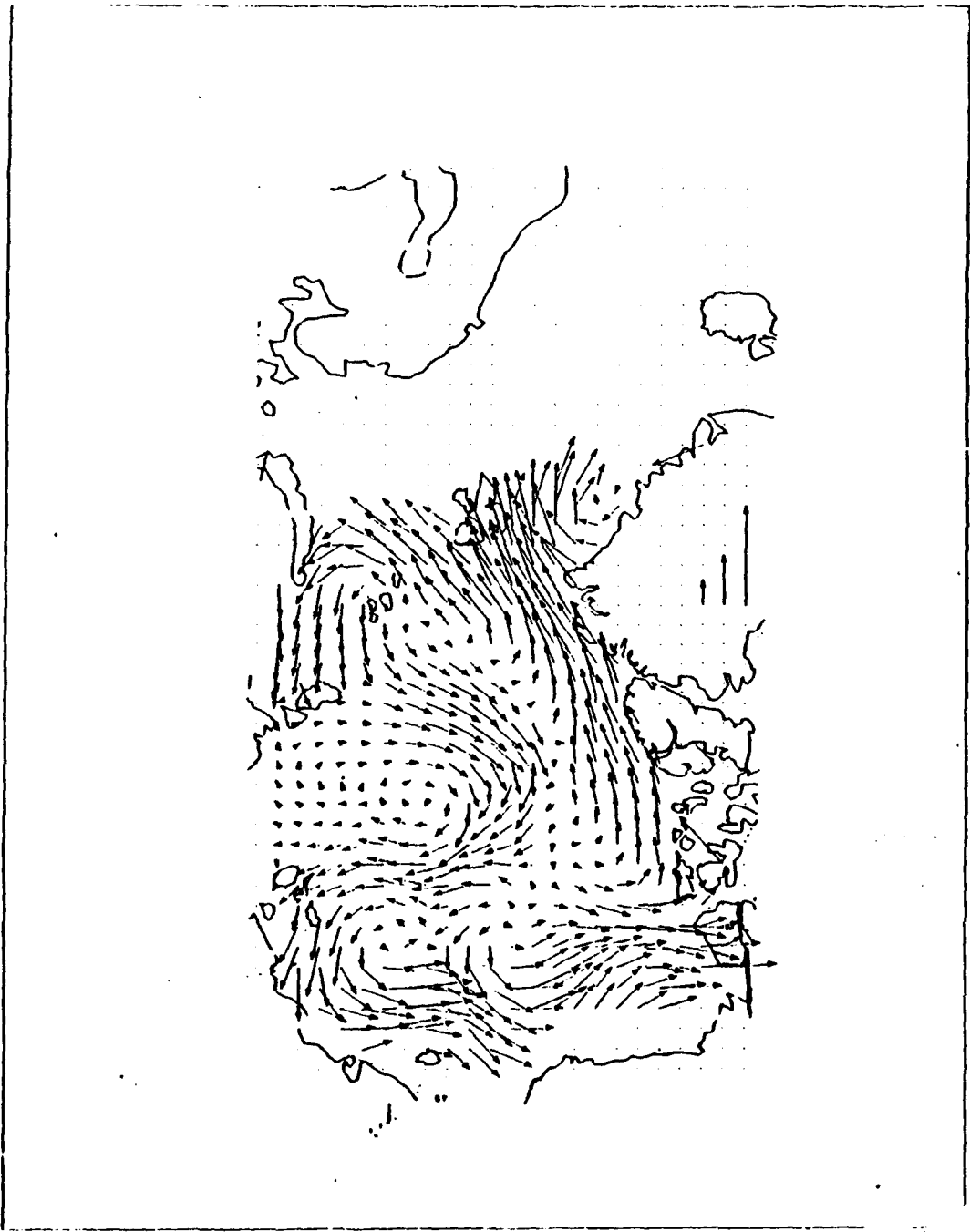
Figure 4.35 Model ice drift trajectories in cm/s for 17 September 1986. The three vectors toward the bottom center represent speeds of 5, 10 and 20 cm/s, respectively.
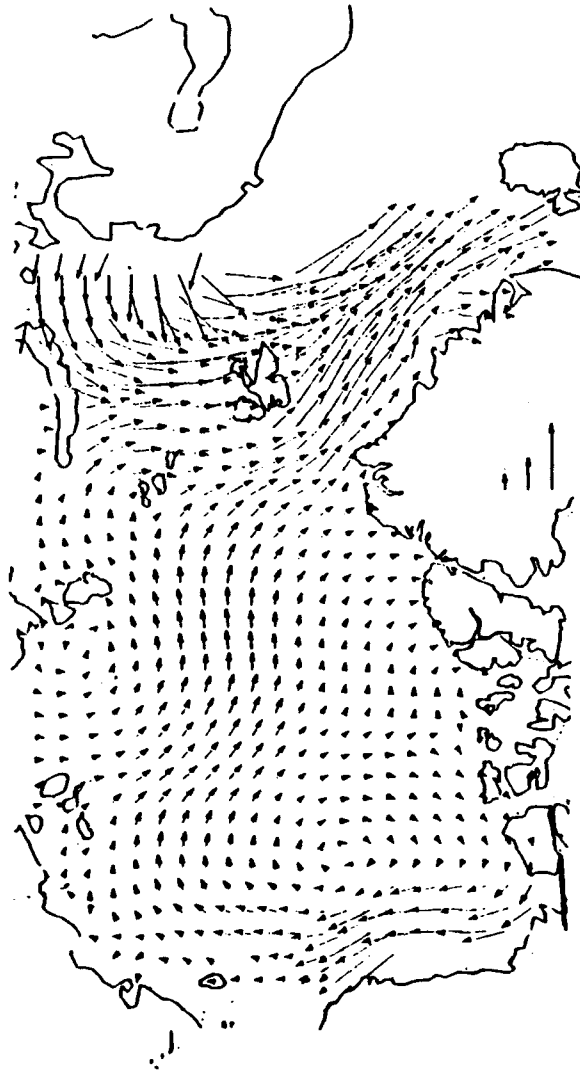
Figure 4.36 Model ice drift trajectories in cm/s for 23 January 1986. The three vectors toward the bottom center represent speeds of 5, 10 and 20 cm/s, respectively.
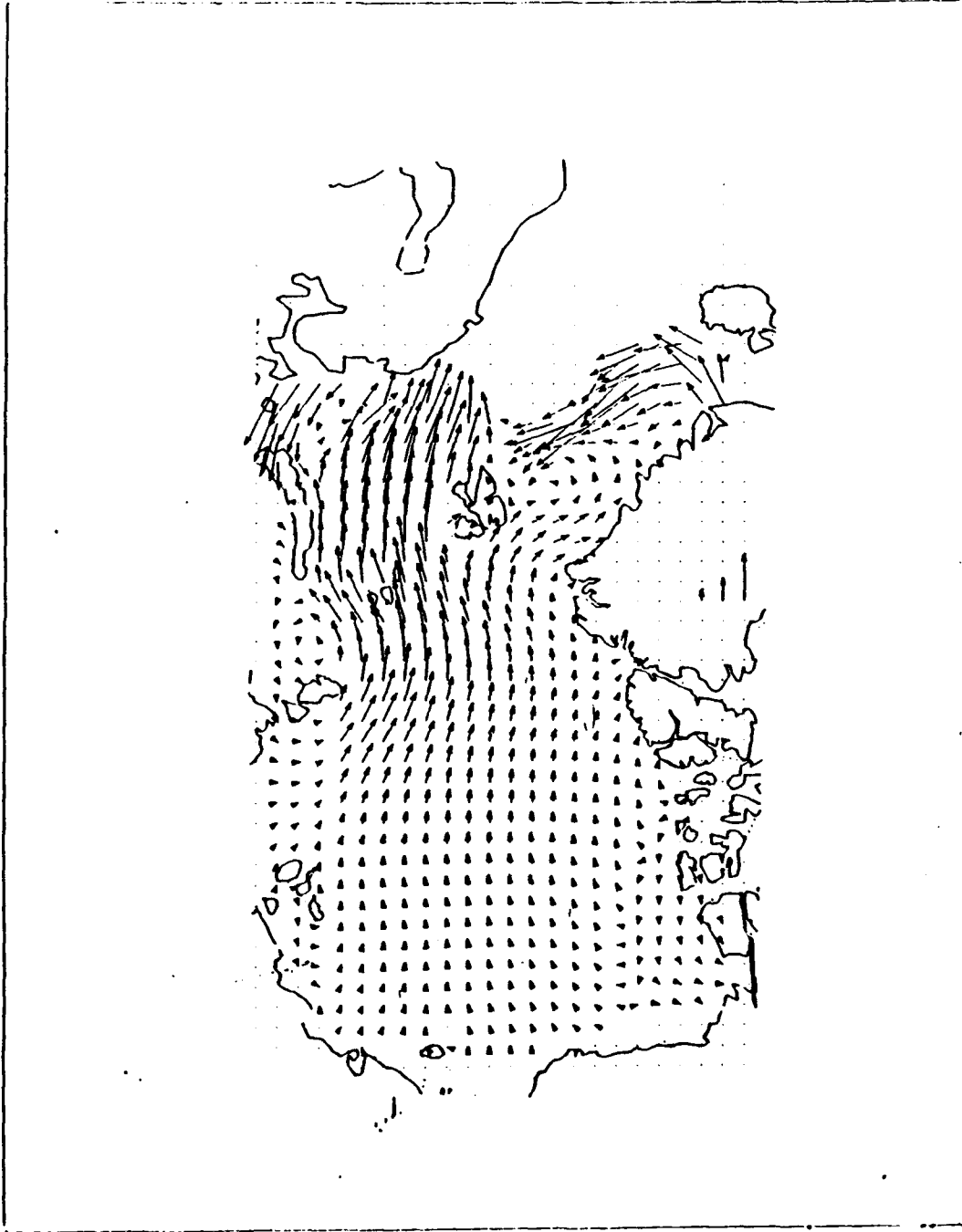
Figure 4.37 Model ice drift trajectories in cm/s for 1 March 1986. The three vectors toward the bottom center represent speeds of 5, 10 and 20 cm/s, respectively.

Figure 4.38 The NPOC eastern Arctic ice edge for 11 March 1986.

Figure 4.39 Model ice edge and concentration (from .1 to .9 in increments of .1) for 11 March 1986.

94

Figure 4.40 The NPOC eastern Arctic ice edge for 20 May 1986.

Figure 4.41 Model ice edge and concentration (from .1 to .9 in increments of .1) for 20 May 1986.

Figure 4.42 The NPOC eastern Arctic ice edge for 8 July 1986.

Figure 4.43 Model ice edge and concentration (from .1 to .9 in increments of .1) for 8 July 1986.

Figure 4.44 The NPOC eastern Arctic ice edge for 17 September 1986.

Figure 4.45 Model ice edge and concentration (from .1 to .9 in increments of .1) for 17 September 1986.
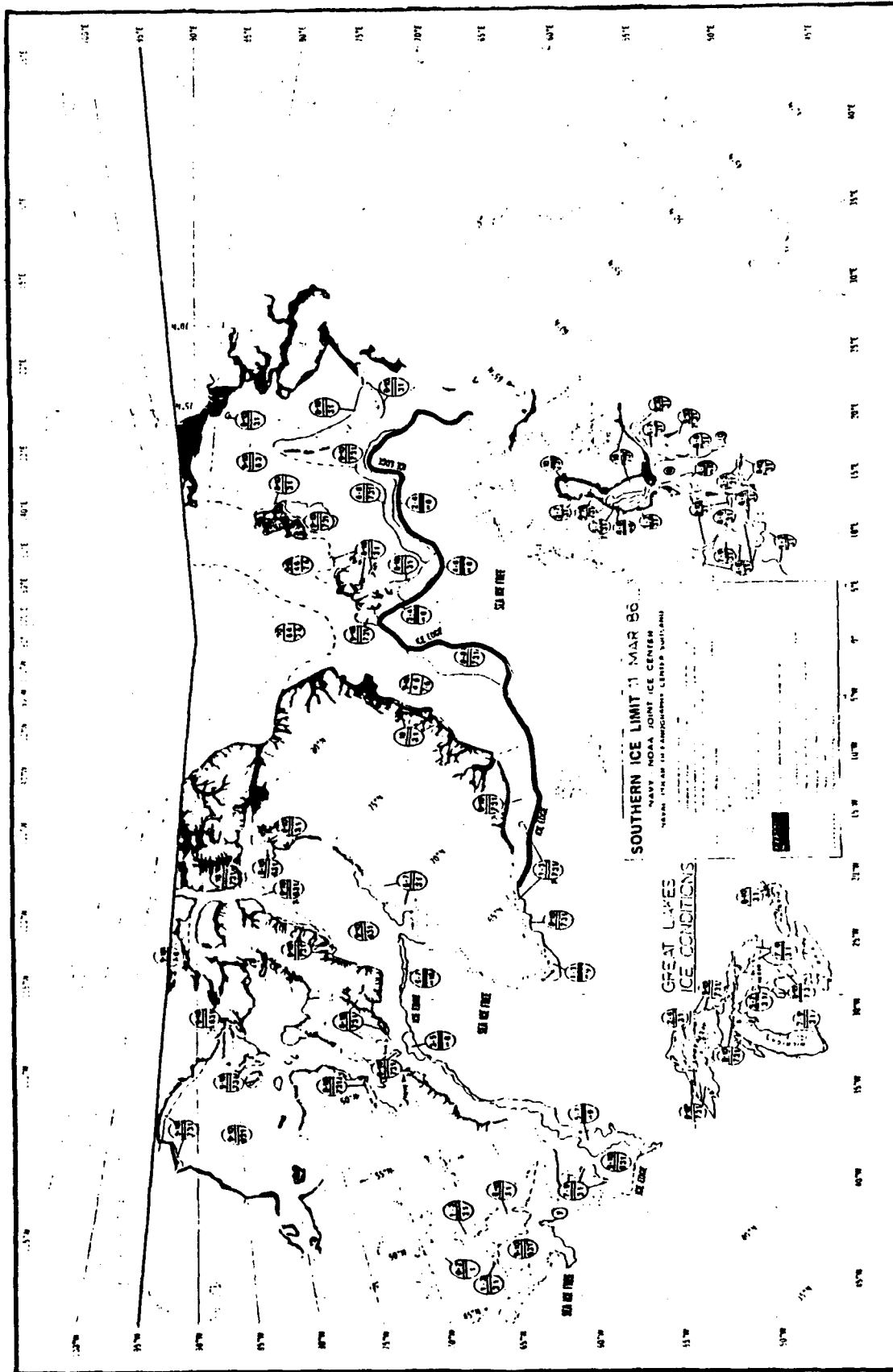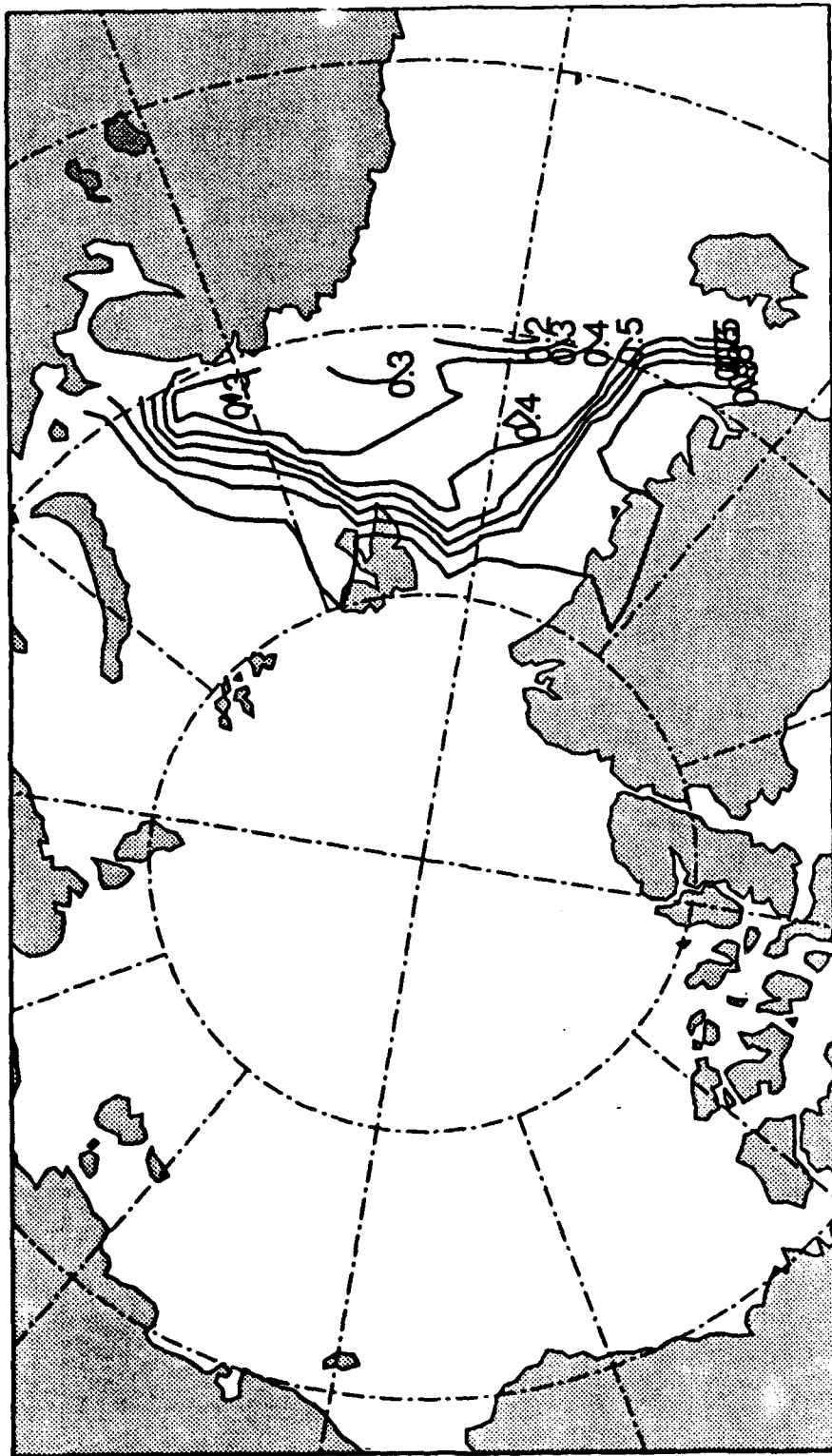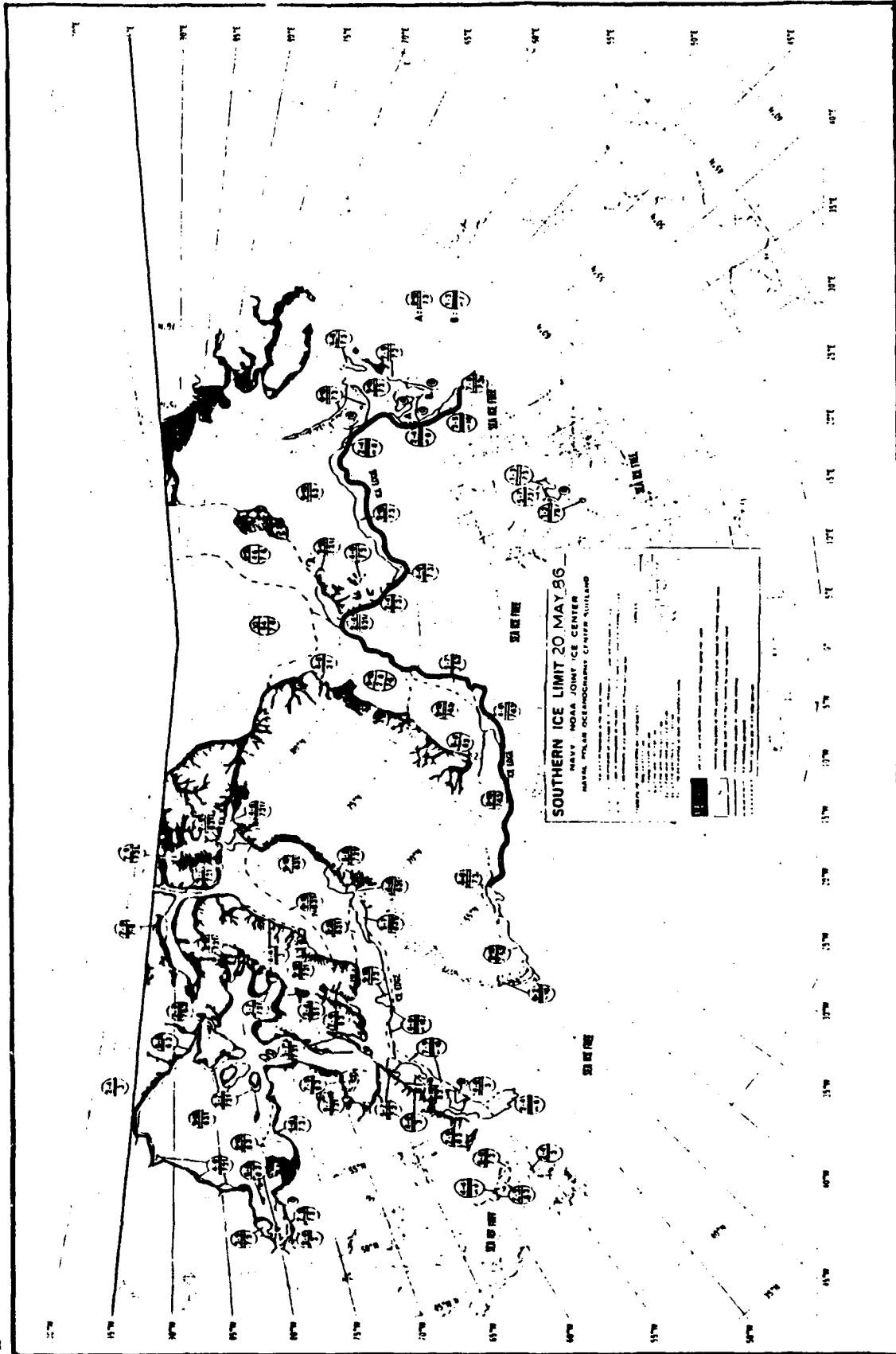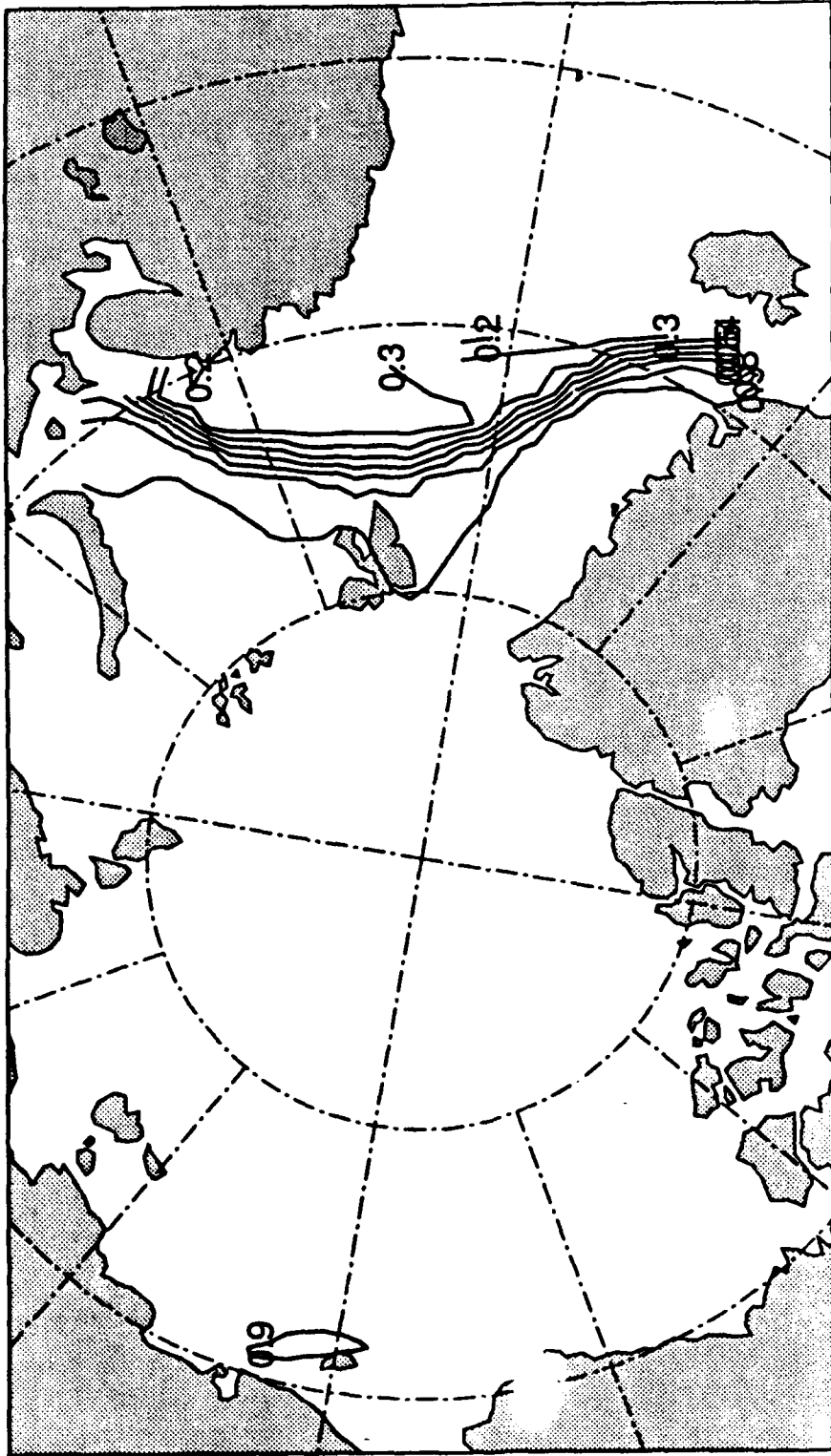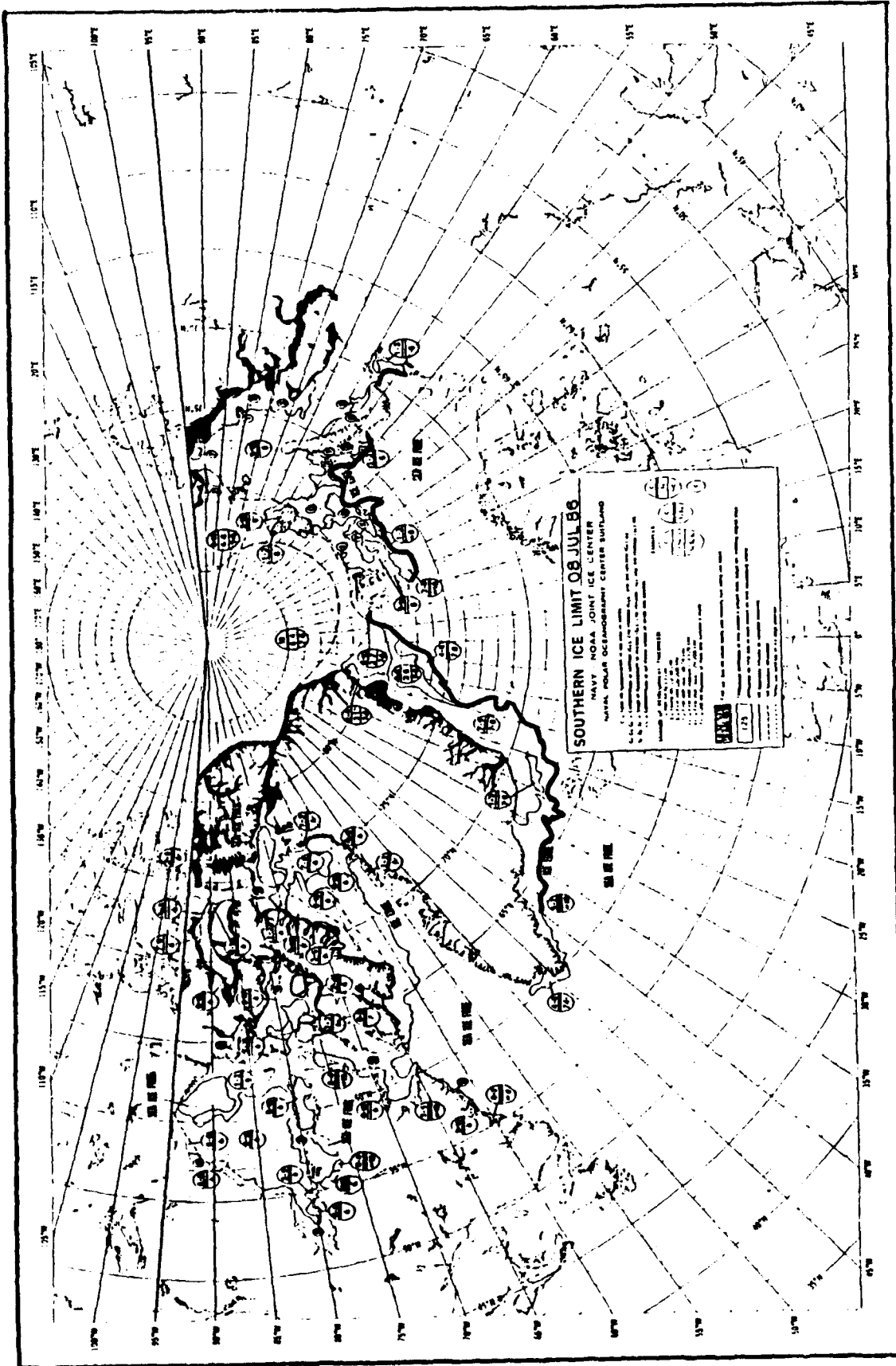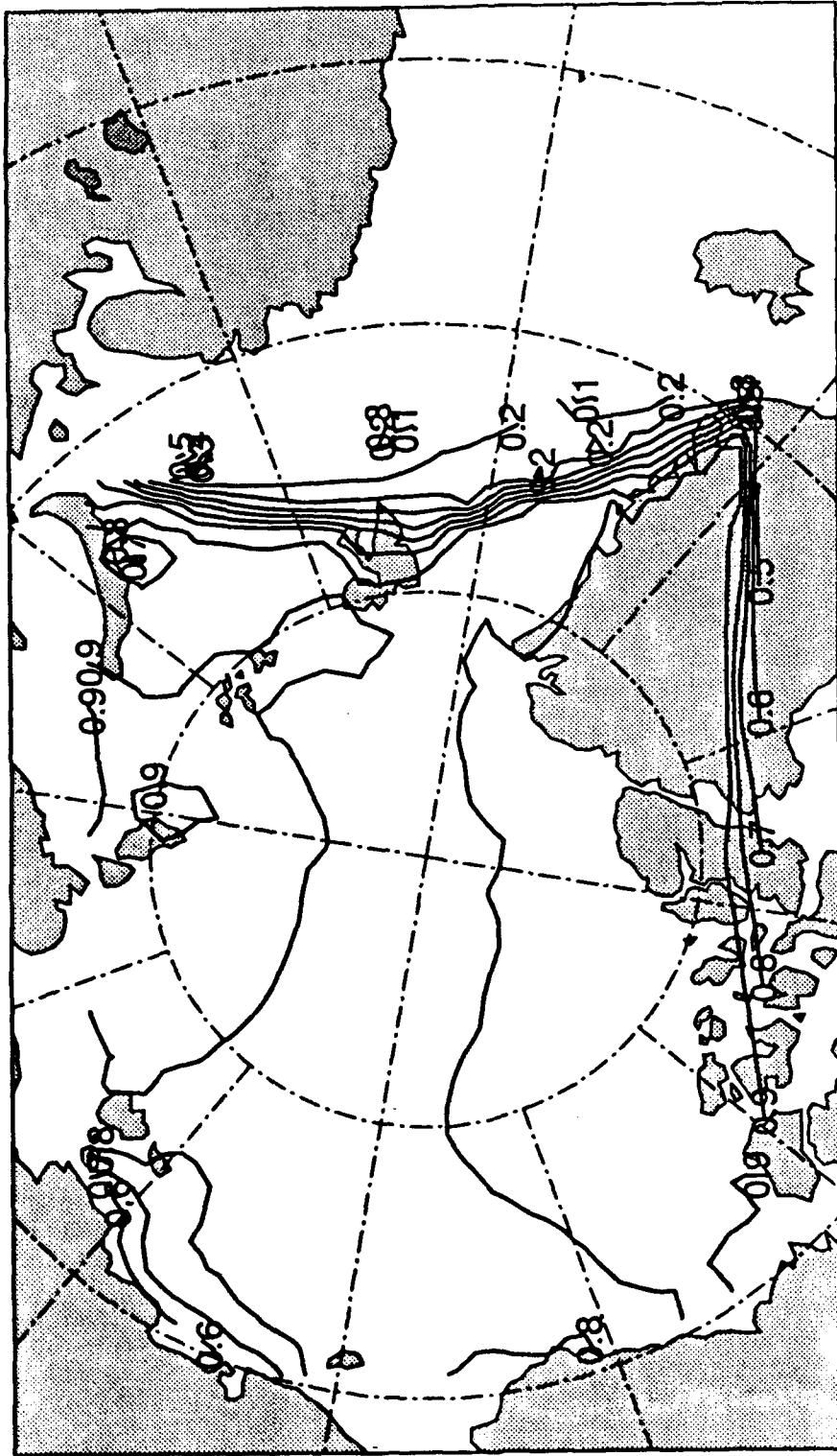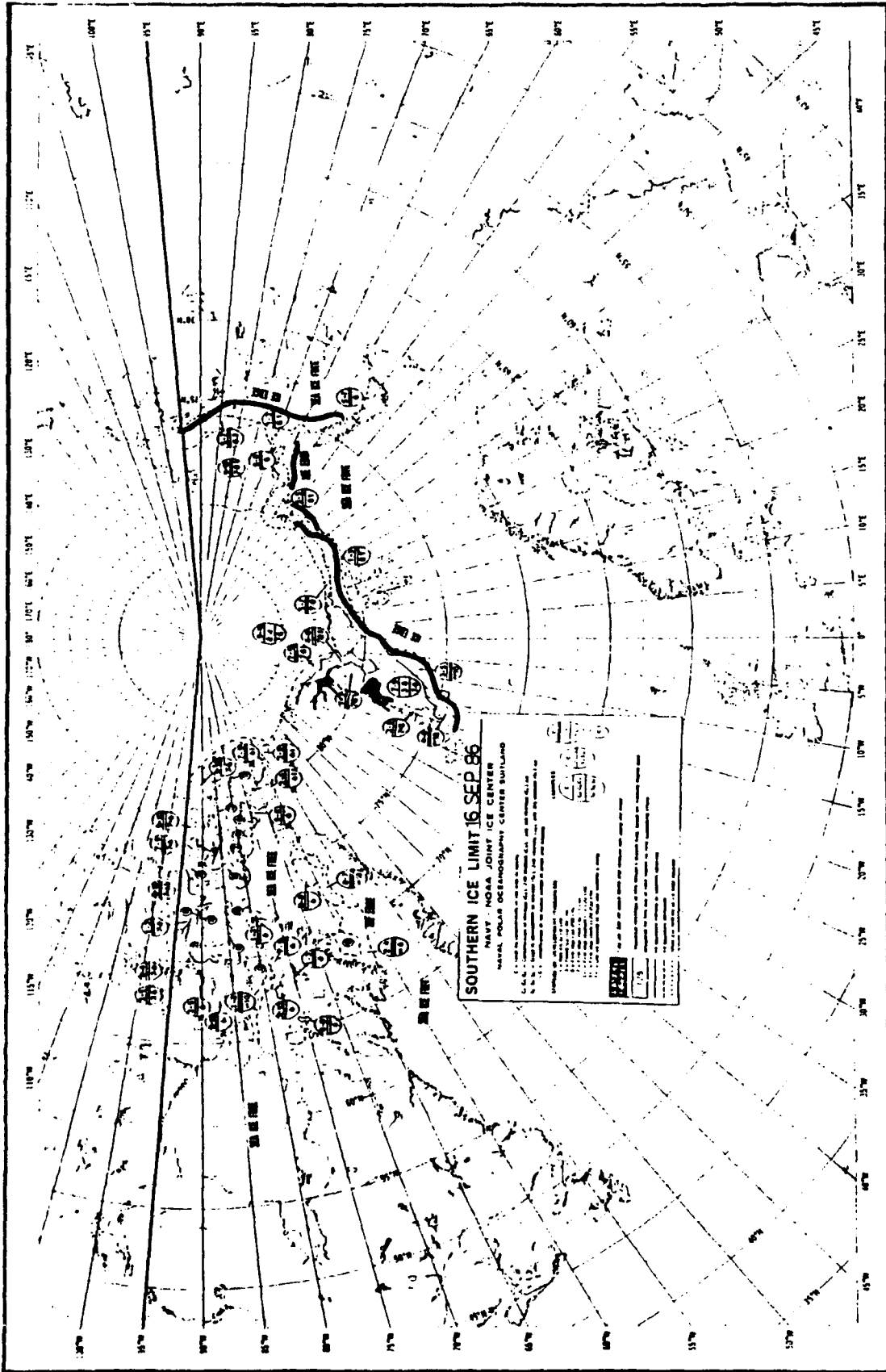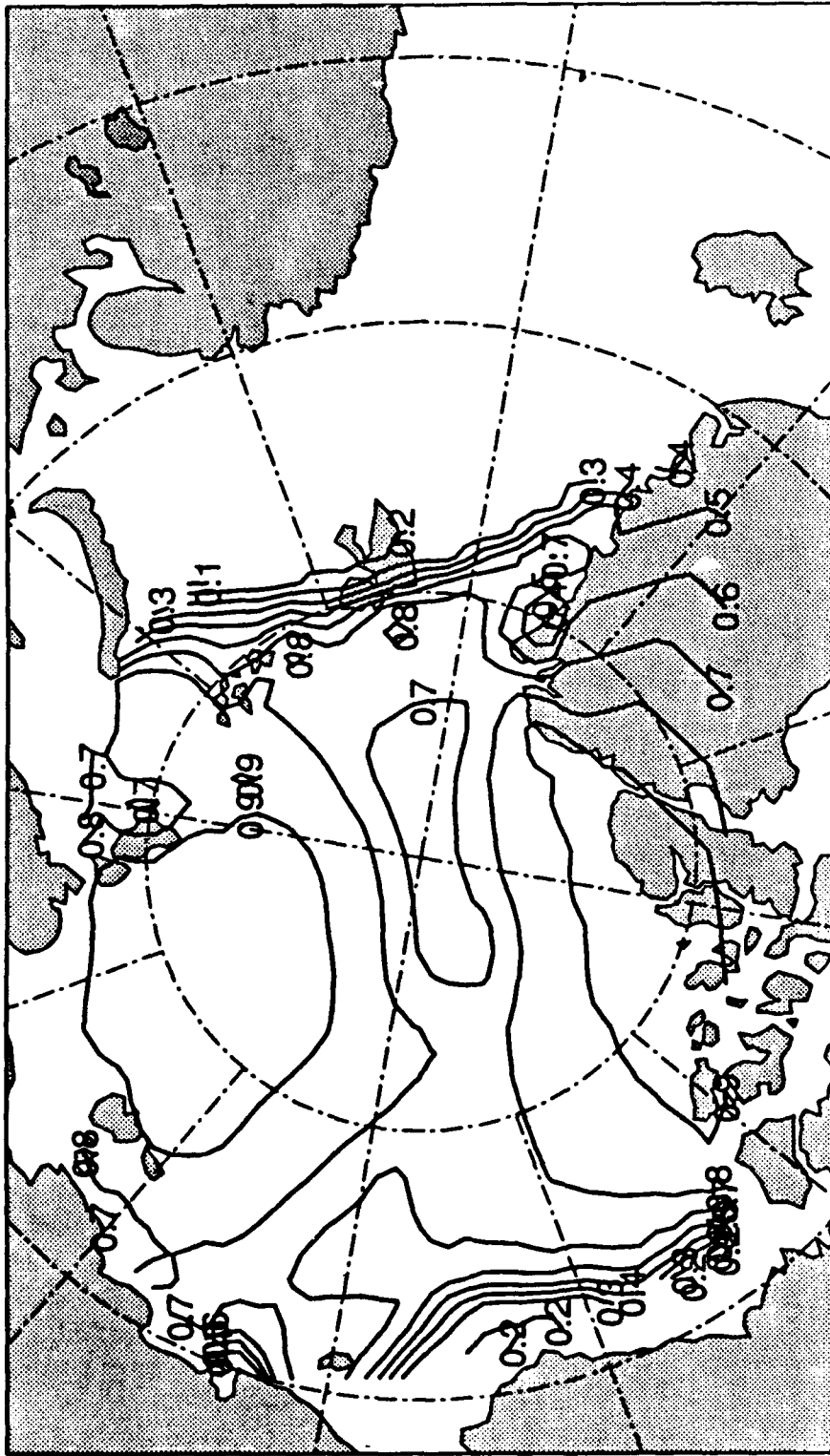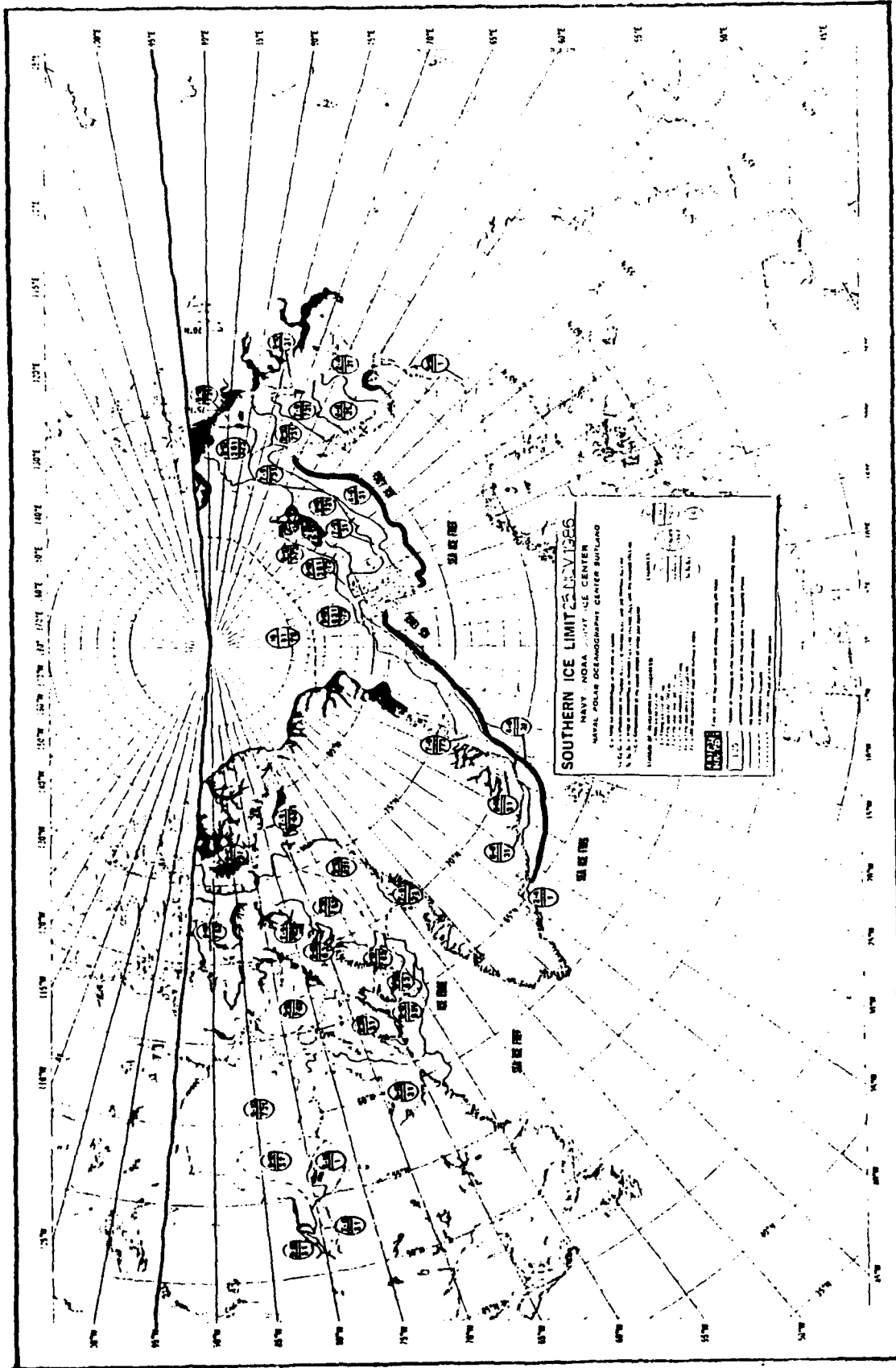
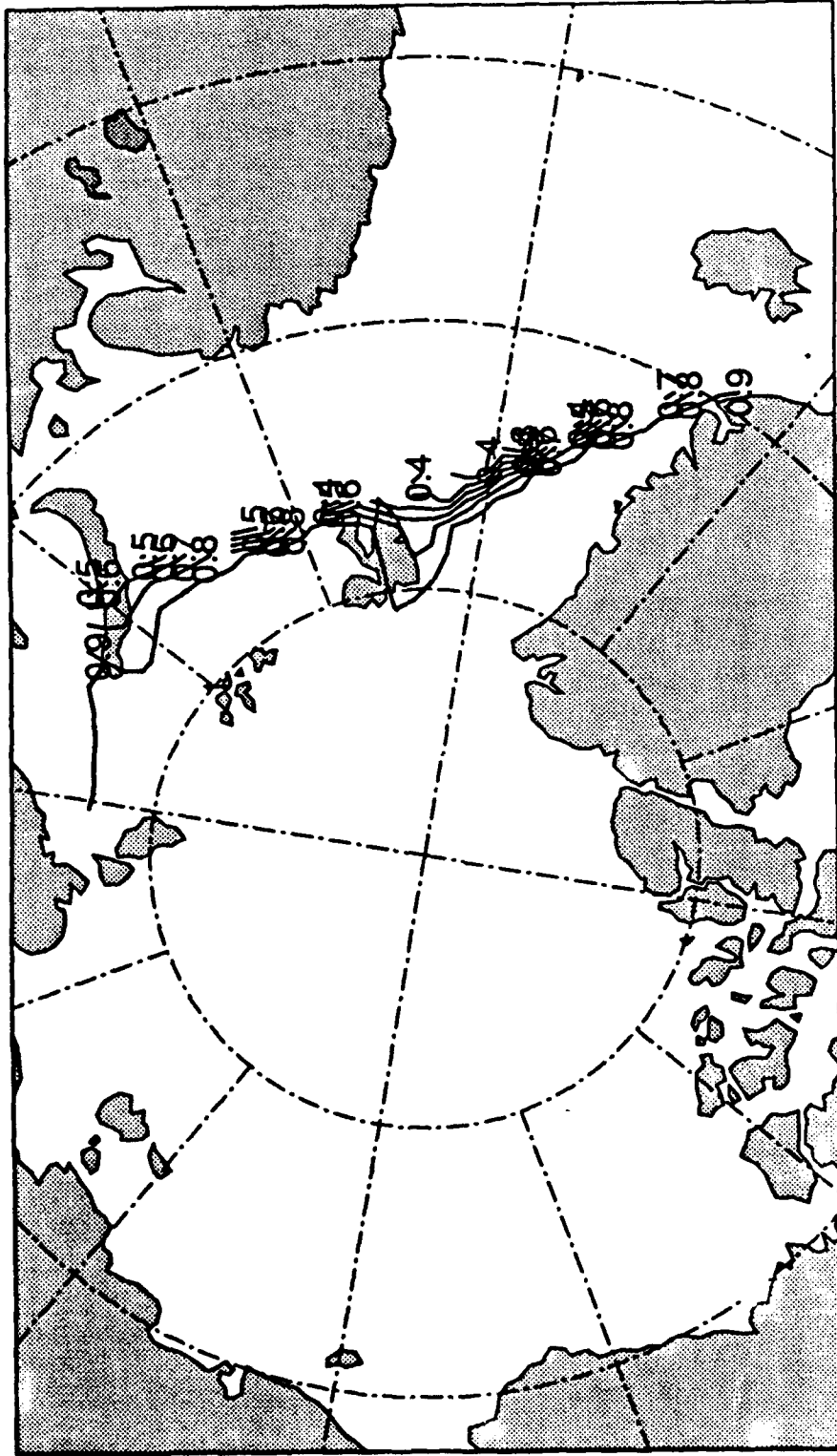Figure 4.46 The NPOC eastern Arctic ice edge for 25 November 1986.

Figure 4.47 Model ice edge and concentration (from .1 to .9 in increments of .1) for 25 November 1986.

V. SUMMARY AND CONCLUSION

A. SUMMARY

As the U. S. Navy conducts operations in the Arctic, there will always continue to be a need for a way to predict the movement and behavior of the ice pack. Early computer models of ice prediction studied and forecast ice movement in isolation without considering the effects of the ice thickness, strength, and thermodynamic growth. Today the Navy uses the PIPS model, based on Hibler's (1979) dynamic-thermodynamic sea ice model, which combines a thermodynamic heat budget ice model with a dynamic ice model which is sensitive to the effects of ice thickness and ice strength interactions.

The dynamic thermodynamic sea ice model simultaneously solves a system of four principle equations of momentum balance, ice rheology, ice thickness distribution, and ice strength. Momentum balance describes the change in ice movement or ice drift through time as the result of a summing of forces of wind and ocean stress, Coriolis force, a sea surface tilting term, and internal ice stress. Of these forces the wind stress term normally has the largest effect on the momentum balance. Ice rheology descibes the internal ice stress interaction through a viscous-plastic law that states that under light strain ice behaves like a highly viscous fluid, and under heavy strain it behaves like a plastic. The ice thickness distribution describes ice thickness and concentration through a seven layered scheme that parameterizes the effects of advection, divergence, growth and decay and includes a heat budget for the ice-ocean-atmosphere system. Finally, ice strength, which is used in the ice rheology, is described as a function of ice thickness and concentration.

The ice model used in this study was adapted from one used by Owens and Lemke (1990) to model the ice cover of the Antarctic and Weddell Sea. For this study the ice

model was fitted with the PIPS Arctic grid (127 km resolution) for its domain and was driven by 1986 NOGAPS forcing data at 12 hour increments over one annual cycle. The forcing data included pressure fields for deriving geostrophic winds and atmospheric thermodynamic data to drive the heat budget. The monthly ocean currents and oceanic heat fluxes used by the ice model originated from the Hibler-Bryan coupled ice-ocean model. The ice model had an option for using a vertically varying prognostic oceanic mixed layer but for this study the mixed layer was held to a constant depth of 30 m.

To initialize the model it was started with an ice field of uniform thickness, concentration, and velocity and was driven by the 1986 forcing input data for three years to permit the ice field to stabilize. The third year results were examined and compared to buoy drift data to evaluate model performance under differing environmental conditions

B. CONCLUSIONS AND RECOMMENDATIONS

The main purpose of this thesis was to study and evaluate the performance of the NPS version of the PIPS Arctic sea ice model. The focus of the study was to evaluate the ice model's ability to depict the movement of ice in both speed and direction. Ice model results from 1986 were qualatatively analyzed and compared to Arctic buoy drift data under differing environmental conditions of decreasing wind speed, increasing wind speed, steady state light or calm winds, steady high winds resulting from strong pressure gradients, and gyre reversals. The case of the ice drift in the Greenland Sea was also examined.

It was found that the ice model generally performed well in depicting ice movement. Model performance was better at higher wind speed but performance at lower wind speed was reasonable. Model reaction to changing weather and wind conditions was almost immediate. However, a 12 hour time lag was noted for decreasing ice drift speeds. There was less variability in ice drift direction with sustained winds above 10 m/s Thinner and less concentrated ice tended to move at a greater rate than thicker and

more compact ice. Some discrepancies between model and buoy data could be traced to inaccuracies in the NOGAPS data used to drive the model. Model comparison with NPOC ice edge reports placed the modeled ice edge generally more than 100 km south of the actual ice edge, most likely resulting from the poor representation of ocean heat fluxes at the ice edge by the monthly oceanic heat fluxes. Weekly updates of the ice edge in PIPS as run at FNOC prevents this from being a problem.

The sea ice model's reasonable depiction of ice motion warrants its continued use by the Navy as an operational model. Its chief limitation, correctly modeling the input data, will improve in time as more powerful computers come on line which will permit finer spatial resolution. The data sparse Arctic will always present a challenge with regards to small scale features contained within it. Regional models now under development will improve this aspect especially along the ice edge.

Further areas of study would be to take the model output data and the buoy data and conduct a statistical analysis for a quantitative study. Additional studies could include running the ice model with different forcing and parameters to see if there is an improvement in ice edge location and ice thickness accuracy, and running the model with different relaxation schemes to improve computational efficiency.

REFERENCES

Bryan, K., A numerical method for study of the circulation of the world oceans, *J. Comput. Phys.*, 4, 347-376, 1969.

Colony, R., and I. Rigor, Arctic Ocean buoy program data report for 1 January 1986 - 31 December 1986, Applied Physics Laboratory, University of Washington, Technical Memorandum APL-UW TM6-89, 139 pp., 1989.

Comiso, J. C., Arctic multiyear ice classification and summer ice cover using passive microwave satellite data, *J. Geophys. Res.*, 95 (C8), 13,411-13,422, 1990.

Coon, M. D., S. Maykut, R. Pritchard, D. Rothrock, and A. Thorndike, Modelling the pack ice as an elastic-plastic material, *AIDJEX Bulletin*, 24, 105 pp., 1974.

Naval Polar Oceanography Center, Eastern - Western Arctic Sea Ice Analysis bi-monthly series, Suitland, Md., 1986.

Gloersen, P., and W. J. Campbell, Variations on the Arctic, Antarctic, and global sea ice covers during 1978-1987 as observed with the Nimbus 7 scanning multichannel micro-wave radiometer, *J. Geophys. Res.*, 93(C9), 10,666-10,674, 1988.

Hibler, W. D., III, A dynamic thermodynamic sea ice model, *J. Phys Oceanogr.*, 9, 815-846, 1979.

Hibler, W. D., III, Ice dynamics, U. S. Army Cold Regions Research and Engineering Laboratory, Hanover, NH, CRREL Report 84-3, 52pp., 1984.

Hibler, W. D., III, Numerical modelling of sea ice dynamics and ice thickness characteristics, a final report, U. S. Army Cold Regions Research and Engineering Laboratory, Hanover, NH, CRREL Report 85-5, 50 pp., 1985.

Hibler, W. D., III, Ice dynamics, *in: The Geophysics of Sea Ice*, N. Untersteiner, ed., Plenum Press, New York, NY, 577-640, 1986.

Hibler, W. D., III, and K. Bryan, Ocean circulation: its effects on seasonal sea-ice simulations, *Science*, 224, 489-491, 1984.

Hibler W. D., III, and K. Bryan, A diagnostic ice-ocean model, *J. Phys. Oceanogr.*, 17, 987-1017, 1987.

Hibler, W. D., III, and J. E. Walsh, On modelling seasonal and interannual fluctuations of Arctic sea ice, *J. Phys Oceanogr.*, 12, 1514-1523, 1982.

Lemke, P., A coupled one-dimensional sea ice-ocean model, *J. Geophys. Res.*, 92 (C12), 13,164-13,172 1987.

Lemke, P., W. B. Owens, and W. D. Hibler, III, A coupled sea ice mixed layer pycnocline model for the Weddell Sea, *J. Geophys. Res.*, 95 (C6), 9513-9525, 1990.

McLaren, A. S., M. C. Serreze, and R. G. Barry, Seasonal variations of ice motion in the Canada Basin and their implications, *Geophys. Res. Let.*, 114, 1123-1126, 1987.

Manabe, S., K. Bryan, and M. Spelman, A global ocean-atmosphere climate model with seasonal variation for future studies of climate sensitivity, *Dynamics of Atmosphere and Ocean*, 3, 393-426, 1979.

Maykut, G. K., and N. Untersteiner, Some results from a time-dependent thermodynamic model of sea ice, *J. Geophys. Res.*, 76, 1550-1575, 1971.

Mesinger, F., and A. Arakawa, Numerical methods used in atmospheric models, Global Atmospheric Research Programme (GARP), WMO-ICSU Joint Organizing Committee Global Atmospheric Research Publication Series, 17, 1976.

McPhee, M. G., The effect of the oceanic boundary layer on the mean drift of pack ice: application of a simple model, *J. Phys. Oceanogr.*, 9, 388-400, 1979.

Owens, W. B., and P. Lemke, Sensitivity studies with a sea ice-mixed layer-pycnocline model in the Weddell Sea, *J. Geophys. Res.*, 95 (C6), 9527-9538, 1990.

Parkinson, C. L., and W. M. Washington, A large-scale numerical model of sea ice, *J. Geophys. Res.*, 84 (C1), 311-337, 1979.

Parkinson, C. L., J. C. Comiso, H. J. Zwalley, D. J. Cavalieri, P. Gloersen, and W. J. Campbell, Arctic sea ice, 1973-1974, satellite passive microwave observations, *NASA Spec. Publ.*, Sp-489, 296 pp., 1987.

Parkinson, C. L., and D. J. Cavalieri, Arctic sea ice 1973-1987: seasonal, regional, and inter annual variability, *J. Geophys. Res.*, 94 (C10), 14,499-14,523, 1989.

Posey, P., Personal correspondance, Naval Oceanographic and Atmospheric Research Laboratory, Code 322, Stennis Space Center, MS 39529, 1990.

Preller, R., and P. Posey, The Polar Ice Prediction System, a sea ice forecasting system, NORDA Technical Report 212, 42 pp., 1989.

Preller, R. H., The NORDA/FNOC Polar Ice Prediction System (PIPS) Arctic. A technical description, NORDA Technical Report 108, 60 pp., 1985.

Pritchard, R. S., A simulation of near shore winter ice dynamics in the Beaufort Sea, *in: Sea Ice Processes and Models*, R. S. Pritchard, ed., University of Washington Press, Seattle, 49-61, 1980.

Rothrock, D. A., The energetics of the plastic deformation of pack ice by ridging, *J. Geophys. Res.*, 80, 4514-4519, 1975.

Semtner, A. J., Jr., A model for the thermodynamic growth of sea ice in numerical investigation of climate, *J. Phys. Oceanogr.*, 6, 379-389, 1976.

Serreze, M. C., R. G. Barry, and A. S. McLaren, Seasonal variations in sea ice motion and effects on sea ice concentration in the Canada Basin, *J. Geophys. Res.*, 94 (C8), 10,955-10,970, 1989.

Skiles, F. L., Empirical wind drift of sea ice, *in: Arctic Drifting Stations*, J. E. Sater, ed., The Arctic Institute of North America, Washington, D. C., 239-254, 1968.

Stossel, A., P. Lemke, and W. B. Owens, Coupled sea ice- mixed layer simulations for the southern ocean, *J. Geophys. Res.*, 95 (C6), 9539-9555, 1990.

Thorndike, A. S., D. Rothrock, G. Maykut, and R. Colony, The thickness distribution of sea ice, *J. Geophys. Res.*, 80 (no. 33), 4501-4513, 1975.

Thorndike, A. S., and R. Colony, Arctic Ocean buoy program data report: 19 January 1979-31 December 1979, Polar Science Center, University of Washington, Seattle, 131 pp., 1980.

Thorndike, A. S., and R. Colony, Sea ice motion in response to geostrophic winds, *J. Geophys. Res.*, 87 (C7), 5845-5892, 1982.

Tucker, W. B., III, A comparison of sea ice model results using three different wind forcing fields, U. S. Army Cold Regions Research and Engineering Laboratory, CRREL Report 83-17, 11 pp., 1983.

Tucker, W. B., III, and W. D. Hibler, III, An evaluation of the Polar Ice Prediction System, U. S. Army Cold Regions Research and Engineering Laboratory, Hanover, NH, 34 pp., 1986.

Zwalley, H. J., J. C. Comiso, C. L. Parkinson, W. J. Campbell, F. D. Carrey, and P. Gloersen, Antarctic sea ice, 1973-1976: satellite passive microwave observations, *NASA Spec. Publ.*, Sp-459, 1983.

INITIAL DISTRIBUTION LIST

No. Copies

1. Defense Technical Information Center   2
    Cameron Station
    Alexandria, VA 22304-6145

2. Library, Code 52   2
    Naval Postgraduate School
    Monterey, CA 93943-5002

3. Chairman (Code OC/Co)   1
    Department of Oceanography
    Naval Postgraduate School
    Monterey, CA 93943-5000

4. Dr. R. H. Bourke (Code OC/Bf)   3
    Naval Postgraduate School
    Monterey, CA 93943-5000

5. Dr. James Morison   1
    Applied Physics Labratory
    University of Washington
    1019 NE 40th ST
    Seattle, WA 98105-6698

6. Ruth Preller, Code 322   1
    Naval Oceanographic and Atmospheric
    Research Laboratory
    Stennis Space Center, MS 39529-5004

7. Dr W. B. Owens   1
    Woods Hole Oceanographic Institution
    Woods Hole, MA 02543

8. LT. G. N. Lundeen   1
    Naval Oceanographic and Atmospheric
    Research Laboratory
    Stennis Space Center, MS 39529-5004

9. Dr. W. D. Hibler, III   1
    Dartmouth College
    Hanover, NH 03755

10. Dr. W. B. Tucker, III   1
    U. S. Army Cold Regions Research
    and Engineering Laboratory
    Hanover, NH 03755-1290

11. Comanding Officer   1
    Naval Polar Oceanography Center
    Suitland Road
    Washington, DC 20390-5180